Plasmonic manipulation of thermoresponsive and thermosetting polymers

Michael Fedoruk

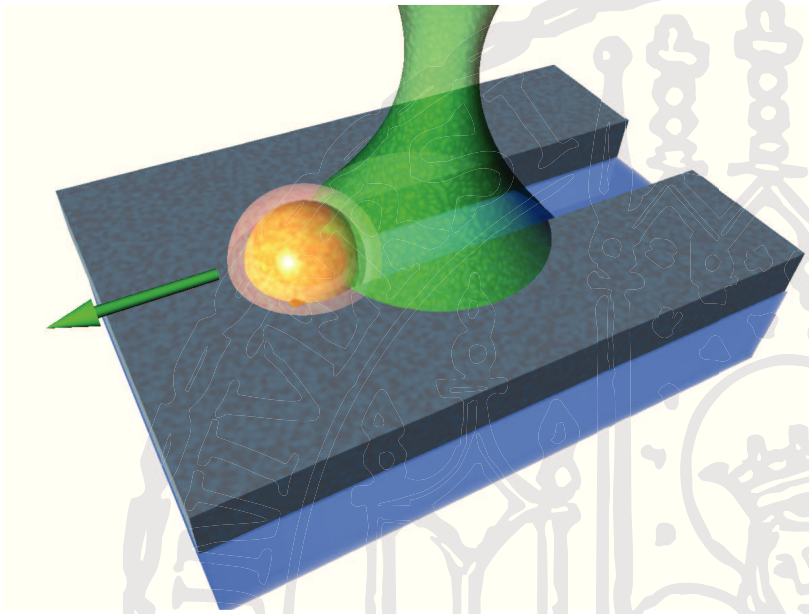

München 2013

Plasmonic manipulation of thermoresponsive and thermosetting polymers

Michael Fedoruk

München 2013

Plasmonic manipulation of thermoresponsive and thermosetting polymers

Michael Fedoruk

Dissertation
an der Fakultät für Physik
der Ludwig-Maximilians-Universität
München

vorgelegt von
Michael Fedoruk
aus Mariupol (Ukraine)

München
April 2013

Erstgutachter:	Prof. Dr. Jochen Feldmann
Zweitgutachter:	Prof. Dr. Joachim Rädler
Tag der Verteidigung:	23.07.2013

Cover: Nanoscopic milling with a gold nanoparticle

Publications

Publications based on the result of this thesis:

- *Triggering the volume phase transition of core–shell Au nanorod–microgel nanocomposites with light*
  J. Rodríguez-Fernández, M. Fedoruk, C. Hrelescu, A.A. Lutich, J. Feldmann
  Nanotechnology 22, 245708 (2011)

- *Subdiffraction-Limited Milling by an Optically Driven Single Gold Nanoparticle*
  M. Fedoruk, A.A. Lutich and J. Feldmann
  ACS Nano 5, 9, 7377-–7382 (2011)

- *Shrink-to-fit Plasmonic Nanostructures*
  A.S. Urban, M. Fedoruk, S. Nedev, A.A. Lutich, T. Lohmueller, J. Feldmann
  Advanced Optical Materials 1, 2, 123-127 (2013)

- *Nanolithography by Plasmonic Heating and Optical Manipulation of Gold Nanoparticles*
  M. Fedoruk, M. Meixner, S. Carretero-Palacios, T. Lohmueller, J. Feldmann
  Manuscript submitted

Further publications:

- *Controlling Loading and Optical Properties of Gold Nanoparticles on Liposome Membranes*
  T.K. Sau, A.S. Urban, S.K. Dondapati, M. Fedoruk, M.R. Horton, A.L. Rogach, F.D. Stefani, J.O. Rädler, J. Feldmann
  Colloids and Surfaces A 342 (1-3), 92-96 (2009)

- *Controlled Nanometric Phase Transitions of Phospholipid Membranes by Plasmonic Heating of Single Gold Nanoparticles*
  A.S. Urban, M. Fedoruk, M.R. Horton, J.O. Raedler, F.D. Stefani, J.Feldmann
  Nano Letters 9 (8), 2903 (2009)

- *Single Step Injection of Gold Nanoparticles through Phospholipid Membranes*
  A.S. Urban, T. Pfeiffer, M. Fedoruk, A.A. Lutich, J. Feldmann
  ACS Nano 5, 3585 (2011)

Contributions to conferences and workshops

- *Controlled Heating And Material Transport Through Phospholipid Bilayers By Plasmonic Heating Of Gold Nanoparticles*
  A. S. Urban, M. Fedoruk, F. D. Stefani, M. R. Horton, J. O. Rädler, J. Feldmann
  Complex Nanosystems: Assembly, Control and Functionality, Venice, Italy, October 2008.

- *Optothermal manipulations of thin films*
  M. Fedoruk
  Workshop From Biophotonics to Optoelectronics, Riezlern, Austria, October 2011.

- *Subdiffraction-Limited Milling by an Optically Driven Single Gold Nanoparticle*
  M. Fedoruk, A. A. Lutich and J. Feldmann
  Seoul Nanohealth 2011 Symposium, Seoul, South Korea, November 2011.

- *Subdiffraction-Limited Milling by an Optically Driven Single Gold Nanoparticle*
  M. Fedoruk, A. A. Lutich and J. Feldmann
  Material Research Society (MRS) Fall Meeting, Boston, USA, December 2011.

Kurzfassung

In dieser Arbeit werden neuartige Anwendungsmöglichkeiten von Goldnanopartikeln als Sensoren und Aktoren für temperaturabhängige Veränderungen von Polymeren auf der Nanometerskala untersucht. Darüber hinaus werden Verfahren entwickelt, um die Eigenschaften von thermoresponsiven und duroplastischen Polymeren durch plasmonisches Heizen von Goldnanopartikeln gezielt und lokal zu verändern.

Die in dieser Arbeit verwendeten Goldnanopartikel besitzen einen Durchmesser von unter 100 nm und zeigen aufgrund ihrer Größe bemerkenswerte optische Eigenschaften. Diese basieren auf sogenannten lokalisierten Oberflächenplasmonen, kollektive Oszillationen der Leitungsbandelektronen, die von einer einfallenden elektromagnetischen Welle angeregt werden. Die wellenlängenabhängige Oberflächenplasmonenresonanz solcher Goldnanopartikel führt in einem bestimmten Bereich des sichtbaren Lichtspektrums zu einer Erhöhung des gestreuten und absorbierten Lichts. Dadurch werden Goldnanopartikel, trotz ihrer kleinen Abmessungen, durch rein optische Methoden, wie die Dunkelfeldmikrokopie, sichtbar und zeigen gleichzeitig ein großes Anwendungspotential als nanoskopische Wärmequellen.

Zunächst wird das gestreute Licht der Nanopartikel als Indikator für die Strukturänderungen von Polymeren verwendet. Dazu werden Goldnanopartikel auf einer Polymeroberfläche positioniert und das Polymer geheizt. Ausgelöst durch eine Kontraktion des Polymers wird der Abstand zwischen den einzelnen Goldnanopartikeln reduziert, so dass sich gekoppelte plasmonische Resonanzen zwischen den Nanopartikeln zeigen.

Ein weiteres in dieser Arbeit verwendetes thermoresponsives Polymer verändert seine Wasserlöslichkeit bei einer Temperaturerhöhung über die untere kritische Lösungstemperatur. Dabei wird das Wasser aus dem Polymernetzwerk heraus getrieben, was mit einer Volumen- und Brechzahländerung des Polymernetzwerks verbunden ist. Diese Änderung wird zunächst durch die hohe Empfindlichkeit von Goldnanopartikeln bezüglich der Brechzahländerung untersucht und in weiteren Experimenten durch das plasmonische Heizen der Nanopartikel ausgelöst.

Plasmonisches Heizen von Goldnanopartikeln wird ebenfalls dazu verwendet, um eine Matrix eines Polymers kontrolliert optothermisch zu verändern. Dabei führt der hohe Temperaturanstieg zur thermischen Zersetzung des Polymers. Dieser Prozess lässt sich mit der Intensität des verwendenden Laserstrahls kontrollieren. Starke optische Kräfte werden genutzt, um ein einzelnes Goldnanopartikel in einem Poylmerfilm kontrolliert zu bewegen und so Nanokanäle zu erzeugen.

Ähnlich zum Prozess der thermischen Zersetzung eines Polymers, können plasmonisch geheizte Goldnanopartikel dazu angewandt werden, um die Kreuzvernetzung von Polymerketten zu beschleunigen. Die Größe der erzeugten Polymerstrukturen lässt sich mit der Dauer und Stärke des Heizprozesses steuern. Auch hier können die einzelnen Goldnanopartikel durch optische Kräfte bewegt werden. Hierbei entstehen Polymerfäden im Nanomaßstab.

Die in dieser Arbeit neu entwickelten Methoden, erlauben die gezielte Untersuchung und Manipulation von Polymereigenschaften auf der Nanoskala und bieten ein hohes Anwendungspotential im Bereich der Nanolithographie.

Contents

1 Introduction

The pure and shiny appearance of gold together with its outstanding malleability made it one of the most treasured materials in the cultural history of mankind. More than 1500 years ago people also discovered the intriguing optical properties of the metal by adding gold precursors to molten glass [1]. Depending on the manufacturing process, the glass appeared in colors ranging from red to purple [2]. The origin of the color was unknown until 1857, when an English scientist, Michael Faraday, connected the resulting color to the small size of gold nanoparticles [3]. Half a century later, the German physicist Gustav Mie published a theoretical paper about light scattering and absorption by small metallic structures, which exactly describes their size dependent optical properties [4]. Today, gold nanoparticles with dimensions between 1 and 100 nm and highly diverse shapes [5–8] are an established and well studied tool in the fast developing field of nanoscience [9–11].

The interaction of electromagnetic waves with gold is strongly influenced by the free electron gas of the metal. The incident light excites collective oscillations of free electrons, which are so-called surface plasmons [12, 13]. Localized surface plasmons inside gold nanoparticles change their optical properties compared to bulk gold. Due to the plasmon resonance, which is in the visible region of the electromagnetic spectrum, the amount of light scattered and absorbed by the gold nanoparticle increases drastically [10, 14, 15]. The strong sensitivity of the plasmon resonance to dielectric properties of the surrounding medium [16–18] and the local electric field enhancement due to increased electron concentration in certain parts of gold nanostructues [19, 20] constitute enormous sensing properties of plasmonic particles [21–24]. A drastic temperature increase of gold nanoparti-

cles by irradiating them with resonant light[1] allows their use as a light-controlled nanoscopic heat source [25, 26]. The applications of plasmonically heated gold nanoparticles span from thermally induced changes of material properties [27, 28] to cancer cell hyperthermia [29–31]. Additionally, the enlarged amount of the scattered and absorbed light leads to an increased transfer of photon momentum to the gold nanoparticle, which opens the door for resonant optical manipulations of gold nanoparticles, such as laser printing, stamping or sorting [32–35].

Gold nanoparticles can be used to manipulate polymers, which are natural or synthetic compounds that are built up by a long chain of repeating units. Highly diverse physical properties of synthetic polymers make them applicable in almost all fields of modern manufacturing. In terms of nanofabrication, polymers are developing into a highly interesting material. Nanostructured polymers play a role in photonics [36], for biomedical applications [37] and even photovoltaics [38]. Some of the modern polymer nanofabrication methods are connected to scanning probe techniques, such as thermomechanical writing or near field illumination [38, 39].

In this work we investigate how laser guided and plasmonically heated gold nanoparticles can be used as nanoscopic tools for polymer nanofabrication. Nanocomposites made from polymers and nanoparticles combine advantages of both materials: high sensing properties of gold nanostructures and tunable physical properties of polymers [40].

The physical background of the plasmonic properties is explained in chapter 2. This chapter starts with optical properties of gold nanoparticles and introduces how they lead to plasmonic heating and strong electromagnetic forces exerted by a strongly focused laser beam. In addition, we briefly present the computer based calculation methods, which are required for numerical modeling.

In chapter 3 we give a brief overview on the thermal properties of polymers. In particular, polystyrene (PS), polyvinyl alcohol (PVA), poly (N-isopropylacrylamide) (pNIPAM) and polydimethylsiloxane (PDMS) are introduced.

[1] The frequency of the incident electromagnetic wave corresponds to the plasmon resonance frequency of the gold nanoparticle.

The main focus of chapter 4 is the preparation and characterization of polymer-nanoparticle composites. Furthermore, spectroscopic and microscopic techniques to characterize and manipulate the samples are discussed and introduced.

The main findings of this work are discussed in two chapters. In the 5th chapter, plasmonic properties of gold nanoparticles and nanorods are employed to determine thermal properties of polymers. Initial experiments are based on external heating of the whole sample. In continuation, gold nanostructures act as local heat sources to the surrounding polymer. We compare the difference in thermal behavior of the polymer between localized and bulk heating.

The possibilities of using gold nanoparticles in terms of polymer nanopatterning are discussed in the 6th chapter. Plasmonic heating with a focused laser beam is applied to manipulate the polymer composites. We explain how nanoparticles are heated and guided simultaneously by a focused laser beam.

Chapter 7 concludes the work and gives an overview about possible future applications.

2 Gold nanoparticles and electromagnetic radiation

The metallic character of gold nanoparticles give rise to their extraordinary properties compared to dielectric particles of the same size. Free electrons of gold are excited by the oscillating electric field component of the incident visible light. The resulting collective oscillation of the free electron gas is called a plasmon [12]. In the case of gold nanoparticles, plasmons are confined in nanostructure dimensions and show a resonance in the visible region of light [10]. The frequency of the plasmon resonance depends on the size and shape of the nanoparticle [15]. In the following chapter we explain briefly the outstanding optical properties of gold nanoparticles.

Furthermore, computer based calculations provide for the comparison of the theoretically-predicted behavior of the system with experimental results. In particular, analytical and numerical methods are applied to calculate effective cross sections of gold nanoparticles, optical forces, and three-dimensional heat distributions due to plasmonic heating.

2.1 Optical properties of gold nanoparticles

The dielectric function of gold

Optical properties of gold nanoparticles can be best explained by looking at the dielectric function of the metal. The function describes the relationship of the incident electromagnetic wave and the irradiated structure. For metallic structures, the dielectric response is strongly determined by the free electrons. The basic theoretical description for free electrons in a metal is the Drude-Sommerfeld model [41, 42]. The idealistic model considers electrons, which interact only with the surrounding atomic nuclei. This assumption reduces the calculation to a one electron problem multiplied by the number density of free electrons. Using the mass of the electron m_e, the damping constant Γ, and the external field $\mathbf{E}(t)$, the equation of motion can be written as [41]:

$$m_e \frac{\partial^2 \mathbf{x}}{\partial t^2} + m_e \Gamma \frac{\partial \mathbf{x}}{\partial t} = -e\mathbf{E}(t). \tag{2.1}$$

The damping constant Γ is connected to the relaxation time of the free electron gas τ via the relation $\Gamma = 1/\tau$ and denotes the characteristic collision frequency of moving electrons with lattice vibrations (electron-phonon scattering). The value of the collision frequency for gold is typically in the region around 100 THz [43].

In order to solve the equation of motion (2.1) for oscillating electric fields (e.g. light), we replace the function $\mathbf{E}(t)$ with $\mathbf{E}_0 e^{-i\omega t}$, which has an amplitude $\mathbf{E}_0$ and a frequency ω. The solution of this modified equation is provided by a motion: $\mathbf{x}(t) = \mathbf{x}_0 e^{-i\omega t}$. This solution contains the complex amplitude $\mathbf{x}_0$, and its imaginary part describes the phase shift between the applied electric field and the response of the electrons due to the damping constant Γ:

$$\mathbf{x}(t) = \frac{e}{m_e(\omega^2 + i\Gamma\omega)} \mathbf{E}_0 e^{-i\omega t}. \tag{2.2}$$

The equation (2.2) characterizes the time dependent displacement of a free electron driven by an oscillating electric filed. The macroscopic polarization of a metal structure $\mathbf{P} = -Ne\mathbf{x}$ considers the contribution of the electron density N with the charge e, which are displaced by $\mathbf{x}$. In the next step, the macroscopic

polarization can be inserted into the equation of the electric displacement field [44]:

$$\mathbf{D} = \varepsilon_0 \mathbf{E} + \mathbf{P} = \varepsilon_0 \varepsilon \mathbf{E}. \tag{2.3}$$

This equation connects the electric displacement field $\mathbf{D}$ with the external electric field $\mathbf{E}$ using the vacuum permittivity ε_0, and the dielectric function of the material ε. In our case, the frequency dependent dielectric function $\varepsilon_{Drude}(\omega)$ is determined by a free electron gas inside the metallic structure:

$$\mathbf{D} = \varepsilon_0 \mathbf{E} - \frac{Ne^2}{m_e(\omega^2 + i\Gamma\omega)}\mathbf{E} = \varepsilon_0(1 - \frac{Ne^2}{\varepsilon_0 m_e(\omega^2 + i\Gamma\omega)})\mathbf{E}, \tag{2.4}$$

and

$$\varepsilon_{Drude}(\omega) = 1 - \frac{Ne^2}{\varepsilon_0 m_e(\omega^2 + i\Gamma\omega)} = 1 - \frac{\omega_P^2}{\omega^2 + i\Gamma\omega}. \tag{2.5}$$

In this equation we make a substitution using $\omega_P^2 = \frac{Ne^2}{\varepsilon_0 m_e}$. The frequency ω_P is called plasma frequency of the free electron gas [41]. The plasma frequency provides a deeper physical understanding of the optical material properties: at this frequency the real part of the dielectric function shows a change of sign. Below the plasma frequency, the real part of the dielectric function becomes negative, which means that the electric field cannot penetrate the metal and will be reflected or absorbed by its surface [44].

For noble metals, such as gold and silver, the dielectric function has to be corrected considering the strong positive background of ion cores. The correction is implemented by introducing the background permittivity ε_∞ to the dielectric function [41]:

$$\varepsilon_{Drude}(\omega) = \varepsilon_\infty - \frac{\omega_P^2}{\omega^2 + i\Gamma\omega}. \tag{2.6}$$

By plotting the theoretical dielectric function of gold from the equation (2.6) and comparing it to the measured values for the real and complex part of the dielectric function, we can observe a limitation of the Drude-Sommerfeld theory for gold in the wavelength region below 700 nm (figure 2.1).

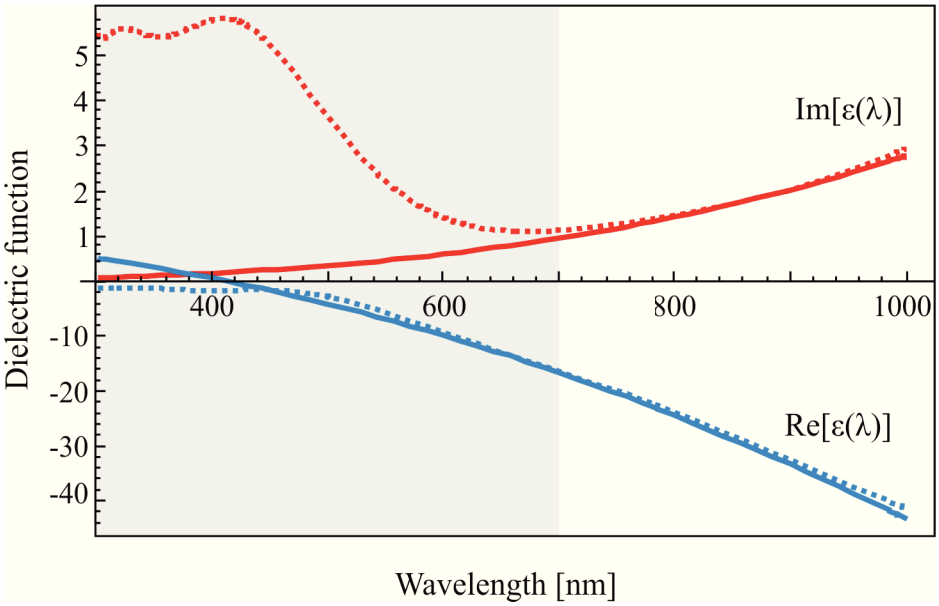

Figure 2.1: **Comparison of theoretical and experimental values of the dielectric function of gold.** The Drude-Sommerfeld model is calculated with the following values: $\varepsilon_\infty = 9$, $\omega_p = 1.36 \cdot 10^{16}$ Hz and $\Gamma = 100$ THz (solid lines) [43]. Experimental values are from the well-known measurement by Johnson and Christy (dashed lines) [45]. Blue color denotes the real and the red color imaginary parts of both dielectric functions. The region of the interband transition is marked with a gray background.

At wavelengths below 700 nm, the energy of the incident photons is sufficient to induce interband transitions. During this transition, electrons are excited from the lower energetic d-band to the sp-band of gold (inset in the lower left corner of figure 2.1). These material specific transitions are not takein into account by the theoretical model and can be corrected by introducing an additional term into the equation of motion (2.1). The correction term is represented by a bound electron with a resonance frequency ω_0 [41]:

$$m_e \frac{\partial^2 x}{\partial t^2} + m_e \Gamma \frac{\partial x}{\partial t} + m_e \omega_0^2 x = -e\mathbf{E}(t). \tag{2.7}$$

Depending on the region of validity, the experimental data or the theoretical model is used for calculations. The analytic expression provided by the Drude-Sommerfeld theory is used for calculations if the exciting wavelength is above

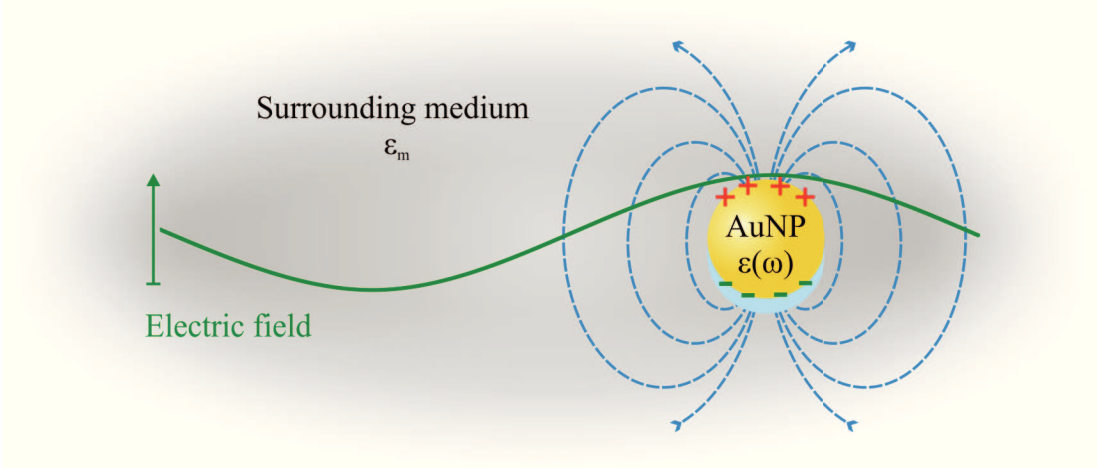

Figure 2.2: **A spherical gold nanoparticle with an incident electromagnetic wave.** The gold nanoparticle with a dielectric function $\varepsilon(\omega)$ is surrounded by a medium with a dielectric constant ε_m. The electric field component of the oscillating electromagnetic wave (green line) deflects free electrons of the gold nanoparticle (shown in blue) and polarizes it (green minuses and red pluses). At the same time, an electromagnetic field is induced around the gold nanoparticle due to the movement of electrons.

700 nm. For shorter wavelengths the experimental data points by Johnson and Christy are interpolated in order to calculate continuous dielectric functions.

Localized surface plasmons and the quasi-static approximation

Noble metal structures are considered a special case if their physical dimensions are much smaller than the wavelength of the incident electromagnetic wave. Firstly, the excited electron oscillation is confined inside the structure volume and cannot propagate away from the excitation area, as this is the case for bulk metal structures. Secondly, the amplitude of the incident electric field shows only small differences over the nanostructure volume, which results in an almost constant phase of all excited electrons [42]. According to these properties, the gold nanostructure can be considered as a nanoscopic antenna which receives and sends the incident electromagnetic wave [46](figure 2.2).

As mentioned before, collective oscillations of electrons inside a sub-wavelength metallic structure are called localized surface plasmons. Since only nanoscopic

structures are employed in this work, all plasmons and plasmonic properties mentioned in this thesis are referred to localized surface plasmons.

To calculate the interaction of a sub-wavelength metallic structure with the electromagnetic wave, the spacial phase of the oscillating electrons is considered to be constant over the structure volume. This assumption is called quasi-static approximation [42]. The most convenient geometry is a homogeneous sphere with a radius a and a dielectric constant ε, surrounded by an isotropic medium with a dielectric constant ε_m. The dielectric constant (also called relative permittivity) of a non-magnetic material is connected to its refractive index by $\varepsilon_m = n^2$ [44]. The incident electric field is static with the field intensity E_0. An analytical solution for the electric potential inside Φ_{in} and outside Φ_{out} the sphere is provided by equations (2.8) and (2.9) [41]. In both equations, the corresponding cylindrical coordinates are r and θ.

$$\Phi_{in} = -\frac{3\varepsilon_m}{\varepsilon + 2\varepsilon_m} E_0 r \cos\theta \tag{2.8}$$

$$\Phi_{out} = -E_0 r \cos\theta + \frac{\varepsilon - \varepsilon_m}{\varepsilon + 2\varepsilon_m} E_0 a^3 \frac{\cos\theta}{r^2} \tag{2.9}$$

The equation 2.9 describes the electric potential corresponding to the applied electric field in the first term and the contribution of a dipole in the second term. In comparison, a general definition of a dipole potential in each point $\mathbf{r}$ is based on the dipole moment $\mathbf{p}$ and the corresponding distance to the dipole center r [44]:

$$\Phi_{Dipol}(\mathbf{r}) = \frac{\mathbf{pr}}{4\pi\varepsilon_0\varepsilon_m r^3} = \frac{pr\cos\theta}{4\pi\varepsilon_0\varepsilon_m r^3}. \tag{2.10}$$

This equation can be combined with the equation (2.9) which leads to the expression for a dipole moment of a dipole, that is located in the center of the previously introduced sphere:

$$\mathbf{p} = 4\pi\varepsilon_0\varepsilon_m a^3 \frac{\varepsilon - \varepsilon_m}{\varepsilon + 2\varepsilon_m} \mathbf{E}_0. \tag{2.11}$$

Per definition, the dipole moment is connected to the external electric field via the electric permittivity of vacuum ε_0, the permittivity of the surrounding medium ε_m and the polarizability coefficient of the dipole α:

$$\mathbf{p} = \varepsilon_0 \varepsilon_m \alpha \mathbf{E}_0. \tag{2.12}$$

This relation allows us to extract the size and the permittivity-dependent polarizability of a sphere from the equation (2.11):

$$\alpha = 4\pi a^3 \frac{\varepsilon - \varepsilon_m}{\varepsilon + 2\varepsilon_m}. \tag{2.13}$$

This equation (2.13) is known as Clausius-Mossotti equation. A closer look at this equation provides important information about the frequency dependent behavior of the nanoparticle polarizability. As introduced in the previous section, the dielectric function of gold depends on the excitation frequency. At certain frequencies the polarizability shows a resonance behavior which occurs for minimal values of $|\varepsilon(\omega) + 2\varepsilon_m|$ [41]. This resonance, which is called the Fröhlich condition, is met for $Re[\varepsilon(\omega)] = -2\varepsilon_m$, assuming a small and slowly-varying imaginary part of the dielectric function. The complex polarizability of the nanostructure plays a significant role in the next chapter, since the electromagnetic force on a gold nanoparticle is directly connected to the nanoparticle polarizability.

We use the experimental dielectric function of bulk gold (Johnson and Christy [45]) to calculate the complex polarizability for different excitation wavelengths. The resulting polarizability of an 80 nm gold nanoparticle in water is shown in figure 2.3. The plot clearly denotes the resonantly enhanced complex polarizability in a region around 540 nm. This plasmonically-increased polarizability affects the amount of scattered and absorbed light by the nanostructure.

Effective cross section of gold nanostructures

The scattering cross-section of a gold nanoparticle is calculated by dividing the total scattered or extinct power by the intensity of the incident light, which leads to expressions [41, 42]:

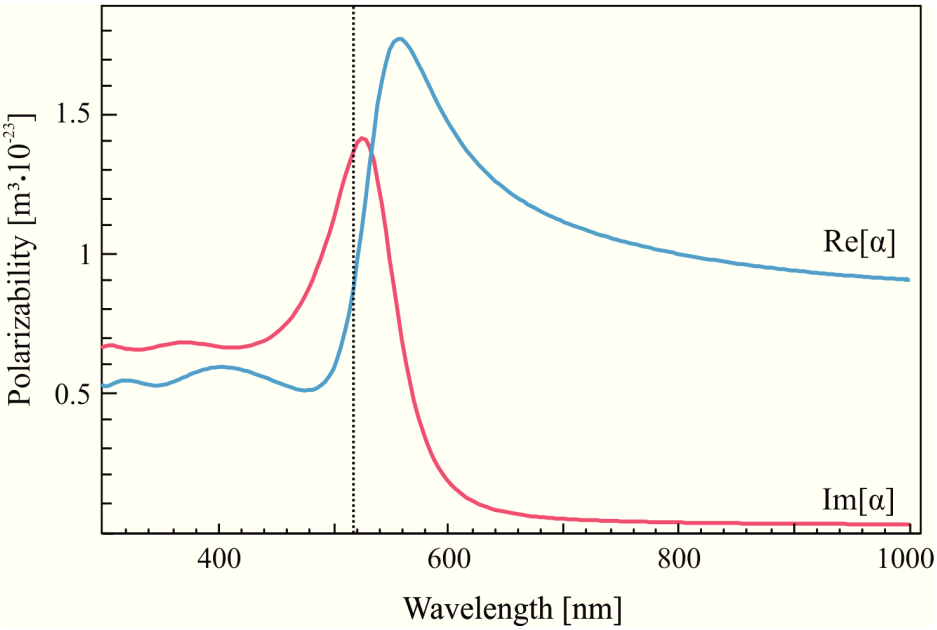

Figure 2.3: **Complex polarizability of a spherical gold nanoparticle in water.** The diameter of the gold nanoparticle is 80 nm and the dielectric constant of water is $\varepsilon_m = 1.33^2$. The Fröhlich condition is met at 516 nm (denoted by a vertical dashed line).

$$\sigma_{sca} = P_{sca}/I_{inc} = \frac{k^4}{6\pi}|\alpha|^2, \tag{2.14}$$

$$\sigma_{ext} = P_{ext}/I_{inc} = k\,\mathrm{Im}[\alpha]. \tag{2.15}$$

The extinction cross section contains both, the scattering and the absorption cross sections: $\sigma_{ext} = \sigma_{sca} + \sigma_{abs}$. Therefore, the absorption cross section σ_{abs} can be easily obtained from equations (2.15) and (2.14). These calculations are performed considering vacuum conditions. In a case of another surrounding media, the incident wavelength, and thus the wavenumber, must be corrected by the refractive index of the medium.

It is possible to calculate the complex polarizability of spherical gold nanoparticles by using the experimental dielectric function [45] and the Clausius-Mossotti equation (2.13). Together with this polarizability, equations (2.15) and (2.14)

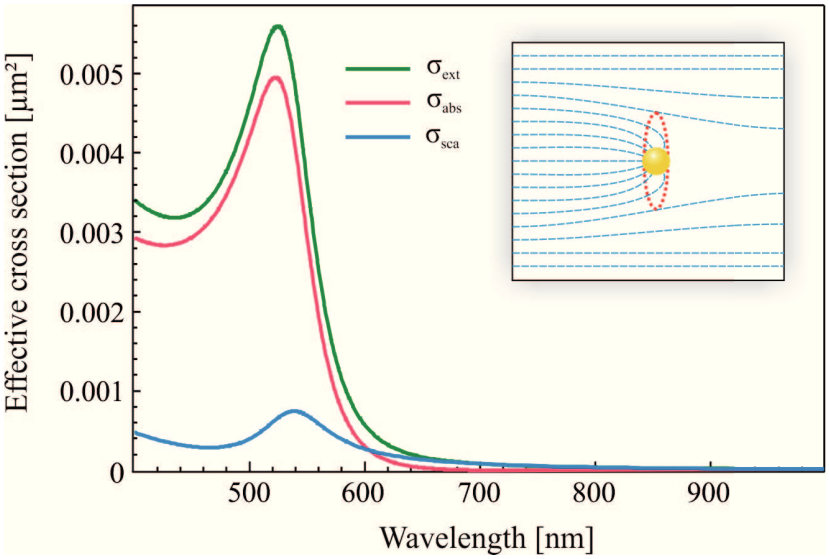

Figure 2.4: **Effective cross section of a gold nanoparticle.** The diameter of the gold nanoparticle is 50 nm. The surrounding medium is water. The inset in the top right corner illustrates the idea of an effective cross section: the incident intensity is blocked by an object with the surface area, that is equal to the effective cross section.

provide wavelength dependent effective cross sections of a gold nanoparticle with 50 nm diameter surrounded by water.

Figure 2.4 illustrates the effective cross sections of the largest nanoparticle, which can be calculated using the Clausius-Mossotti equation without any restriction. For nanoparticle diameters above 50 nm, the value of the scattering cross section becomes bigger than the extinction cross section, in the wavelength region between 600 and 800 nm. This leads to unphysical negative numbers for the absorption cross section. The same behavior is observed by introducing surrounding media with $\varepsilon_m > 1.33^2$. Therefore, a more precise solution is required to calculate more realistic effective cross sections of particles with diameters bigger than 50 nm in a high refractive surrounding media.

Mie theory

The Mie theory assumes an optically isotropic spherical particle with a radius a and a complex refractive index m, irradiated with a plane harmonic electro-

magnetic wave at a wavelength λ. This theory considers not only the dipole contribution, as in the case of the quasi-static approximation, but also the contribution of higher orders of multipole expansion. Boundary conditions for the electromagnetic wave at the edge of the sphere lead to exact expressions for scattering and extinction cross sections [42]:

$$\sigma_{sca} = \frac{2\pi}{|k|^2} \sum_{j=1}^{\infty} (2j+1)(|a_j|^2 + |b_j|^2), \tag{2.16}$$

$$\sigma_{ext} = \frac{2\pi}{|k|^2} \sum_{j=1}^{\infty} (2j+1) Re(|a_j| + |b_j|). \tag{2.17}$$

In these equations, $k = 2\pi/\lambda$ is the wavenumber of the incident wave. The scattering coefficients a_j and b_j are

$$a_j = \frac{m\psi_j(mx)\psi_j'(x) - \psi_j(x)\psi_j'(mx)}{m\psi_j(mx)\xi_j'(x) - \xi_j(x)\psi_j'(mx)}, \tag{2.18}$$

$$b_j = \frac{\psi_j(mx)\psi_j'(x) - m\psi_j(x)\psi_j'(mx)}{\psi_j(mx)\xi_j'(x) - m\xi_j(x)\psi_j'(mx)}, \tag{2.19}$$

where $x = \frac{2\pi a}{\lambda}$ is the size parameter of the sphere. The functions ψ_j and ξ_j are the Riccati-Bessel functions. For particle sizes smaller than the wavelength of the incident electromagnetic wave, it is sufficient to calculate only the first few terms of the series in equations (2.16) and (2.17).

The scattering and extinctions cross sections are depending on the complex polarizability of a gold nanoparticle, as described by equations (2.14) and (2.15). Using these equations, expressions for the real α' and imaginary α'' parts of the polarizability can be derived according to:

$$\alpha' = \sqrt{\frac{\sigma_{sca} 6\pi}{k^4} - \frac{\sigma_{ext}^2}{k^2}}, \tag{2.20}$$

$$\alpha'' = \frac{\sigma_{ext}}{k}. \tag{2.21}$$

Comparison of the complex polarizability provided by the Clausius-Mossotti expression and the values calculated by using the Mie theory denotes again the limited validness of the quasi-static approximation (figure 2.5).

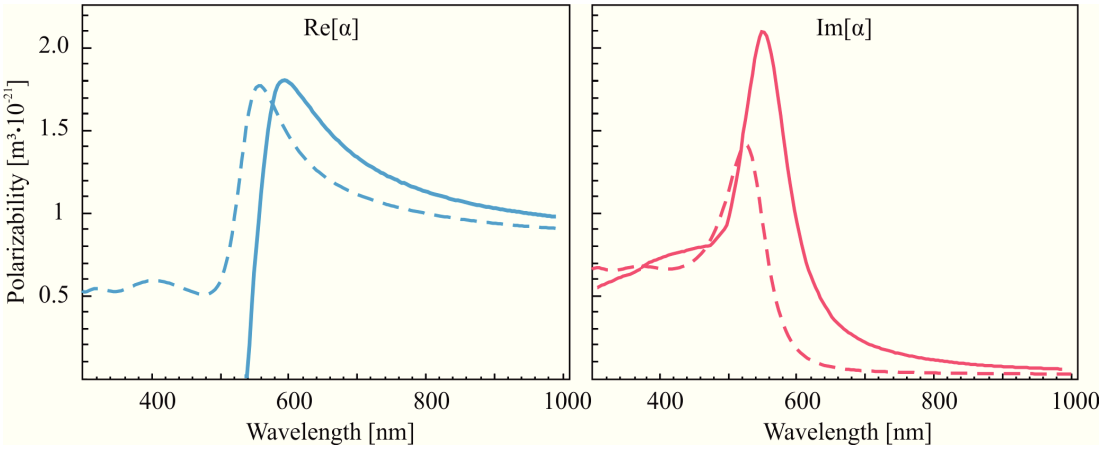

Figure 2.5: **Complex polarizability of a gold nanoparticle.** Different ways to calculate the real (blue lines) and the imaginary (red lines) parts of a nanoparticle polarizability (80 nm diameter in water). Solid lines correspond to the Mie theory. Dashed lines shows results by the quasi-static approximation.

The Clausius-Mossotti equation does not take some important size dependent plasmonic effects, such as a red shift of the plasmon resonance for bigger particles due to the retardation effect, into account [47]. The retardation effect occurs when the the phase of the incident electromagnetic field cannot be assumed as constant over the nanoparticle volume which leads to excitation of higher orders of multipol excitation. This effect is usually observed for a structure size $a > \lambda/10$, compared to the incident wavelength λ. Other significant effects, such as absorption and radiation damping are also not considered [41], which explains the big difference shown in figure 2.5.

Additionally, the real part of the nanoparticle polarizability, calculated with the Calusius-Mossotti equation, is positive over the whole visible wavelength range. The real part of the polarizability, provided by the Mie theory, suggests a change of sign (solid blue line in figure 2.5). The change of sign occurs in a wavelength region below the plasmon resonance. Negative values of the real part of the

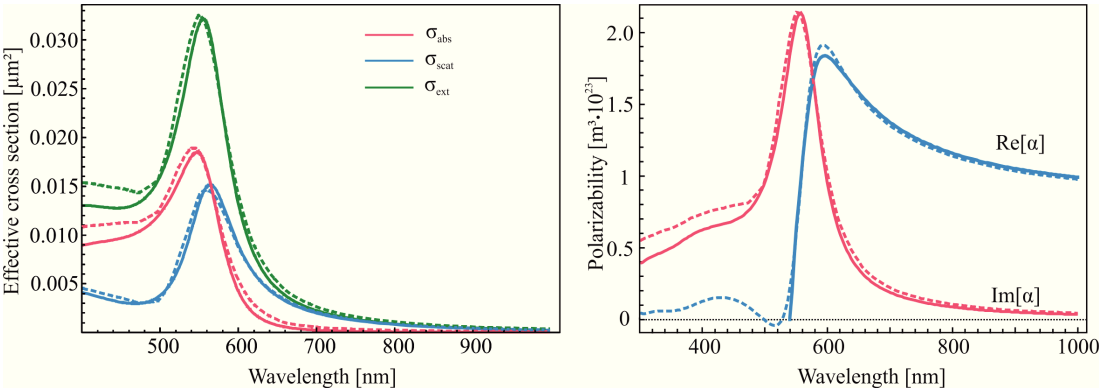

Figure 2.6: **Effective cross sections and complex polarizability of a gold nanoparticle.** The diameter of the gold nanoparticle is 80 nm and the surrounding medium is water. The values represented by solid lines are calculated with the Mie theory. The dashed lines are calculated with the extended quasi-static approximation.

polarizability is a substantial feature, which plays a role during experiments with electromagnetic forces acting on gold nanoparticles as shown in next sections.

Extending the quasi-static approximation

The quasi-static approximation is limited for gold nanoparticles bigger than 50 nm and for surrounding media with high dielectric constants ($\varepsilon_m > 1.33^2$). An alternative expression for the polarizability of a metallic nanosphere is proposed by Kuwata et al. [48]:

$$\alpha_{ext} = V_p \frac{1 - \frac{1}{10}(\varepsilon + \varepsilon_m)(x)^2 + O(x^4)}{(\frac{1}{3} + \frac{\varepsilon_m}{\varepsilon - \varepsilon_m}) - \frac{1}{30}(\varepsilon + 10\varepsilon_m)(x)^2 - i\frac{16\varepsilon_m^{3/2}}{9}(x)^3 + O(x^4)}. \tag{2.22}$$

In this equation, V_p is the volume of the sphere, $x = 2\pi a/\lambda$ is the size parameter, a is the radius of the sphere, and λ is the wavelength in vacuum. O contains higher orders of the size parameter.

Complex polarizabilities of an 80 nm gold nanoparticle surrounded by water and calculated by the extended equation (2.22) and the Mie Theory are in a very good agreement to each other. Comparing the effective cross-sections by both

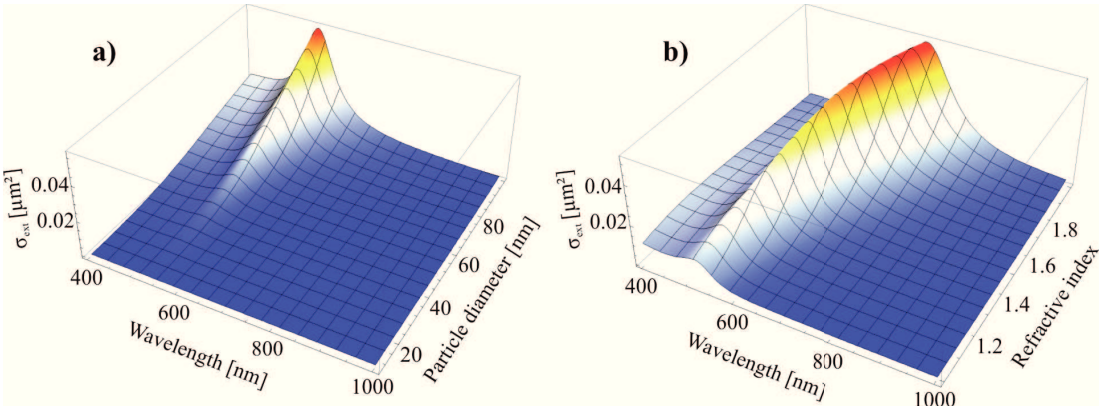

Figure 2.7: **Extinction cross section of spherical gold nanoparticles** a) The increase, broadening and red shift of the plasmon resonance of spherical gold nanoparticles with a diameter between 10 and 100 nm in water. b) The Increase and strong redshift of extinction cross sections of an 80 nm gold nanoparticle for a varying refractive index of the surrounding medium.

methods shows a very good agreement. Figure 2.6 illustrates the comparison of the extended polarizability and Mie theory. The extended polarizability equation (2.22) is used in the following chapters to calculate the complex polarizability, effective cross sections, and the electromagnetic force on gold nanoparticles.

Figure 2.7 illustrates two important dependences of the plasmon resonance for spherical gold nanoparticles. Panel (a) shows the increase, the broadening and the red shift of the plasmon resonance with increasing particle radius. In this graph, the refractive index of the surrounding medium is constant with n = 1.33. Panel (b) shows the increase and the strong redshift of the plasmon resonance of a spherical 80 nm gold nanoparticle as a function of the refractive index of the surrounding medium.

Among all optical properties, the existence of an absorption cross section denotes that a fraction of the incident electromagnetic energy will remain inside the nanostructure. Depending on material properties, a bigger or smaller fraction of the absorbed energy can therefore cause a substantial temperature increase. The high absorption cross section of gold nanoparticles, thus makes them the perfect candidates to be applied as a nanoscopic heat source.

2.2 Plasmonic heating

A rather low quantum efficiency of gold nanoparticles in terms of photoluminescence [49] leads to the transfer of almost all absorbed electromagnetic radiation into heat. The heating effect is proportional to the increasing effective absorption cross section in the region of the plasmon resonance [50].

The energy of the excited plasmon decays two possible ways, a radiative decay, which corresponds to the elastic scattering of light and a non-radiative decay, which results into the temperature increase of the gold nanoparticle. In detail, the non-radiative decay of the gold nanoparticle plasmon is connected to incoherently oscillating electrons and transfers the plasmon energy to phonons due to electron-electron and electron-phonon interaction [42]. The result of this process is an increasing temperature of the gold nanoparticle. Due to the high thermal conductivity of gold, the temperature distribution over the whole gold nanoparticle volume can be considered as constant (shown schematically in figure 2.8).

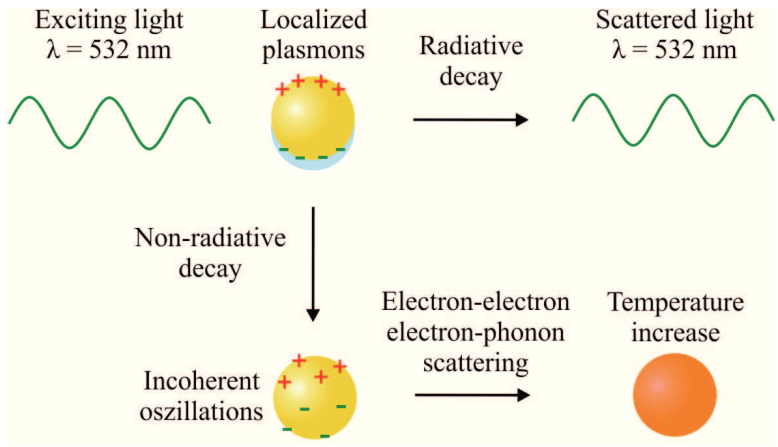

Figure 2.8: **Decays of the localized surface plasmon.** The radiative decay results in elastically scattered light of the same wavelength as the incident light. The non-radiative decay is connected to the loss of phase of oscillating electrons. Following electron-electron and electron-phonon interactions lead to the temperature increase of the gold nanoparticle.

The generated heat diffuses away from the hot gold nanoparticle surface, which leads to the increase of the temperature around the gold nanoparticle. The diffusion of heat is described by the following equation [50]:

$$\rho(\mathbf{r})c(\mathbf{r})\frac{\partial T(\mathbf{r},t)}{\partial t} = \nabla\kappa(\mathbf{r})\nabla T(\mathbf{r},t) + Q(\mathbf{r},t), \tag{2.23}$$

where $T(\mathbf{r},t)$ is the temperature at the point with the coordinate $\mathbf{r}$ at time t, $\rho(\mathbf{r})$ the density, $c(\mathbf{r})$ the heat capacity and $\kappa(\mathbf{r})$ the thermal conductivity of the surrounding material. In our experiments, the heat source $Q(\mathbf{r},t)$ is always represented by the gold nanoparticle, which absorbs a fraction of the incident laser irradiation.

When irradiated by a continuous wave laser, the gold nanoparticle generates a constant amount of thermal energy. At the same time, the amount of the heat transferred to the surroundings depends on the temperature gradient, which is increasing for higher nanoparticle temperatures. The point where the temperature distribution inside the system is constant in time, the thermal steady-state is achieved.

The steady-state temperature increase around a spherical gold nanoparticle with a volume V_P acting as a heat source with a constant thermal energy Q depends on the thermal conductivity of the surrounding medium k_0 and the distance to the nanoparticle surface r [50]:

$$\Delta T(r) = \frac{QV_P}{4\pi k_0 r}. \tag{2.24}$$

This equation has its validity only for distances r bigger than the radius of the gold nanoparticle. The amount of the absorbed heat Q is calculated by using the previously introduced absorption cross section of the gold nanoparticle:

$$Q = \frac{\sigma_{abs} I}{V_P}. \tag{2.25}$$

In this equation I is the power density of the incident electromagnetic wave.

Simulating heat distributions around hot gold nanoparticles

The heat distribution around spherical heat sources with an isotropic heat conductance can be calculated analytically by applying symmetry simplifications (equation 2.24). All relevant values are assumed to be constant at different temperatures. Nevertheless, the heat distribution for asymmetric geometries has usu-

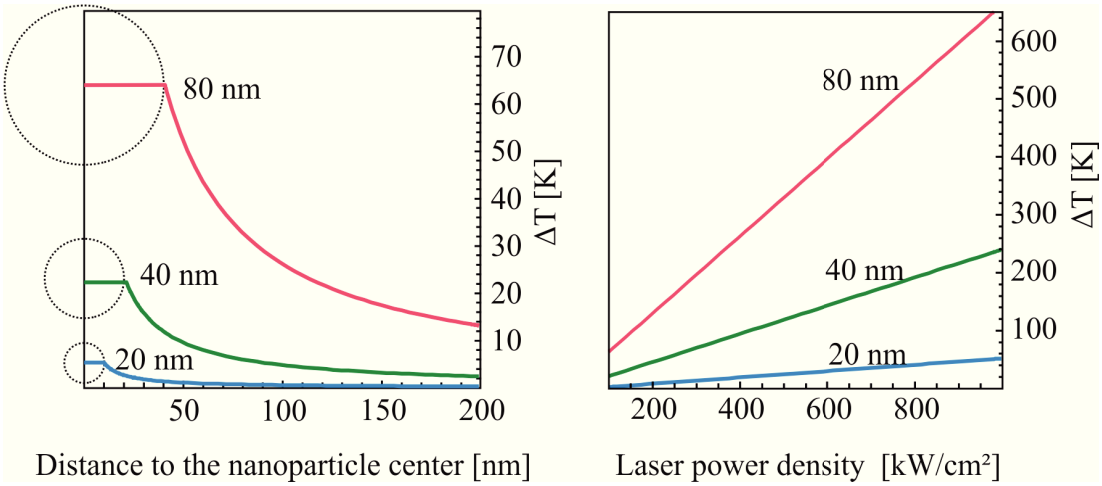

Figure 2.9: **Calculated temperature increase of the surroundings and the surface of the gold nanoparticle in water.** Left panel shows the temperature increase as a function of the distance to the nanoparticle center for different nanoparticle diameters and 100 kW/cm^2 heating power density. Right panel illustrates the temperature increase of the gold nanoparticle surface for different power densities and nanoparticle diameters.

ally no analytical solution and can only be calculated numerically. Additionally, relevant material properties, such as the heat capacity and thermal conductivity, show a temperature dependent behavior which makes the calculation significantly extensive.

It is therefore important to distinguish the exact amount of light absorbed by a gold nanoparticle. For this calculation the effective absorption cross section of the nanoparticle and the laser intensity are required. Effective cross sections are calculated by the program "MQMie" version 3.2a by Dr. Michael Quinten [51]. It provides exact solutions of the Mie theory for coated spherical particles of defined materials surrounded by different media. Alternatively, it is possible to use the extended polarizability equation (2.22) and absorption cross section from equations (2.15) and (2.14) for bare gold nanoparticles. The exact value of the laser intensity is calculated by taking a picture of the laser spot in the focal plane of the objective. Afterwards, the image of the spot is measured and approximated by a two-dimensional Gaussian function to calculate the power distribution in the spot. It is assumed that the gold nanoparticle is placed exactly in the middle

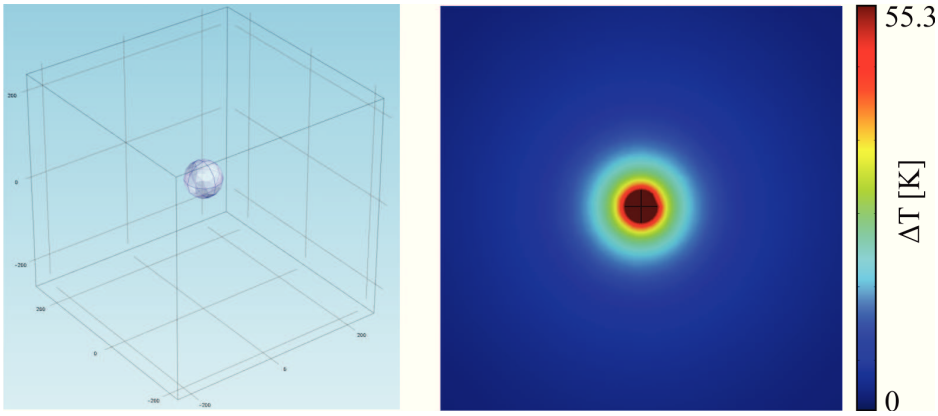

Figure 2.10: **Numerical calculation of the temperature distribution around a hot gold nanoparticle.** a) The experimental geometry is built inside the program. b) A cut through a three-dimensional temperature distribution simulation around a spherical gold nanoparticle. The diameter of the nanoparticle is 80 nm, the surrounding medium is water and the laser intensity is 1 mW. The heating laser beam is focused by an objective with an NA of 0.9.

of the laser spot and the intensity of the central area, which is equal to the absorption cross section, is absorbed by the nanoparticle. Dividing the absorbed power by the nanoparticle volume leads then to the required power density Q.

A commercial program "Comsol Multiphysics" version 4.0 by FemLab, is used to solve the heat diffusion equation numerically for arbitrary geometries and material properties. This program applies the method of finite elements, which divides the simulated volume into small triangular elements and solves individual heat diffusion equations for defined boundary conditions between each element [52]. Therefore, the correct definition of all boundary conditions plays an important role. Factors, such as heat transfer or insulation between single structures, constant temperatures or heat sources must be consistent with realistic conditions. The total simulation volume is defined to be big so outer boundary conditions can be held constant without disturbing the simulation.

The exact geometry of the sample area of interest is built inside the program. The material properties, such as heat capacity and thermal conductivity are of high importance to provide temperature values comparable with the experimental results.

The program allows to calculate both the steady-state and time dependent temperatures for arbitrary heat sources and geometries.

2.3 Optical forces

In order to understand the electromagnetic force acting on an object by an incident laser beam, also referred to as optical force, three important object size regimes have to be considered. Firstly, the Rayleigh regime, which corresponds to the situation when the size of the object is much smaller than the incident wavelength $a << \lambda$ [53]. This regime describes the interaction of light with molecules and shows the prominent scattering intensity dependence to $1/\lambda^4$. Secondly, the geometrical optics regime, which represents the interaction of light with non-absorbing particles with $a >> \lambda$ [54]. At this point, the origin of optical forces can be described in terms of ray optics. A transparent sphere refracts the incident light and changes its direction and momentum, which leads to a force pointing in the opposite direction. This force pulls the object into the region of the maximal intensity of light, where the incident beam is not refracted by the object. In the ray optics regime the size of the object is usually bigger than the size of the light beam. Thirdly, a special case between the ray optics and Rayleigh regimes, which is the Mie regime. The Mie regime is characterized by the interaction of light with objects with $a \approx \lambda$, which corresponds to all experiments done in this work [55]. Figure 2.11 gives an overview on all three regimes. In order to visualize the processes, the illustrated width of the beam corresponds to the wavelength of the electromagnetic wave. In all three cases the beam propagation direction is from top to the bottom.

One of the possible approaches to calculate the optical force on an object is the consideration of a Lorentz force on a dipole [56]. The classical expression for the Lorentz force on a moving object with speed $\mathbf{v}$ and charge q, depends on the electric and magnetic fields $\mathbf{E}$ and $\mathbf{H}$ [44]:

$$\mathbf{F}_{Lorentz} = q(\mathbf{E}(\mathbf{r},t) + \mathbf{v}(\mathbf{r},t) \times \mu_0 \mathbf{H}(\mathbf{r},t)). \tag{2.26}$$

In this equation $\mu_0 = 4\pi 10^{-7} N/A^2$ is the vacuum permeability.

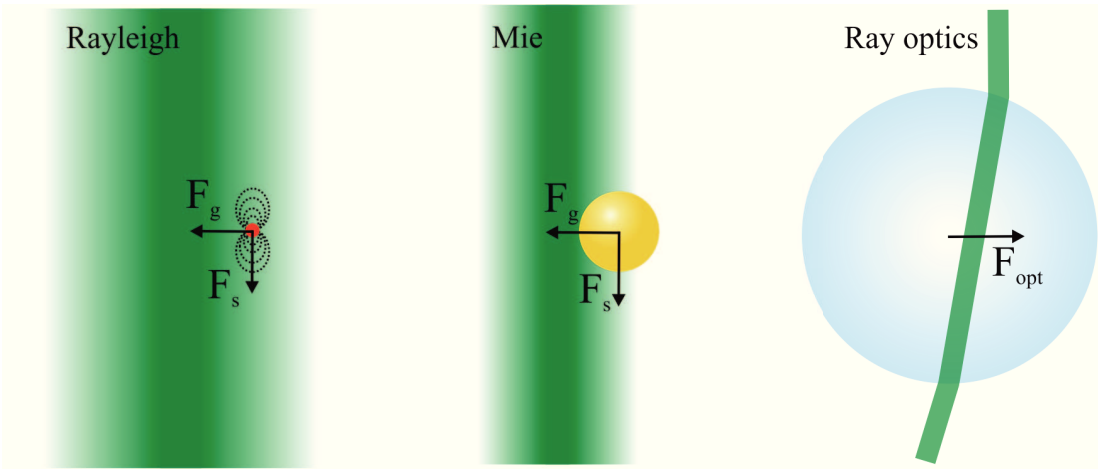

Figure 2.11: **Different regimes of optical forces on an object.** Left: the Rayleigh regime, with a very small object inside the laser beam. Middle: Mie regime, the size of the object is on the order of the incident wavelength. Right: the ray optics regime. The size of the particle is considerably bigger than the wavelength and the beam diameter.

In the case of a dipole with a dipole moment $\mathbf{p} = \varepsilon_0 \varepsilon_m \alpha \mathbf{E}$, the Lorentz force can be written as [57]:

$$\mathbf{F}_{dipole} = (p \cdot \nabla)\mathbf{E} + \mu \frac{d\mathbf{p}}{dt} \times \mathbf{H}. \tag{2.27}$$

In this equation, we use the dipole approximation for electric and magnetic fields. With the Maxwell equations and the vector equality, the total force equation can be represented as a function of the electric and magnetic fields:

$$\mathbf{F}_{total} = \varepsilon_0 \varepsilon_m \alpha [\sum_j E_j \nabla E_j + \mu \frac{\partial}{\partial t}(\mathbf{E} \times \mathbf{H})]. \tag{2.28}$$

Using the real α' and imaginary α'' parts of the extended complex polarizability and averaging over the optical period $T = 2\pi/\omega$, an equation is obtained which is only depending on the electric field:

$$\langle \mathbf{F}_{total} \rangle = \frac{1}{4} \varepsilon_0 \varepsilon_m \alpha' \nabla (\mathbf{E}^* \mathbf{E}) + \frac{1}{2} \varepsilon_0 \varepsilon_m \alpha'' \, \mathrm{Im} \left\{ \sum_j E_j^* \nabla E_j \right\}, \tag{2.29}$$

where * denotes the complex conjugate.

The total force can be decomposed into two important components, the gradient force

$$\langle \mathbf{F}_{grad} \rangle = \frac{1}{4} \varepsilon_0 \varepsilon_m \alpha' \nabla (\mathbf{E}^* \mathbf{E}), \tag{2.30}$$

and the scattering force

$$\langle \mathbf{F}_{scat} \rangle = \frac{1}{2} \varepsilon_0 \varepsilon_m \alpha'' \operatorname{Im} \left\{ \sum_j E_j^* \nabla E_j \right\}. \tag{2.31}$$

The gradient force depends on the real part of the complex polarizability and follows the gradient of the intensity. The gradient force usually acts towards the region with the highest light intensity. The gradient force is used to confine structures with a strongly focused laser beam, which shows high intensity gradients around the focal point. This confinement leads to optical trapping or optical tweezing.

The scattering force depends on the imaginary part of the complex polarizability and follows the Poynting vector $\mathbf{S}$ of the incident electromagnetic radiation. Alternatively, the scattering force is described by [58]:

$$\langle \mathbf{F}_{scat} \rangle = \frac{\varepsilon_m^2}{c} (\sigma_{scat} + \sigma_{abs}) \langle \mathbf{S} \rangle. \tag{2.32}$$

The name scattering force is rather misleading, since it contains both forces acting on a metallic nanoparticle due to the scattered and absorbed light [56].

The dependence of the gradient force on the real part, and the scattering force on the imaginary part of the polarizability allows different regimes of optomechanical manipulations (figure 2.12). Using different ratios of the real and complex polarizabilities, the ratio of the gradient and scattering force can be adjusted by applying different wavelengths of the incident light. For gold nanoparticles in the order of tens of nanometers, the real part of the complex polarizability dominates in the long wavelength region around 900–1000 nm. This region is marked by a vertical orange line. It is possible to confine gold nanoparticles in three dimensions using a strongly focused laser beam with these wavelengths.

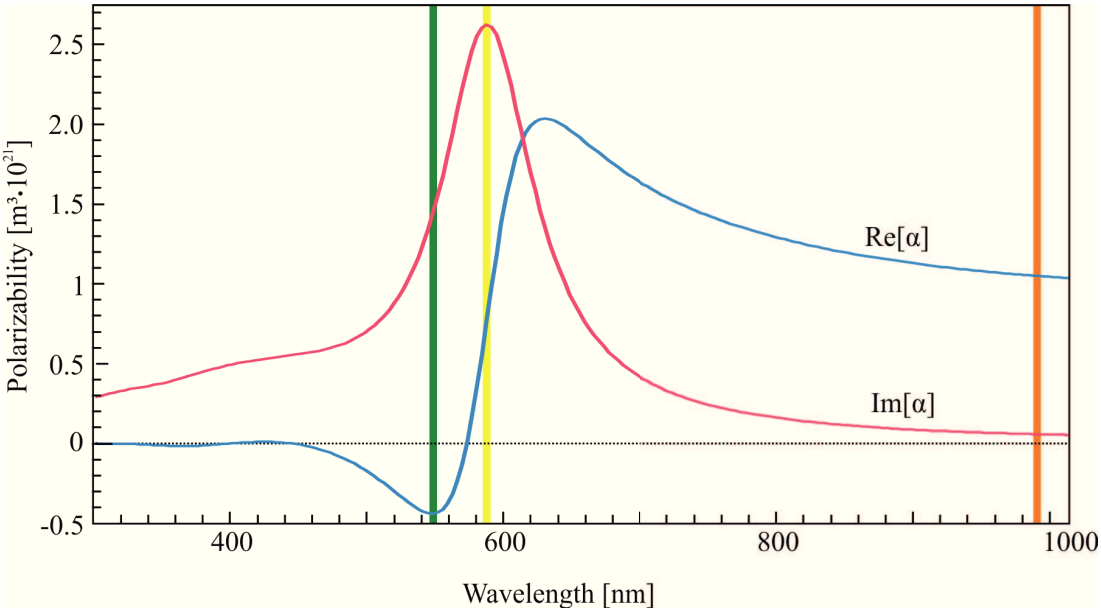

Figure 2.12: **Complex polarizability of a gold nanoparticle in a medium with a high refractive index.** The diameter of the gold nanoparticle is 80 nm, the refractive index of the medium is 1.5. The blue curve represents the real part and the red curve is the imaginary part of the polarizability. The green vertical line marks the region with the maximal repulsive gradient force, the yellow line the region with the maximal scattering force and the orange line marks the region of the mainly attractive gradient force.

In the wavelength regions close to the plasmon resonance (yellow line), the dominating imaginary part of the polarizability leads to the strong scattering force, which overcomes the gradient force and accelerates the gold nanoparticle along the beam propagation direction.

Additionally, the real polarizability of plasmonic nanoparticles can also obtain negative values. The negative value results in a change of the gradient force form attractive to repulsive. It occurs at wavelengths blue shifted compared to the plasmon resonance (figure 2.12, green line). In this case, the gold nanoparticle is not attracted by the gradient force anymore, but repelled from the region with the highest intensity. The gold nanoparticle follows the negative gradient of the electric field and optical trapping or confinement with a focused Gaussian beam is possible.

To be able to confine the gold nanoparticle with an incident wavelength in the region of negative real polarizability, special beam shapes like a hollow beam (Laguerre-Gaussian laser mode [59]) can be used [56]. In this case, the movement of the gold nanoparticle is limited inside the low intensity region in the focus of the beam. A similar principle is applied to trap atoms with blue detuned optical traps [60, 61].

Calculation of optical forces

To calculate the resulting optical forces on a plasmonic nanostructure, the optical force equations have to be solved for the case of a tightly focused laser beam. All force calculations are done with a commercial program for mathematical calculations "Mathematica" version 8.0 by Wolfram Research.

The electric field distribution of a focused laser beam in cylindrical coordinates, depending on the radius r and height z, can be described using the following equation [62]:

$$E(r,z) = E_0\sqrt{2/\pi}\frac{w_0}{w}e^{-\frac{r^2}{w^2}}e^{i(k(\frac{r^2}{2R}+z)+\eta)}, \tag{2.33}$$

where λ is the wavelength of incident light and $k = 2\pi n/\lambda$ is the wave vector inside the medium. The propagation direction of the laser beam is the z-direction. E_0 is the maximum electric field amplitude in the focus provided by

$$E_0 = \frac{\sqrt{2\mu_0 c_0 P}}{w_0}, \tag{2.34}$$

with the laser power P, the permeability of the free space μ_0, the speed of light in vacuum c_0, the width of the beam along the z-axis w, and at the focal plane w_0:

$$w_0 = \frac{\lambda}{\pi NA}, \qquad w(z) = w_0\sqrt{1+(z/z_0)^2}. \tag{2.35}$$

The equations contain NA, the numerical aperture of the focusing objective, described before (equation 4.1), and z_0, which is the length at which the beam cross section area doubles:

$$z_0 = \frac{\pi w_0^2 n}{\lambda}. \tag{2.36}$$

R and η are connected to z_0 and z-coordinate:

$$R = z(1 + \left(\frac{z_0}{z}\right)^2) \quad and \quad \eta = tan^{-1}\left(\frac{z_0}{z}\right). \tag{2.37}$$

The electric field equation can be applied on the optical force equations for the gradient force (2.30) and scattering force (2.31).

In order to plot the direction dependent optical force on a gold nanoparticle, we split the resulting optical force equations into components parallel to both coordinates r and z [62]. This leads to four expressions, the gradient force into z-direction:

$$F_{gradZ}(r,z) = -\frac{\varepsilon_0}{\pi}\alpha' E_0^2 \frac{z w_0^4}{z_0^2}\left(\frac{1}{w^4} - \frac{2r^2}{w^6}\right) e^{-\frac{2r^2}{w^2}}, \tag{2.38}$$

the gradient force into r-direction:

$$F_{gradR}(r,z) = -\frac{2\varepsilon_0}{\pi}\alpha' E_0^2 \frac{r w_0^2}{w^4} e^{-\frac{2r^2}{w^2}}, \tag{2.39}$$

the scattering force into z-direction:

$$F_{scatZ}(r,z) = \frac{\varepsilon_0}{\pi}\alpha'' E_0^2 \frac{w_0^2}{w^2}\left(k\left(1 - \frac{r^2}{2}\frac{z^2 - z_0^2}{(z^2 + z_0^2)^2}\right) + \frac{w_0^2}{z_0 w_0^2}\right) e^{-\frac{2r^2}{w^2}}, \tag{2.40}$$

and the scattering force into r-direction:

$$F_{scatR}(r,z) = \frac{\varepsilon_0}{\pi}\alpha'' E_0^2 \frac{r w_0^2}{w^2}\frac{k}{R} e^{-\frac{2r^2}{w^2}}, \tag{2.41}$$

Cross-sections of optical forces in z and r-directions acting on a spherical gold nanoparticle with 80 nm diameter irradiated by a 1 mW focused laser beam in water are calculated with previous equations (2.38-2.41) and shown in figure 2.13.

At this point should be mentioned that these calculations represent an approximated, idealistic situation. The real focused laser beam shows diffraction

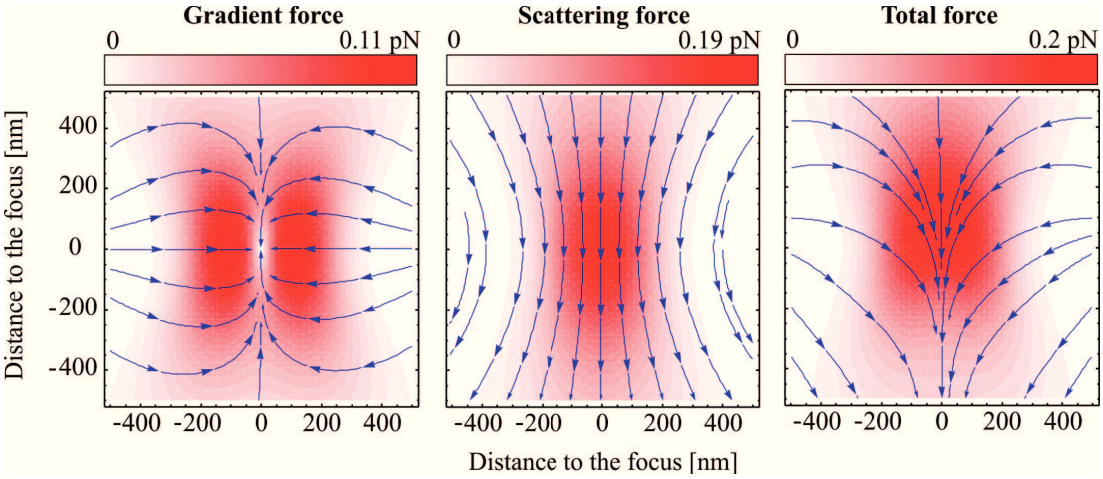

Figure 2.13: **Optical forces acting on a spherical gold nanoparticle.** Plots of the gradient, scattering, and the total force applied by a laser beam on a 80 nm gold nanoparticle in water. The laser beam with a wavelength of 632 nm is focused by a NA 0.9 objective. The laser power is 1 mW. In all plots, the arrows denote only the direction of the force, its magnitude is represented by the color distribution.

patterns which are not considered here [63]. Additionally, the influence of the gold nanoparticle on the laser beam is not taken into account.

3 Thermal properties of polymers

Synthetic polymers are highly diverse in their physical properties. Thermoplastics are rigid polymers that become reversibly soft above the glass transition temperature [64]. Elastomers are flexible polymers with a glass transition temperature below the operating temperature, often called the rubbery state [65]. Thermosetting polymers are fluid and deformable, but become irreversible rigid after heating [66]. In some cases, polymers show thermoresponsive behavior due to changes in solubility [67] or pre-stressed polymer manufacturing [68].

At the beginning of this chapter we give an overview on the general thermal properties of polymers. Afterwards, we focus on the particular thermal response of polymers, which are employed in this work.

3.1 Thermal response of polymers

Figure 3.1 illustrates idealistic temperature dependent behavior of an model polymer regarding its deformability. All possible states, from the glassy, the rubbery and the fluid states with corresponding glass and melting transitions, are shown in the graph.

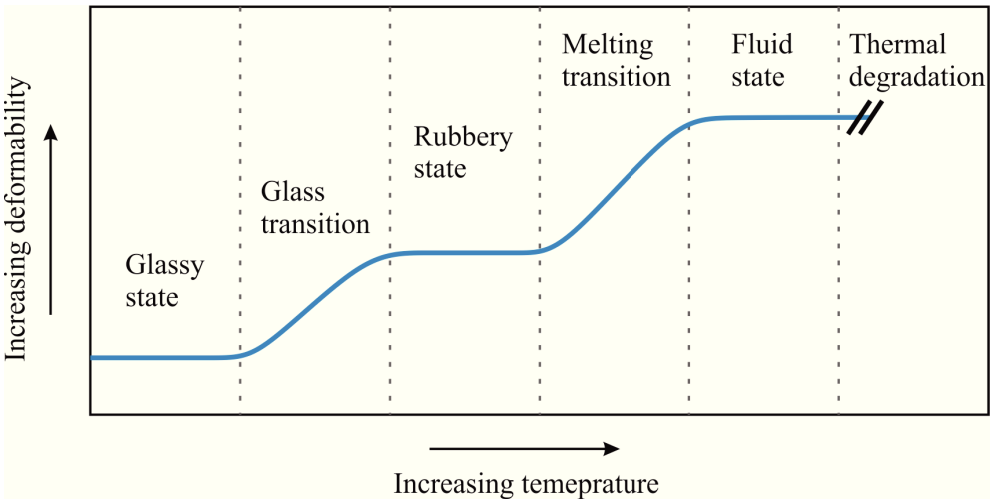

Figure 3.1: **Increasing deformability of a polymer versus the increasing temperature.** By increasing the temperature, the polymer undergoes a glass transition, which leads to a deformable rubbery state. Further increase of the temperature initiates melting of the polymer with the highest deformability. Thermal degradation occurs when the thermal energy is sufficient to break chemical bonds of the polymer chain (adapted from [69]).

The glass transition is a thermal property of amorphous and partially crystalline polymers. It is connected to the thermal energy, which is required to allow long-range segmental motion of the polymer chains [70]. Above the glass transition temperature T_g, it is possible to overcome the interaction between individual polymer chains by applying an external force. The polymer state above T_g is often called the "rubbery state". In this state, polymers become highly flexible and soft. Some factors, such as the polymer chain length [71], shape [72], chain defects, or the heating rate affect a range of the glass transition temperature [73]. Fully crystalline polymers show no glass transition, but have a relatively sharp melting point.

At the melting point of a polymer, the interaction between individual polymer chains is broken by thermal energy [74]. Above the melting point T_m, the polymer behaves as a viscous liquid. Again, factors, such as polymer chain length, the degree of crystallinity, high polarity, and strong binding between individual polymer chains will affect the melting temperature [75]. The exact value of T_m is hard to predict theoretically and is usually experimentally derived. In comparison, fully cross-linked polymers show no melting point. These polymers possess covalent or ionic bonds between polymer chains and start to degrade by high thermal energy before melting.

The stability of most polymers decreases at high temperatures. Increasing thermal energy destabilizes chemical bonds of polymer chains and breaks the long chains to shorter oligomers and monomers [76]. A further increase of the temperature eventually leads to evaporation of polymer components. This process is called thermal degradation [76]. Above the thermal degradation temperature a strong volume and weight decrease of the polymer can be observed.

Polymers also exhibit defined thermoresponsive properties. Usually, these properties are based on a change of the solubility at different temperatures. An important definition in this context is the lower critical solution temperature (LCST), denoting the temperature above which two components are not longer miscible. Polymers with a temperature dependent miscibility allow the solvent to swell the polymer network below the LCST [77]. At the LCST these polymers undergo a phase transition which leads to the release of the solvent from the polymer network [78]. During the phase transition, the polymer changes some of its physical properties drastically. Beside the variable solubility, a pronounced change in the polymer volume, density and refractive index is observed [79]. Additional thermoresponsive character can be provided to polymers by introducing mechanical stress into the polymer in the rubbery state. Cooling down to the glassy state retains the stress inside the polymer. By heating the polymer above the glass transition temperature, the introduced stress can be released and the polymer can change its shape back to the original [80].

In following sections we will briefly explain the relevant thermal properties of the polymers used in this thesis.

3.2 Thermally induced shrinking

Polystyrene (PS) shows a glass transition at temperatures around 100 °C [81], which makes the polymer soft and easily deformable above this temperature. Decreasing the temperature again leads to the rigid glassy state. This behavior makes PS an important polymer for molding processes, where the hot deformable polymer takes the form of the mold and retains it after the cooling [82]. The melting temperature of PS is around 240 °C [74].

Figure 3.2 shows the chemical structure of PS. The polymer is highly transparent for visible light and not soluble with polar solvents like water. Strongly nonpolar solvents as toluene or hexane are able to dissolve the polymer. The surface of structures made of PS is usually hydrophobic and can be modified using oxygen plasma treatment.

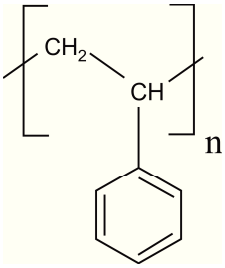

Figure 3.2: **The chemical structure of PS.** PS consists of a long hydrocarbon chain with a phenyl group on every second carbon atom.

A single transparent polymer sheet with a thickness of 1 mm is cut into pieces and used as a substrate for our experiments. At temperatures above the glass transition, the polymer changes its shape irreversibly, such that the surface area of the polymer sheet decreases with the simultaneously increasing thickness. This behavior also leads to a decrease of the distance between structures on top of the polymer surface [80].

The thermoresponsive properties of pre-stressed PS are achieved by the way how the polymer sheet is manufactured. A PS sheet is stretched and heated above the glass transition temperature at the same time. The following rapid cooling of the polymer retains the deformed shape and the applied mechanical stress. At the glassy state, PS is rigid and cannot be deformed by the inner mechanical stress. However, if the pre-stressed polymer is heated above the glass transition temperature, it becomes soft again and returns back to the original

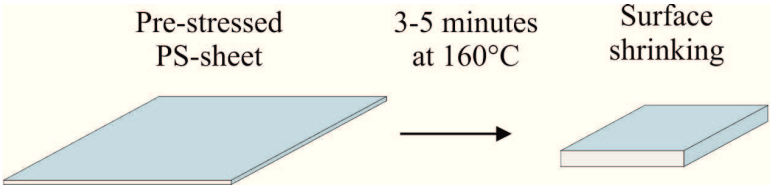

Figure 3.3: **Surface shrinkage of the pre-stressed PS sheet.** The surface area decreases at temperatures above the glass transition of PS. Simultaneously, the thickness of the PS sheet increases.

unstressed shape. This process is irreversible and requires reapplication of heat and mechanical force in order to change the shape of the polymer again.

3.3 Volume phase transitions

Poly(N-isopropylacrylamide) or pNIPAM is a widely studied polymer with defined thermal properties. At room temperature pNIPAM is hydrophilic and, together with water molecules, builds a swollen three dimensional structure, when pNIPAM chains are cross-linked. At temperatures around the lower critical solution temperature (LCST), which is 32-34 °C [83], cross-linked pNIPAM shows a sharp volume phase transition, which is the result of the solubility change of pNIPAM network in water. Below the LCST, the polymer network is hydrophilic and hydrated by water molecules. Above the LCST, the polymer becomes insoluble in water or hydrophobic. Under hydrophobic conditions, the previously water swollen polymer network collapses and expels water molecules. Thereby the volume of the collapsed pNIPAM based structure decreases by several times compared to the swollen state.

Due to the hydrated state of the cross-linked pNIPAM network, it is often called a hydrogel. Micro and nanoscopic structures are named microgels and nanogels respectively. The three dimensional microgel network is typically cross-linked, with pNIPAM serving as a long backbone and N,N'-methylenebisacrylamide a commonly used cross-linker [84]. Usually microgels are produced as a colloidal dispersion in water. Techniques, such as dynamic light scattering can be eas-

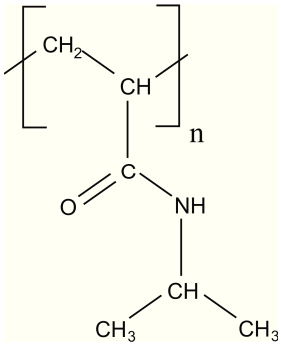

Figure 3.4: **The chemical structure of pNIPAM.** pNIPAM contains a long hydrocarbon chain with an acrylamid group modified with an isopropyl side group.

ily applied to measure the size and the swelling behavior of colloidal pNIPAM microgels [85].

During the collapse process, the volume of the pNIPAM microgel drastically decreases, which leads to the change of the effective refractive index of the microgel particle. At the swollen state, the refractive index of the microgel corresponds to the refractive index of water, which forms more than 90% of the microgel volume [86]. At the collapsed state, water is partially repelled from the polymer network, leading to the increase of the refractive index of the microgel. Figure 3.5 shows the behavior of pNIPAM microgels in water at two different temperature regimes: the swollen microgel at room temperature and the collapsed one above the lower critical solution temperature.

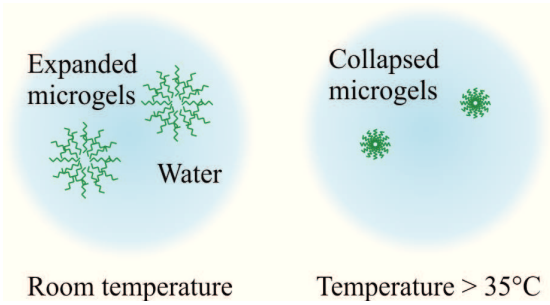

Figure 3.5: **pNIPAM microgel in water at different temperatures.** Left panel: the microgel particle is swollen by water at temperatures below the LCST, containing more than 90% of water [86]. Right panel: above the LCST the polymer network becomes hydrophobic, which leads to water expulsion and collapse of the structure.

The phase transition of pNIPAM is fully reversible [87]. By decreasing the temperature below the LCST, the water solubility of pNIPAM increases again and water molecules hydrate the polymer. Here, the cross-linked pNIPAM undergoes a reversed volume phase transition and swells to the original size.

The kinetics of the volume change depends on pNIPAM structure size to the power of two [88], which leads to a very fast temperature response of micro- and nanogels down to the hundred nanosecond regime [89].

3.4 Thermal degradation

Thermal degradation process of polymers starts when the thermal energy is sufficient to break chemical bonds between polymer chain components. In this work, two polymers are heated to temperatures above the thermal degradation temperature, polyvinyl alcohol and polystyrene.

Polyvinyl alcohol at high temperatures

Polyvinyl alcohol or PVA is a synthetic water soluble polymer (figure 3.6). Films made of PVA are transparent in the visible spectrum of light. Due to its high water solubility and affinity, PVA changes its physical properties, such as deformability or electric conductivity, at high humidity or with water contact [90, 91]. Therefore, PVA is often employed as a base for humidity sensors in some applications [92].

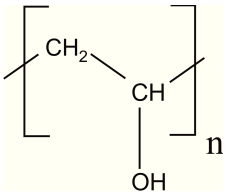

Figure 3.6: **The chemical structure of polyvinyl alcohol.** PVA consists of a hydrocarbon chain with an alcohol group bond to every second carbon atom.

PVA shows a glass transition around 80°C [93] and a melting point around 230°C [94]. In air, the thermal degradation of the polymer starts at temperatures above 300°C [95]. The degradation process can be observed by thermal gravimetric analysis (TGA), measuring the mass loss of the polymer as a function of the temperature. Additionally, the intensity of O–H and C–H stretching modes, measured by Fourier transform infrared spectroscopy, drastically decreases [96]. This decrease corresponds to the breaking of chemical bonds and the sequential shortening of the polymer chains.

The first weight loss of 4.2% is connected to water losses from the polymer matrix at temperatures around 82°C. PVA always shows a small content of water due to its high water affinity. In air, the process of thermal degradation of PVA shows two main steps: at 378°C and 449°C with a corresponding mass losses of 52.4 and 41.7%, respectively. The remaining weight of the carbon residue after water loss and both thermal degradation steps is 1.7%. These temperatures are measured for a specific PVA molecular mass of 24000 g/mol and a certain heating rate of 1 °C/min [96]. Small variations of the thermal degradation temperature are expected for other values for the molar mass and heating rate.

Thermal degradation of polystyrene

PS has a glass transition temperature around 100°C and shows a melting point around 240°C. Thermal degradation of PS starts at around 320°C with a maximum at 390-400°C, which leads to the total weight loss of 99% and a remaining 1% of carbon residue at temperatures above 430°C [97].

3.5 Heat induced cross-linking

Polydimethysiloxane or PDMS is a synthetic silicone-based elastomer. The polymer is transparent in the visible range of light. PDMS is widely used in the area of soft lithography [98]. The polymer is often employed as a material for microfluidic cells [99] and can show both hydrophilic and hydrophobic properties, which can be controlled by the surface treatment [100]. The advantage of PDMS is its thermally triggered cross-linking reaction. Therefore, it belongs to thermosetting polymers.

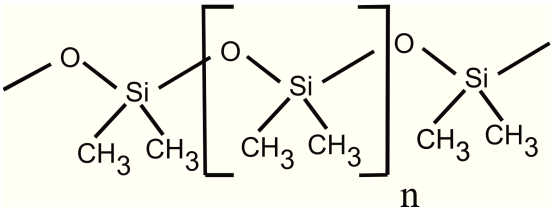

Figure 3.7: **The chemical structure of polydimethylsiloxane.** PDMS consists of an alternating chain of oxygen and silicon atoms. Two methyl croups are bond to each silicon atom.

In our experiments, we use a commercially available PDMS precursor with the trade name Sylgard 184. The polymer has two components with different chain

lengths. The components are mixed and react together (figure 3.8). The cross-linking reaction at room temperature is very slow and takes approximately two days. At higher temperatures the cross-linking reaction can be significantly accelerated, reducing the curing time from days to a few minutes. The cross-linking kinetics is not yet studied. The temperatures and times provided by the manufacturer represent rough values for bulk structures: 48 h at room temperature, 45 min at 100°C, 20 min at 125°C and 10 min at 150°C [101].

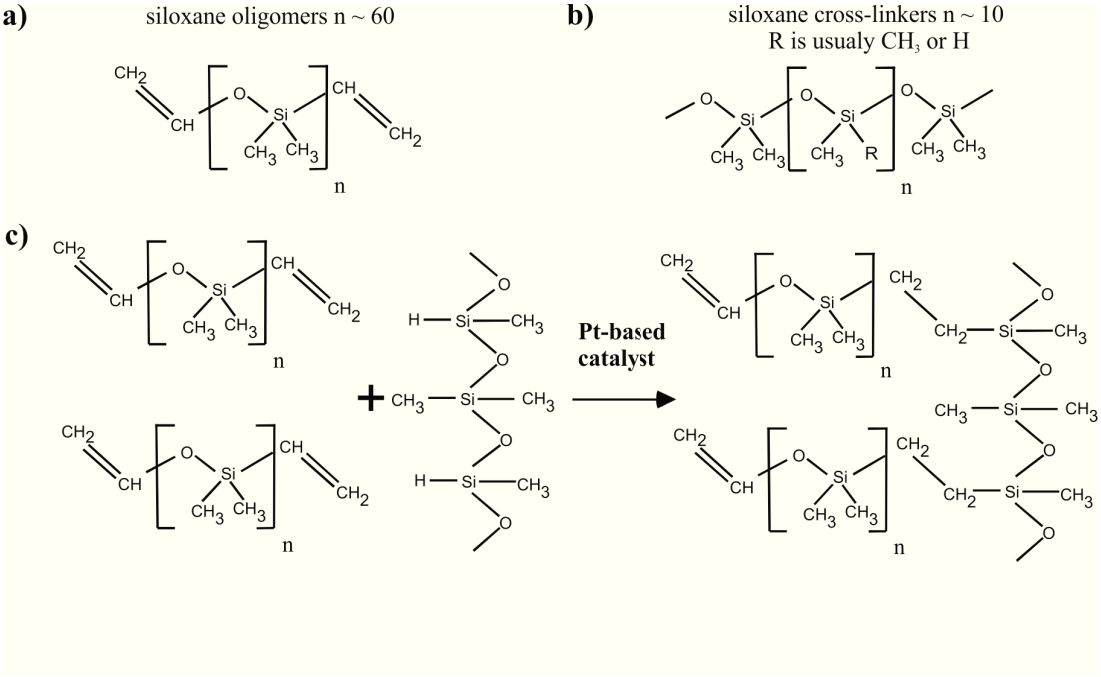

Figure 3.8: **Two compounds of the PDMS precursor and its cross-linking reaction.** a) Siloxane oligomers of around 60 bases build the backbone of the polymer. b) Short siloxane molecules of about 10 bases are used to cross-link long siloxane oligomers. c) Schematic view of the platinum catalyzed reaction between both components of PDMS. (Adapted from [102])

The platinum catalyzed cross-linking reaction is shown schematically in figure 3.8c. Platinum acts as a catalyst during the hydrolization reaction, which binds the short cross-linker molecules to the long siloxane oligomers. After the thermally activated cross-linking reaction, PDMS builds an elastic three dimensional network. Usually, the untreated PDMS network is hydrophobic and insoluble

both in water and in nonpolar solvents, such as hexane. PDMS has no sharp melting temperature and degrades at temperatures around 500°C [103].

4 Characterization of polymer-nanoparticle composites

The following chapter describes methods and techniques used to characterize and manipulate polymer samples. The chapter starts with an introduction of the sample characterization methods, such as dark field microscopy and spectroscopy. Afterwards, non-optical characterization by atomic force and scanning electron microscopy is briefly introduced. These techniques allow the investigation of the sample with nanoscopic resolution. Additional techniques, such as dynamic light scattering and absorbance measurements, are applied to characterize the samples.

4.1 Dark field microscopy

The dark field microscope (DFM) is a powerful tool for gold nanoparticle characterization [104]. Due to the localized plasmon resonance in the visible region of the light spectrum, it is possible to observe spherical gold nanoparticles with an optical microscope by separating the scattered and illumination light as shown in figure 4.1a. The visible color of plasmonic structures observed in a DFM corresponds to the wavelength of the resonance peak position. For example, spherical gold nanoparticles with 80 nm diameter show a plasmon resonance peak between 540 nm to 580 nm in different media. This wavelength is visible as a green color of the scattering structure, as illustrated in figure 4.1b.

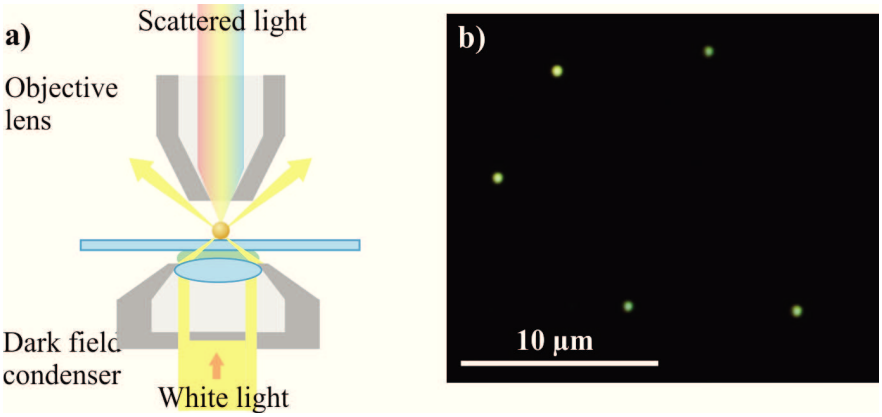

Figure 4.1: **Schematic view of the DFM and observed gold nanoparticles.** a) Schematic view of the DFM. The white light is focused by a condenser in the way, that it does not reach the objective aperture. Only the scattered light of the sample is collected by the objective. b) Several 80 nm gold nanoparticles on a glass substrate observed with the DFM. The non-scattering background is black, which is the origin of the "dark field" denotation.

The basic principle of a DFM is the hollow cone shape of the illuminating light beam, which is focused in the sample plane. The dark region in the middle of the light cone and the high incident angle avoids direct light propagation into the objective. This condition is usually achieved by a condenser system of lenses and spherical mirrors with a mechanically blocked middle part of the illuminating beam. Successful dark field observation depends on the coaxial conformation

of the condenser and the light collecting objective and the ratio between their numerical apertures (NA):

$$\mathrm{NA} = n \sin(\alpha). \tag{4.1}$$

This equation contains n, the refractive index of the immersion medium and α, the half angle of the focused cone of light. If the NA of the objective is higher than the NA of the condenser, the illuminating light will be collected by the objective and disturbs the observation.

Samples can only be observed in a DFM if they scatter light or if they possess luminescent properties. In order to increase the contrast between the observed structure and the background, the substrate is thoroughly cleaned from unwanted scatterers. Additionally, the spectrally resolved scattering properties of the sample can be investigated if the scattered light is collected by a spectrometer.

The DFM used in this work is based on a conventional upright microscope Axiovert 100 by Zeiss GmbH. The light source, a 100 W halogen lamp, covers the whole visible spectrum of light. The dark field configuration is provided by a set of two condensers. An oil dark field condenser "Zeiss 445323" with an NA between 1.2 and 1.4 (corresponding to inner and outer cones of light) allow observations and manipulations with high NA objectives. A special immersion oil with a refractive index of 1.518 is used between the condenser and a glass cover slide. An air dark field condenser "Zeiss 465505" with a lower NA is used to avoid oil contact with the sample and to keep it clean for further measurements. The air condenser has an NA between 0.8 and 0.95, which limits the number of objectives suitable for this condenser to air objectives only.

The light, scattered by the sample, is observed either directly by eye or detected with a digital camera or spectrometer. A Canon 500D digital camera connected to one of the output ports is used for imaging. A grating spectrometer (Acton SpectraPro 300i by Princeton Instruments), which is connected to a liquid nitrogen cooled CCD (Spec-10 by Princeton Instruments), is used for spectroscopy. To allow sub micrometer precise positioning of the sample inside the microscope, the sample holder is modified with a XYZ-stage.

4.2 Scanning electron and atomic force microscopy

Non-optical techniques are applied in order to investigate sample features with dimensions below the diffraction-limited resolution of the optical microscopy.

4.2.1 Scanning electron microscopy

The scanning electron microscopy (SEM) is based on the interaction of a focused electron beam with the sample surface. A beam of electrons focused with magnetic lenses to a tiny spot, provide a much higher resolution compared to optical microscopes that operates with visible light. The electron wavelength is described by the de Broglie relation and depends on the applied acceleration voltage U with $\lambda_e = h/\sqrt{2eUm_e}$. Here, h is the Plank constant, and e and m_e are the electron charge and mass. This wavelength is on order of several tens of picometers for accelerating voltages between 0.2 and 5 kV. Figure 4.2a illustrates schematically the path of the electron beam inside an SEM.

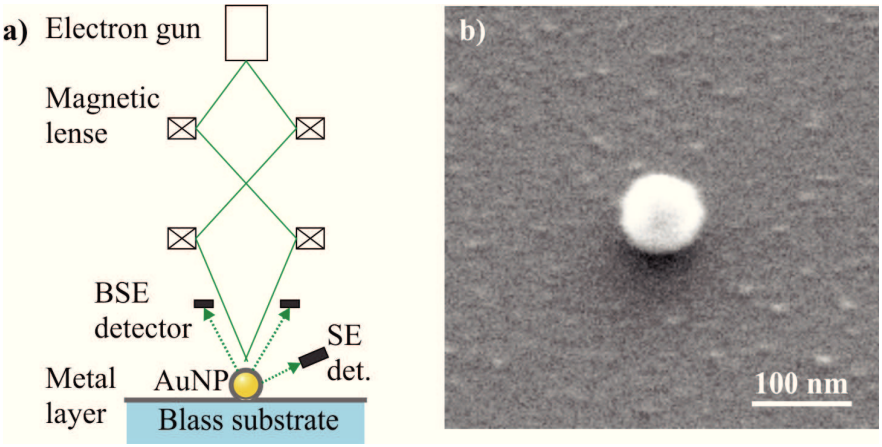

Figure 4.2: **The scanning electron microscope.** a) Schematic view of the SEM. The electrons are accelerated and focused on the sample (green line). The scattered electrons (green dashed arrows) are collected by different detectors. A conductive metal layer is applied on a sample and prevents charging. b) SEM micrograph of a single gold nanoparticle with 82 nm diameter visualized with an SE detector. The sample plane is tilted by 45 degrees.

So called primary electrons of the electron beam are scattered by the sample both in inelastic and elastic ways. Inelastically scattered electrons are called secondary electrons (SE). These electrons are usually low energetic (10-50 eV), thus only few nanometers of the sample surface contribute to the signal. SE from deeper layers cannot escape the sample and be detected. Several factors, such as local surface curvature of the sample, atomic number of the scattering material, electron beam energy and its angle to the sample surface, affect the SE signal. Elastically scattered electrons are so called back scattered electrons (BSE). Their energy is much higher than the energy of SE, therefore it is possible to collect signal from deeper layers of the sample surface. The BSE signal strongly depends on factors, such as atomic number of the sample material and the angle between the irradiated surface and the electron beam. All images in this thesis are made with Zeiss Ultra 55 SEM.

Non-conductive samples are usually coated with a thin layer of metal or carbon to discharge the surface from incident electrons. In this work, a thin conductive layer is made with a Sputter Coater EM SCD005 by Leica, which provides carbon or metallic gold-palladium layers.

4.2.2 Atomic force microscopy

Atomic force microscopy (AFM) is a powerful technique to investigate the surface morphology the sample. The working principle of an AFM is based on the sequential sample scanning by using a sharp tip and measuring the interaction between the tip and the sample surface [105]. In order to detect the signal, a laser beam is pointed on a reflective upper side of the cantilever. Its refection falls on a 4-segment photodiode, which allows very exact measurement of the cantilever deflection caused by the sample surface. Both, the horizontal and vertical position of the cantilever are controlled by very precise piezos. A schematic of the working principle of an AFM and an image of an 80 nm gold nanoparticle on a glass surface are shown in figure 4.3.

The spatial resolution of an AFM depends on the tip curvature [106]. In this work, tips with a radius below 7 nm (NANOSENSORS by NanoWorld AG) are

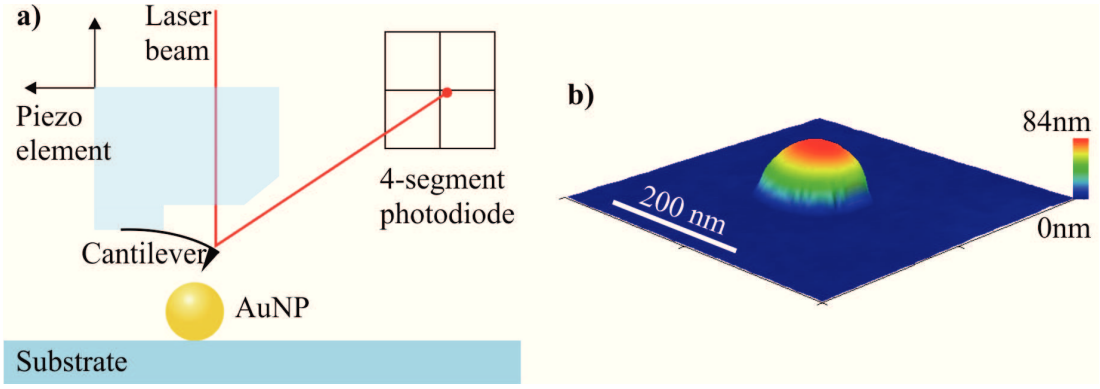

Figure 4.3: **The atomic force microscope.** a) A schematic view of an AFM. A cantilever with a sharp tip interacts with a sample surface which leads to bending of the cantilever. The position of the reflected laser beam is detected with a photodiode. b) An AFM scan of a gold nanoparticle with a diameter of approximately 80 nm.

used for measurements. These tips are coated with a 30 nm thick aluminum, have a force constant of 42 N/m and a resonance frequency of 330 kHz.

Three operation modes are mostly relevant for measurements with an AFM: the contact mode (static mode), the non-contact mode [107] and the tapping mode [108] (dynamic modes). In the contact mode the scanning tip is contacting the sample surface physically. The signal is provided by cantilever deflections due to the sample roughness. This mode is usually applied in combination with rigid samples and can destruct fragile samples [108]. Dynamic modes use excited cantilevers [109] and are based on forces, such as van der Vaals and Coulomb interactions, which occur between the sample surface and the tip at small distances. In the non-contact the cantilever is oscillating with a few nanometer amplitude less than 10 nm to the sample surface. In the tapping mode, the cantilever is oscillating at higher distances and amplitudes both in the range of 100-200 nm. The oscillation frequency of the cantilever in the non-contact and tapping modes is affected by the interaction with the sample surface. Therefore, the read out is based on the changing oscillation frequency of the cantilever. Non-contact and tapping modes can be applied with soft samples, such as lipid layers [110].

All measurements in this work are performed with a NanoWizzard AFM by JPK Instruments AG.

4.3 Dynamic light scattering

In our experiments, we apply the technique of dynamic light scattering (DLS) in order to measure the mean hydrodynamic radius of pNIPAM microgels inside the colloidal suspension.

The method is based on light scattering by small diffusing particles. The fluctuation of the scattered light due to the Brownian motion of particles allows to calculate their mean velocity and the diffusion coefficient D. The radius of the particle is connected to D via the Stokes-Einstein equation [111].

Here, all DLS experiments are performed with a Zetasizer Nano S by Malvern Instruments GmbH, which uses a 4 mW He-NE laser with a wavelength of 633 nm.

4.4 Laser heating and spectroscopy setup

A new setup was built to perform heating experiments and measure the change of optical properties of the pNIPAM coated gold nanorods simultaneously. The setup combines both a continuous wave laser (with a wavelength of 800 nm to heat the gold nanorods) and a probing white light beam for absorbance measurements (figure 4.4). The heating process is triggered by a continuous wave 800 nm Ti:Sapphire laser (Coherent, Inc.) focused by a lens inside a sample filled-cuvette. A tungsten halogen lamp HL-2000 (Ocean Optics, Inc.) acts as a white light source. The maximum overlap of both beams, which is significant for the successful measurement, is realized by an exact positioning of the beam splitter. After the cuvette with pNIPAM-nanorod suspension both beams are parallelized by a second lens.

To obtain the exact extinction spectrum of the nanocomposite, we perform baseline experiments with a water-filled cuvette. The difference between the empty sample and the pNIPAM-nanorod suspension provides the pure absorbance of the sample. In all experiments, the spectral region around the laser wavelength is blocked by the notch filter (NF03-808E-25 by Semrock, Inc.) to avoid direct laser propagation into the spectrometer. The blocked region also contains no relevant signal, and is therefore removed from all spectra. The remaining signal is interpolated with a polynomial function.

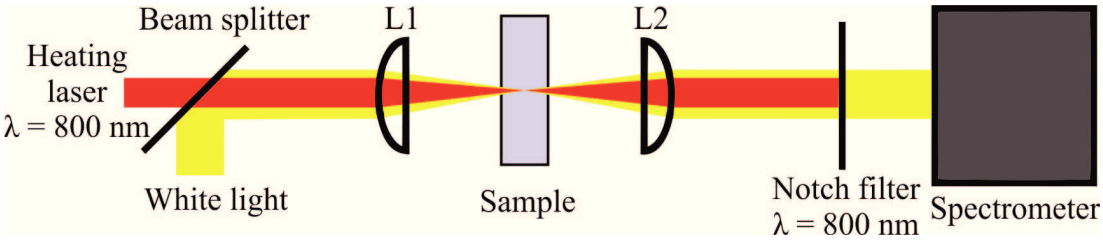

Figure 4.4: **Schematic view of the pNIPAM-nanorods heating setup.** The setup is used for simultaneous laser irradiation and optical extinction measurement of pNIPAM-nanorod nanocomposites. A semitransparent beam splitter overlaps the white light and the heating laser. The beam is focused by a lens L1 inside a cuvette containing the sample. The second lens L2 collimates the beam and the notch filter blocks the laser. The remaining white light is collected by a spectrometer.

5 Plasmonic sensing and manipulation of thermoresponsive polymers

In the following chapter we investigate possibilities for applying gold nanostructures to sense nanoscopic polymer changes. Properties, such as plasmon coupling or plasmon shifts due to refractive index changes, allow to monitor the distance between gold nanostructures or changes in their surrounding respectively. In the first part of this chapter, surface changes of a thermoresponsive polymer are investigated by using gold nanoparticles as nanoscopic markers on top of a transparent polymer sheet. The defined shrinking behavior of the polymer leads to plasmon coupling of previously laser-printed gold nanoparticles. The second part of the chapter deals with the application of a gold nanorod as a sensor and trigger volume phase transitions of a thermoresponsive polymer.

5.1 Plasmon coupling of gold nanoparticles by substrate shrinking

The plasmonic property of two or more gold nanoparticles changes drastically for very short separation distances [112]. To understand this process, we consider the electric field outside the gold nanoparticle, which can be calculated from the electric potential (equation 2.9). This potential has an anisotropic distribution and leads to maximal values of the outer electric field in a direction parallel to the polarization of the exciting electric field. The effect is called local field enhancement. If local electric fields of two nanoparticles affect their localized plasmon oscillations, the resonance of both nanoparticles shifts to a lower energetic region [113]. Coupled nanostructures are a big interest for different applications, such as biosensors [114], florescence [115] and Raman signal enhancers [116]

The method of laser printing is a straightforward technique to produce arbitrary structures of individual metallic nanoparticles on a planar surface [33]. This method uses a strongly focused laser beam to deposit colloidal gold nanoparticles on the surface of a substrate in controlled geometries. Unfortunately, due to plasmonic heating and light scattering around a printed gold nanoparticle, placing a second nanoparticle close enough to couple both of them plasmonically has been a challenge. The closest distance between two gold particles achieved by this method is around 200 nm. At this distance no plasmon coupling of printed gold nanoparticles is observed and the distance between laser printed gold nanoparticles must therefore be significantly reduced.

A substrate made of thermoresponsive pre-stressed PS leads to decrease of its surface's structures by decreasing the surface area after the shrinking process at moderate temperatures [68, 80]. Pre-stressed PS retains its original shape after heating it above its glass transition temperature of around 80°C. The material is manufactured as a stretched planar sheet to achieve shrinking in two dimensions (length and width) and an increase in one dimension (thickness).

Measuring the shrinking factor of pre-stressed PS

Gold nanoparticles are printed on a glass substrate using optical force printing [33]. Colloidal spherical gold nanoparticles with a diameter of 82 nm are printed by applying a focused laser beam with a wavelength of 532 nm. Multiple beam arrays can be used to parallelize the printing process and to print nanoparticles in an arbitrary pattern within seconds [32]. Splitting the singe beam into multiple beams is achieved by a spatial light modulator (SLM) based on a liquid crystal matrix.

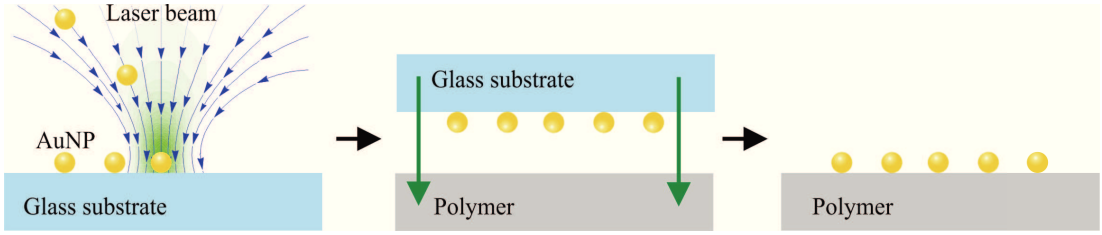

Figure 5.1: **Pattern of gold nanoparticles on a pre-stressed PS.** Left panel: gold nanoparticles are printed from a colloidal suspension on a glass substrate. Middle panel: transfer process by pressing the polymer and the glass substrates against each other. Right panel: the resulting pattern on a pre-stressed PS substrate.

First, gold nanoparticles are printed on a glass cover slip. The resulting structure is then transferred from the glass substrate to a polymer substrate by using a mechanical press with a force of 14 kN applied for 7 min (figure 5.1). Simultaneously, both substrates are heated to soften the polymer and improve the transfer efficiency. The comparison of the pattern before and after the transfer process shows over 99% of successfully transferred gold nanoparticles (figure 5.2).

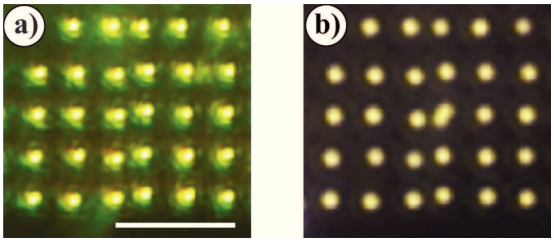

Figure 5.2: **Laser stamped and transferred gold nanoparticle pattern in a DFM.** Gold nanoparticles with a diameter of 82 nm are printed on a glass substrate (a) and transferred to a pre-stressed PS (b). The number and position of most gold nanoparticle patterns remain after the transfer step. The scale bar is 10 µm. (Adapted from [117])

The importance of the transfer step is explained as follows: direct laser printing of gold nanoparticles on the polymer substrate is only possible at higher laser intensities due to the strong repulsive interaction between the polymer surface and gold nanoparticles. Laser printing on a glass surface can be achieved with a laser power around 300 µW, while laser powers above 900 µW are necessary to print the same gold nanoparticles on the polymer surface. Increasing the laser intensity simultaneously leads to higher temperatures of the gold nanoparticle surface. Thus, the polymer surface is modified by hot nanoparticles during the laser printing process, as shown in figure 5.3b. The simulation of the heat distribution around the gold nanoparticle is shown in figure 5.3c and provides temperatures above the glass transition of PS (red dashed line). At these temperatures the polymer matrix becomes soft and allows the gold nanoparticle to be pressed into the polymer by optical forces. Additionally, the mechanical stress inside the polymer is locally released, leading to the deformation of the polymer around the printed nanoparticle. To avoid modifications of the polymer surface during the laser printing, gold nanoparticles are first printed on a glass substrate and then transferred to the polymer.

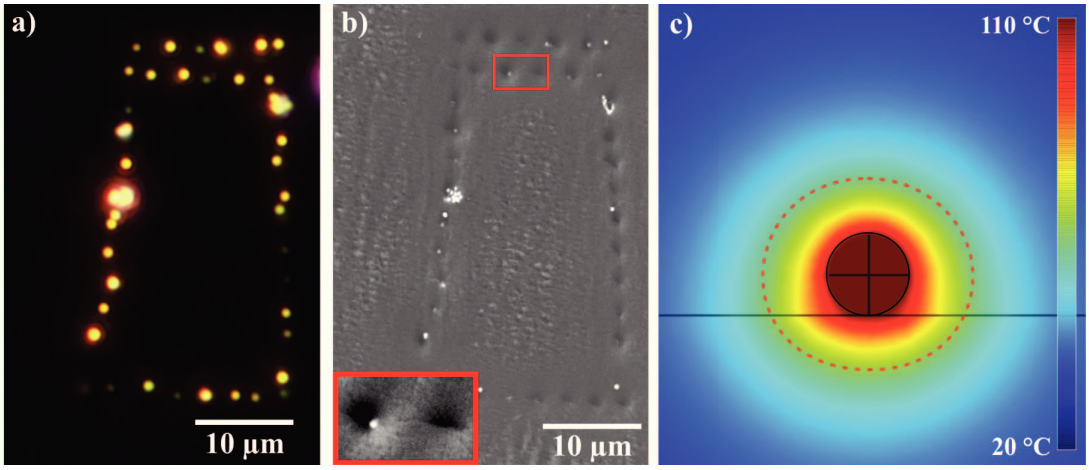

Figure 5.3: **Laser printing of gold nanoparticles on a polymer substrate.** A pattern of laser printed gold nanoparticles on the PS surface observed by DFM (a) and SEM (b). The polymer surface is modified due to their high surface temperature as shown in the red inset. c) The simulated heat distribution around the gold nanoparticle. The red dashed line denotes the temperature region above the glass transition temperature of PS. (Adapted from [117])

In order to determine the shrinking factor, by which the length and the width of the substrate surface are decreased, an array of over 640 gold nanoparticles is printed on a glass substrate and transferred to a pre-stressed PS substrate. Interparticle distances before and after shrinking are measured by analyzing the gold nanoparticle array with a SEM. The measurement shows that separation distance decreased by a factor of 2.34. Figure 5.4 shows the measured distribution of the interparticle distance for the whole laser stamped array of 640 nanoparticles. The narrow distribution of the shrinking factor is connected to nearly uniformly shrinking of the polymer even at the sub-micron level.

In terms of measuring surface changes on such a small level, arrays of gold nanoparticles exhibit a big potential. Measured with a DFM, it is possible to calculate the position of the gold nanoparticle with a precision below 25 nm just by approximating its image with a 2D-Gaussian. SEM measurements allow the gold nanoparticles to be localized with much higher precision, which is significantly below 5 nm. Therefore, this method allows to monitor changes of the polymer with a high precision by measuring nanoparticle positions before and after the shrinking.

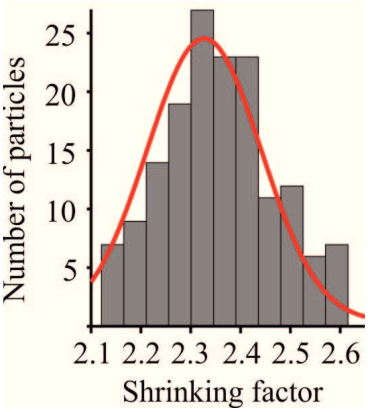

Figure 5.4: **Measuring the shrinking factor of pre-stressed PS.** The histogram shows the number of gold nanoparticles versus the factor, by which the distance between these nanoparticles is reduced after the substrate shrinking process. Fitting the histogram with a Gaussian function reveals the mean shrinking factor of 2.34. (Adapted from [117])

Plasmon coupling after substrate surface decrease

The interparticle distance provided by the laser stamping method is bigger compared to single particle laser printing. The reason is the better focusing quality of a single laser beam, which cannot be reached by using an SLM due to higher optical aberrations. For the following experiments, gold nanoparticles were therefore

only printed with a single beam. Dimers, trimers and tetramers are produced on a glass substrate in order to transfer them to pre-stressed PS and achieve plasmon coupling by substrate shrinking. The exact distance between single gold nanoparticles is measured by SEM. Before substrate heating, the particles were printed at a distance around 280 nm (center to center), which is again too far to observe a notable plasmon shift. One of the produced trimers is shown exemplary in figure 5.5a. The single gold nanoparticles can still be distinguished by DFM. Also, the scattering spectrum of the produced trimer corresponds to the spectrum of uncoupled gold nanoparticles with 82 nm diameter.

The PS substrate is placed into an oven for three minutes to induce the shrinking process. The oven temperature is 165°C, which is above the glass transition temperature but below the melting temperature of PS. The result is shown in figure 5.5b. During the shrinkage of the PS sheet, the distance between the gold nanoparticles follows the decrease of the substrate surface. Hence, single gold nanoparticles of printed structures are not separately distinguishable with an optical microscope anymore. Additionally, the light scattered by the structures shifts from green to orange, which indicates plasmonic coupling between the nanoparticles. The distance between the particles was now around 120 nm (center-to-center) or 20 to 40 nm (surface-to-surface), which is sufficient for plasmonic coupling. The scattering spectra of coupled structures cannot be approximated with a single Gaussian function, but by using a fit of two functions as shown in figure 5.5c. That drastic change of the scattering spectrum results from the plasmon coupling between gold nanoparticles inside the trimer.

The theoretically predicted plasmon resonance of a single 82 nm gold nanoparticle surrounded by water is around 550 nm. Before the substrate heating, the scattering peak of the laser printed nanoparticles is around this value. After substrate heating and shrinking, a second red shifted peak in the scattering spectrum appears. The position of this peak depends on the exact distance between plasmonically coupled gold nanoparticles. In the case of two nanoparticles with a surface-to-surface distance of 20 nm, the scattering peak red shifts to 585 nm. A similar red shift is observed in our experiment: the peak of the second Gaussian function approximating the scattering spectrum lies around 590 nm. The simultaneous appearance of two peaks in the same spectrum is explained by the

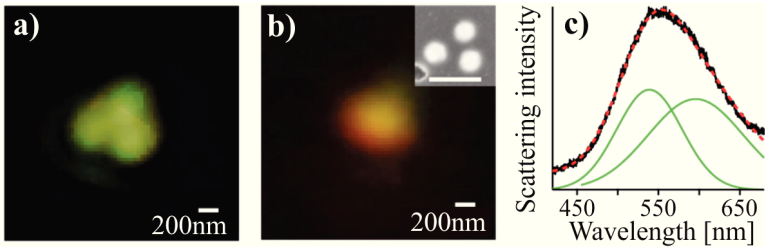

Figure 5.5: **Plasmonic coupling of a trimer after substrate shrinking.** DFM images of a trimer structure, printed using 82 nm gold nanoparticles, before (a) and after (b) the substrate heating. SEM image of the trimer after shrinking is shown in the top right corner of panel (b). The black curve in (c) shows the scattering spectrum of the trimer after shrinking. The red dashed line shows an approximation consisting of two Gaussian functions (green lines). (Adapted from [117])

nonlinear polarization of the illuminating light: both plasmonically coupled and uncoupled modes of the printed structure are excited at the same time.

For realistic sensing applications with plasmonically coupled gold nanoparticles, the resulting surface-to-surface distance must be reduced. The first possibility is to reduce the interparticle during the laser printing process. The second possibility is to choose another shrinking material with a higher shrinking factor. Both of these possibilities are discussed in the following section.

Reducing the interparticle distance

A closer look at the complex polarizability function and cross sections of the gold nanoparticle provides important information about the printing process. All of these factors affect the precision and the resulting interparticle distance. The complex polarizability is connected to optical forces acting on a gold nanoparticle during the laser printing process, with the absorption and scattering cross sections determining the surface temperature and the amount of scattered light, respectively. Theoretical calculations predict a considerable change of all important factors by applying other wavelengths during the laser printing process.

Laser printing of gold nanoparticles is usually done by a laser with a wavelength of 532 nm. In figure 5.6a and b the position of this wavelength is denoted with a vertical green line. At 532 nm the real part of the polarizability shows positive values close to zero. At the same time, the imaginary part of the polarizability is

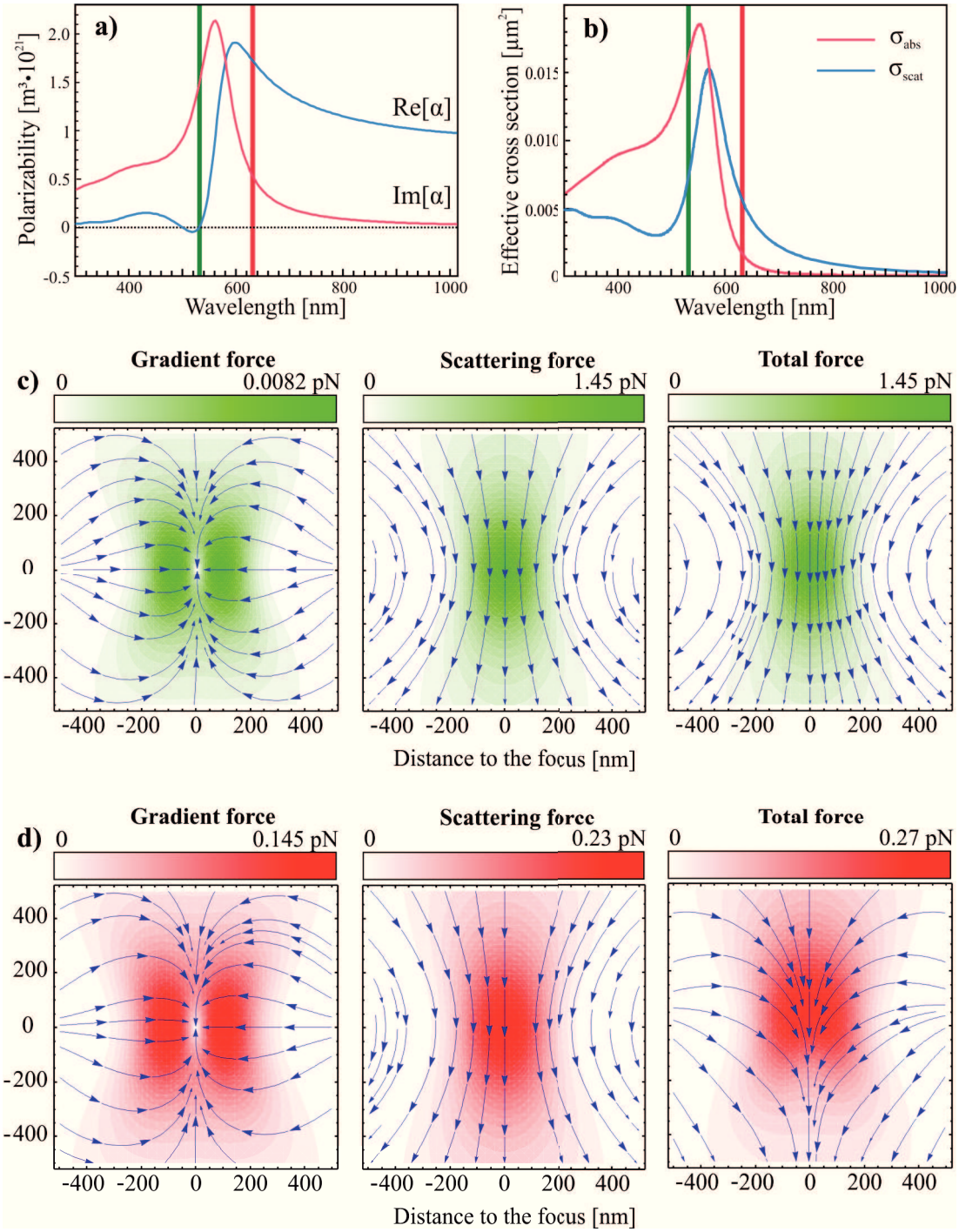

Figure 5.6: **Polarizability, effective cross sections and optical forces at different wavelengths.** a) Complex polarizability of an 82 nm gold nanoparticle in water. b) Effective absorption and scattering cross sections of the same gold nanoparticle. c) Calculated optical forces exerted by a 532 nm laser beam, focused with an 1.0 NA objective. The laser power is 1 mW. d) Calculated optical forces at a 633 nm wavelength. The same laser power and same NA are used.

close to its maximum. Therefore, the gradient force on a gold nanoparticle is very weak and the scattering force is highly dominating. At the focal plane the gold nanoparticle is almost not confined laterally, but experiences a strong scattering force directed along the optical axis. Figure 5.6c illustrates both the low gradient and the dominating scattering forces by a focused laser beam on an 82 nm gold nanoparticle in water. The difference between the gradient and the scattering force is three orders of magnitude. Also, the value of the absorption cross section is close to its maximum, which leads to strong heating of the gold nanoparticle. The high temperature around laser-irradiated gold nanoparticles disturbs the optical trapping process and can lead to thermal escape from the optical trap [118]. In our case, the increased temperature would lead to decreased printing precision of a single nanoparticle and disturb printing of a dimer structure.

In order to increase the lateral confinement of a gold nanoparticle by the gradient force and decrease the heat effects, the laser wavelength has to be redshifted to 633 nm. This wavelength provides a strong scattering force to overcome the repulsive potential of the substrate and print the gold nanoparticle. Additionally, the gradient force is on the same order of magnitude as the scattering force, which results in a strong lateral confinement of the gold nanoparticle in the focal plane. The absorption cross section decreases by one order of magnitude from $1.73{\cdot}10^{-2}$ µm^2 at 532 nm to $1.244{\cdot}10^{-3}$ µm^2 at 633 nm. This leads to a temperature decrease of the printed gold nanoparticle by a factor of ten. The scattering cross section decreases from $8.24{\cdot}10^{-3}$ µm^2 at 532 nm to $4.89{\cdot}10^{-3}$ µm^2 at 633 nm, which decreases the amount of the scattered light by a factor of 1.7. Due to all these effects, applying a laser with a wavelength of 633 nm might improve the laser printing accuracy and decrease the interparticle distance during laser printing.

A similar effect, comparable to applying a red-shifted laser, can be achieved by using gold nanoparticles with smaller sizes, which shifts the plasmon resonance peak to the shorter wavelength region. Another factor is the refractive index of the surrounding fluid (Fröhlich condition, from the Clausius-Mossoti equation). An increase of the refractive index redshifts the plasmon resonance peak, and a decrease leads to a blueshift. By changing the refractive index, a suitable relation

between the plasmon peak position to the applied laser wavelength might be found.

Additional present limitation of the plasmon coupling is the low shrinking factor of pre-stressed PS, which is 2.34 according to our measurement. This factor is provided by the manufacturing process of the acquired PS sheet. Pre-stressed PS with a higher shrinking factor might decrease the interparticle distance. Another materials, such as polyolefins (PO), show a similar temperature-activated shrinking behavior. A the same time, commercially available PO shows a higher shrinking factor (the experimental value is around 4.4 [119]), which would reduce the resulting separation distance of the printed plasmonic structure by a factor of around 1.9 and provide a stronger plasmon coupling.

5.2 Plasmonic sensing and triggering of pNIPAM phase transitions

PNIPAM-based microgels belong to the group of "smart" materials [85, 87]. Their sub-micron size and temperature controlled reversible swelling/collapsing behavior attracts big interest since their fist synthesis in 1986 [120]. Applications, such as tunable microlenses [121, 122], drug delivery [123, 124], thermoresponsive coatings [125, 126] or actuators [127], are based on thermoresponsive properties of pNIPAM. An interesting benefit to these applications is a selective and remotely triggerable swelling/collapsing process. A strongly localized, light controlled heat source, such as a gold nanostructure can be used to trigger this property.

Gold nanorods possess similar optical properties as spherical gold nanoparticles with some important differences. The full rotation symmetry of spherical particles is reduced to only one axis. Two nanorod axes are distinguished: the long axis, along the symmetry axis and a short axis, perpendicular to it. The plasmon resonance of a nanorod depends strongly on the polarization direction of the incident light. The resonance, corresponding to the long nanorod axis (longitudinal resonance), shows a redshifted peak compared to the resonance along the short axis (transversal resonance).

Plasmonic properties of gold nanorods allow efficient heat generation by resonant laser light illumination. Gold nanorods are more sensitive to the refractive index change of the surrounding medium compared to spherical gold nanoparticles [128], which makes them good candidates as nanoscopic sensors [129, 130]. In order to investigate and trigger phase transitions of a known polymer at the nanoscale, a hybrid nanorod-polymer structure is employed.

5.2.1 Plasmon resonance shift by volume phase transitions

Gold nanorods with a length of 61±8 nm and a thickness of 14±2 nm (aspect ratio 4.47±0.65) are coated with a pNIPAM shell using the method of Contrera-Caceres [84]. First, a thin layer of polystyrene–divinylbenzene is polymerized on the gold nanorod surface. Afterwards, a shell of pNIPAM is grown. N,N'-methylenebisacrylamid acts a cross-linker during the shell growth.

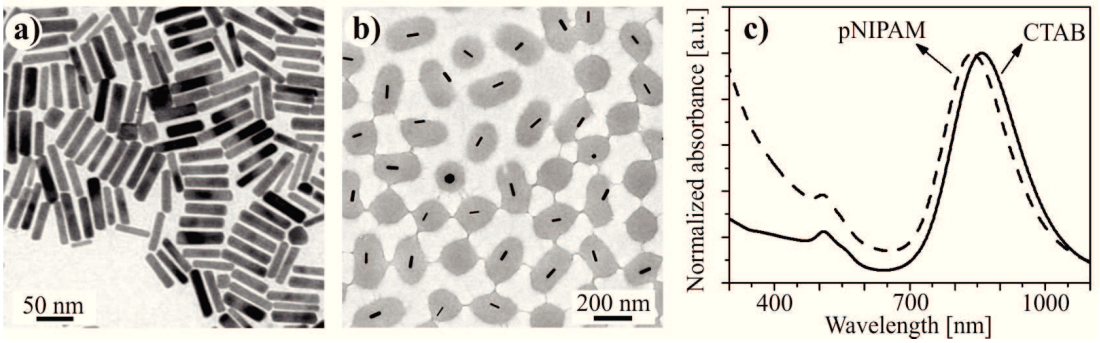

Figure 5.7: **Gold nanorods with a pNIPAM shell.** TEM pictures of gold nanorods before a) and after the polymerization reaction b). The pNIPAM shell coating most nanorods is clearly visible as a gray structure. c) Normalized absorption spectrum of gold nanorods in water. The plasmon peak with a pNIPAM shell is clearly blue shifted due to the thermal reshaping during the polymerization. (Adapted from [131])

Figure 5.7 shows CTAB-stabilized nanorods before (a) and after (b) the pNIPAM polymerization reaction. The plasmon peak of gold nanorods shows a blueshift of 22 nm after the polymerization reaction (figure 5.7c). This spectral shift is provided not only by the change of the refractive index by the surrounding pNIPAM shell, but it is mainly caused due to the thermal reshaping during the polymerization process. The polymerization reaction takes place for several hours at 70 °C. The aspect ratio of the gold nanorods is reduced to 3.99±0.82.

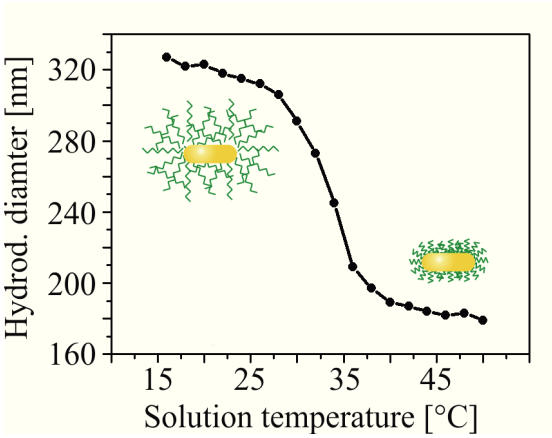

Figure 5.8: **Evolution of the hydrodynamic size of pNIPAM-nanorod nanocomposites as a function of the solution temperature.** During the experiment, the solution temperature is increased stepwise by 2°C. Each measurement is performed after the temperature reaches its equilibrium. The diameter of 320 nm at 16°C is reduced to 180 nm at the highest temperature. (Adapted from [131])

The temperature-dependent size changes were measured by DLS. A clear evidence of the microgel volume phase transition was observed. A cuvette containing a water dispersion of gold nanorods with a pNIPAM shell is heated stepwise until

it reaches values above the phase transition temperature. The mean hydrodynamic diameter of the nanocomposite decreases from around 320 nm at 16°C to 180 nm at 45°C, as shown in figure 5.8. A sharp size decrease is observed at temperatures around 33-34°C, which corresponds to the volume phase transition temperature of pNIPAM. Each DLS measurement is performed after 2°C temperature increase.

Above the LCST, the size of the polymer shell decreases and its increasing refractive index affects the plasmon resonance of the incorporated gold nanorod. In order to determine this effect, a cuvette with a nanorod-pNIPAM dispersion is heated above the LCST while measuring the extinction spectrum in visible and near infrared spectral range. Figure 5.9 illustrates optical properties of the pNIPAM-nanorod suspension depending on the solution temperature, and the corresponding theoretical calculation.

Two main effects are observed during the bulk heating experiment. On one hand, the extinction in the region around 400 nm is strongly increased (short wavelength region in figure 5.9a). This increase is provided by the pNIPAM microgel structure only [89]. The refractive index of pNIPAM in the fully collapsed state arises from an increased contrast to the surrounding aqueous solution, which leads to the increased amount of scattered light. Figure 5.9c illustrates the temperature dependent change of the extinction at 400 nm. On the other hand, a temperature dependent red shift of the longitudinal plasmon resonance is observed (peak shift around 840 nm in figure 5.9a). The plasmon peak at 16°C appears at 828 nm wavelength and shifts during the heating process to 862 nm at 60°C. The resulting redshift is around 34 nm. In order to confirm the measured values of plasmon peak position, we calculate the theoretical extinction of gold nanorods with different refractive indexes of the surrounding medium.

To calculate the wavelength dependent extinction of a nanorod, the polarizability function of a spherical structure (equation 2.21) must be modified for ellipsoidal particles [132]. Here, an ellipsoid can be seen as an approximation for a nanorod shape and provides values comparable to experimental results with nanorods [133]:

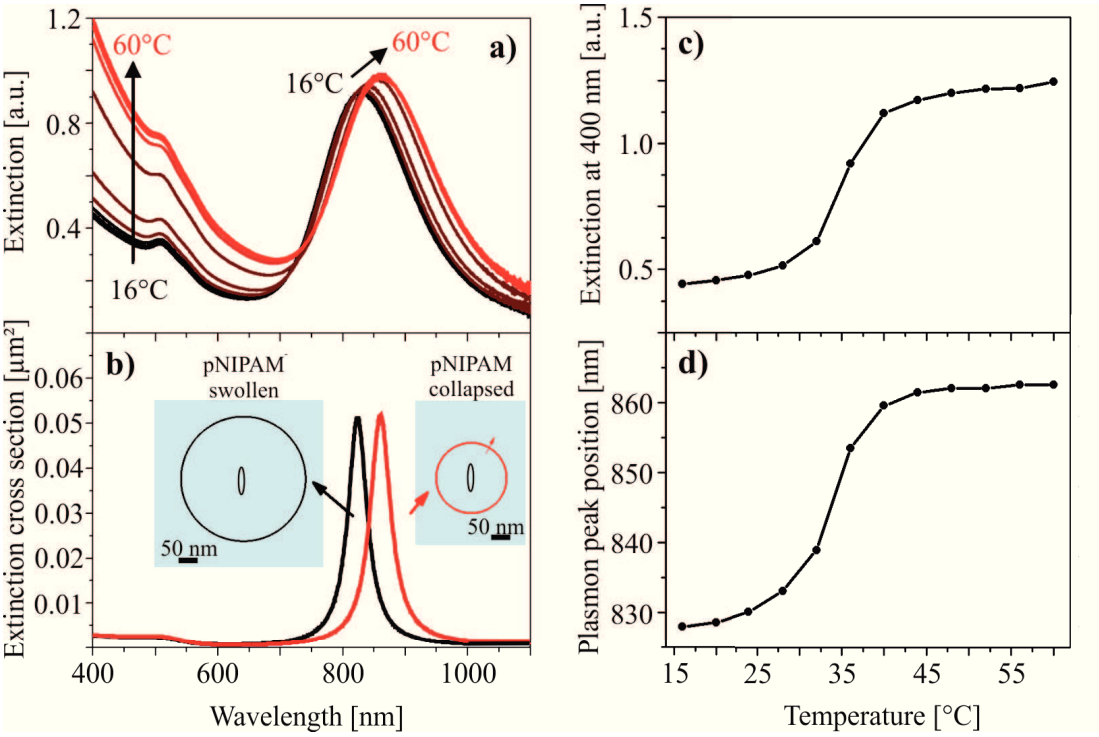

Figure 5.9: **Measured and calculated response of a pNIPAN-nanorod nanocomposite during the temperature increase.** a) Experimental extinction spectrum of the nanocomposite suspension. Two main changes are denoted by black arrows: around 400 nm and around 830 nm. b) Calculated plasmon peak for different refractive indexes. The evolution of the extinction at 400 nm (c) and the longitudinal plasmon peak position (d) at different solution temperatures. (Adapted from [131])

$$\alpha_{x,y,z} = \frac{4\pi abc(\varepsilon - \varepsilon_m)}{3\varepsilon_m + 3L_{x,y,z}(\varepsilon - \varepsilon_m)}, \tag{5.1}$$

with dielectric functions of gold ε and the surrounding material ε_m and ellipsoid dimensions a,b,c along the axes x,y and z. In these equations the long axis of the ellipsoid is a with a relation to other two dimensions of $a > b = c$. The depolarization factor for different axes $L_{x,y,z}$ is given by the following equations:

$$L_x = \frac{1-e^2}{e^2}(-1 + \frac{1}{2e} ln(\frac{1+e}{1-e})) \tag{5.2}$$

and

$$L_{y,z} = (1 - L_x)/2. \tag{5.3}$$

Here $e^2 = 1 - (b/a)^2$ is the ellipticity factor of the prolate ellipsoid.

The plasmonic response of a gold nanorod due to the collapse of the surrounding pNIPAM shell is calculated with the modified polarizability from equation (5.1) and the polarizability-extinction relation $\sigma_{ext} = kIm[\alpha]$. For this calculation, an ellipsoid with a length of 63 nm [2] and a thickness of 14 nm are considered. The refractive index of a swollen pNIPAM shell is 1.335 [134] and the total diameter is 324 nm; the collapsed shell refractive index is 1.414 [134] and the corresponding diameter is 183 nm. Plasmon resonance peaks, predicted by the calculation, are at 824 nm for the fully swollen shell and 860 nm for the collapsed shell (figure 5.9b). The calculated redshift is around 36 nm, which is in a good agreement with the measured value of 34 nm.

Similar to a pure pNIPAM microgel, the pNIPAM-nanorod composite shows a fully reversible swelling/collapsing behavior. After several measurements, the plasmon shift remains around 34 nm, indicating the successful pNIPAM encapsulation of gold nanorods in the suspension. The long term colloidal stability of the nanocomposites is slightly reduced, which is observed as a gradual change of the longitudinal plasmon peak (figure 5.10a). TEM measurements reveal the reason of the reduced stability: partially aggregated nanorods lead to the gradual redshift of the longitudinal plasmon resonance peak after each measurement (figure 5.10b). This reduction in colloidal stability at high temperatures is confirmed by previous investigations [134].

5.2.2 Induced pNIPAM volume phase transition by plasmonic heating

The high refractive index sensitivity of gold nanorods can be applied to monitor the collapse of the surrounding pNIPAM shell above the LCST, as shown in the previous section. Apart from the sensing, gold nanorods can also be used as

[2] This value is slightly above the measured mean length of synthesized nanorods, which is necessary due to the stronger contribution of longer nanorods to the extinction [133].

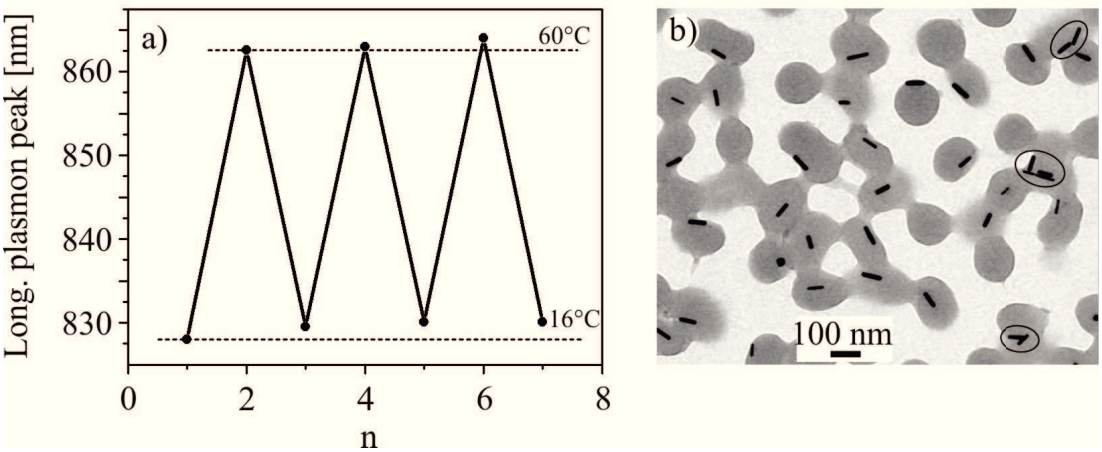

Figure 5.10: **Long term stability of the pNIPAM-nanorod nanocomposite.** a) Evolution of the longitudinal plasmon peak as a function of the number of heating and cooling cycles. A gradual shift of several nanometers occurs after each heating/cooling cycle. b) Partial aggregation of pNIPAM-nanorod nanocomposites is confirmed by TEM (denoted by black ovals). (Adapted from [131])

nanoscopic heat sources. The generated heat is transferred to the surrounding water and pNIPAM network. Reaching temperatures above the LCST leads to the volume phase transition of the polymer.

Theoretical calculations were performed in order to determine the required laser power density during the heating experiment. The absorption cross section of the gold nanorods was calculated using the modified polarizability function (5.1). It is important that the temperature is sufficient to trigger the collapse process of the pNIPAM shell. Simulations show that a laser power density of 880 kW/cm^2 provides temperatures above the LCST in a region closer than 140 nanometers to the nanorod surface (figure 5.11a). This power density is chosen as the upper limit for our experiments. At higher power densities, the generated heat could lead to a thermal reshape of the nanorod. This would cause a non-reversible blueshift of the plasmon resonance peak, which in turn would influence the absorbance measurement.

According to the simulation, the temperature of the gold nanorod surface reached around 90% and 95% of the steady state temperature at 50 and 200 ns, respectively, after switching the laser on (figure 5.11b). The simulation considers the temperature increase of the surrounding medium, which also takes place at

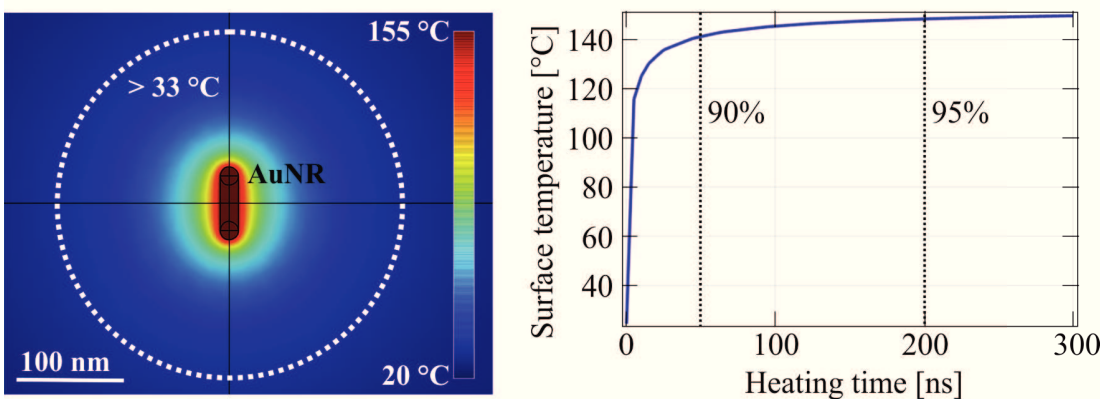

Figure 5.11: **Simulated temperature around the gold nanorod in water** a) The spatial temperature distribution around a 61 nm long and 14 nm thick gold nanorod. The employed laser wavelength is 800 nm and its power density is 880 kW/cm^2. The calculated absorption cross section at 800 nm is $3.7{\cdot}10^{-3}$ µm^2. The corresponding heat density is $1.843{\cdot}10^{18}$ W/m^3. b) Time dependent temperature increase between 0 and 300 ns after switching the laser irradiation on.

the same period of time. The steady state times provided by the simulation are much faster than the known collapse time of the pNIPAM shell [135]. This allows the plasmonic heating of pNIPAM to be used to study the kinetics of the polymer phase transition. It is important to mention that simulated temperatures are considered as an approximation and the real values could vary by several degrees Celsius.

Based on the result of the theoretical calculation, a series of experiments using the estimated required power density of 880 kW/cm^2 are performed. During these experiments, extinction spectra with and without laser irradiation are recorded. Immediately after the laser irradiation starts, a clear difference in the extinction spectrum is observed. The spectral shift retains during the whole irradiation period. Again, two significant differences are visible. Firstly, the extinction in the low wavelength region around 500 nm (which is the lower limit of the employed spectrometer) shows an increase. This increase is explained by the collapsing microgel. Secondly, the plasmon resonance peak shows a considerable redshift, which is connected to the increase of the refractive index close to the gold nanorod surface. Both effects are denoted by I and II in figure 5.12a.

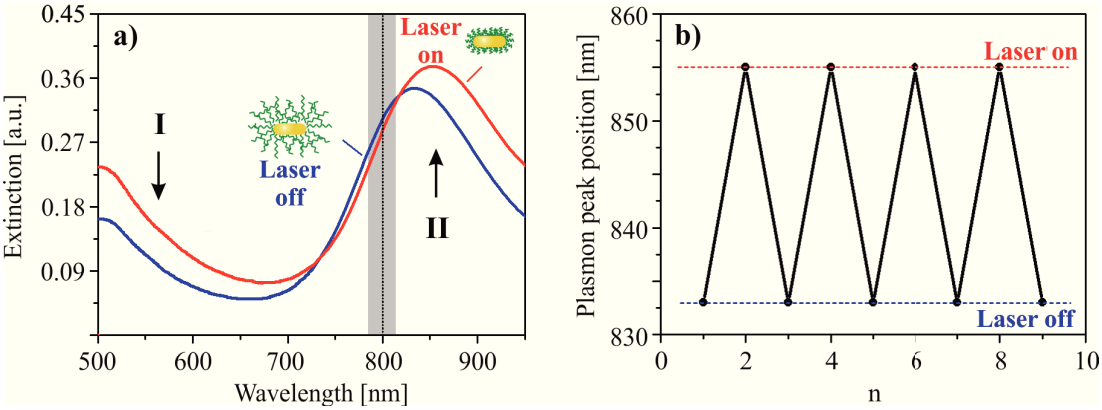

Figure 5.12: **Laser heating of a pNIPAM-nanorod suspension.** a) Extinction spectrum of the sample, without (blue curve) and with (red curve) laser irradiation. b) The reversibility of the longitudinal plasmon peak position after several laser irradiation events. (Adapted from [131])

The measured redshift of the longitudinal plasmon resonance is highly reversible, as shown in figure 5.12b: the original position of the peak around 833 nm shifts to 855 nm upon laser irradiation and blueshifts back to 833 nm after switching the laser off. The resulting spectral shift of 22 nm is smaller than the calculated value of 36 nm and the value provided by bulk heating measurements of 34 nm in the previous section. The reason for the lower red shift could be due to the beam overlap inside the sample: the white-light-probed volume of the sample is significantly larger than the laser-irradiated volume. On the one hand, a white light source has a bigger focal volume compared to a single wavelength laser beam because of optical aberrations. On the other hand, the focused laser beam has a Gaussian profile with the highest intensity locally in the middle of the beam. The power density at outer regions of the Gaussian beam is not sufficient to induce the phase transition of pNIPAM. Considering phase transitions of only 50% of the probed microgels, the theoretically estimated shift is around 20 nm, which is in a good agreement with experimental results. Experimentally observed broadening of the extinction spectrum during laser irradiation supports the assumption of different probing and heating volumes. The broader spectrum contains contributions of microgels in collapsed and swollen states.

So far, all calculations and experiments are performed under conditions that lead to the complete collapse of the polymer shell. If we reduce the power density of the heating laser, the temperature around the gold nanoparticle also drops. The distance to the nanorod surface, where the temperature is above the LCST, is smaller than the thickness of the fully collapsed shell. Therefore, the heat induced phase transition might occur only inside the inner part of the pNIPAM shell, which is close to the hot nanorod surface. At the same time, the temperature of the outer shell is below the LCST and still swollen. Further experiments were performed to prove the concept of a gradually collapsing pNIPAM shell.

Starting with the lowest power density of 145 kW/cm^2, a small 7 nm redshift of the longitudinal plasmon resonance peak is observed (inset in figure 5.13a). The corresponding simulated gold nanorod surface temperature is around 48°C and the region with a temperature above 33°C is approximately 40 nm away from the nanorod surface. The fully collapsed shell has a radius of around 90 nm, thus only the 40 nm thick inner part of the shell is collapsed and the outer part of the pNIPAM shell is swollen at 145 kW/cm^2. The small spectral shift is solely due to the increasing refractive index of the partially collapsed inner shell.

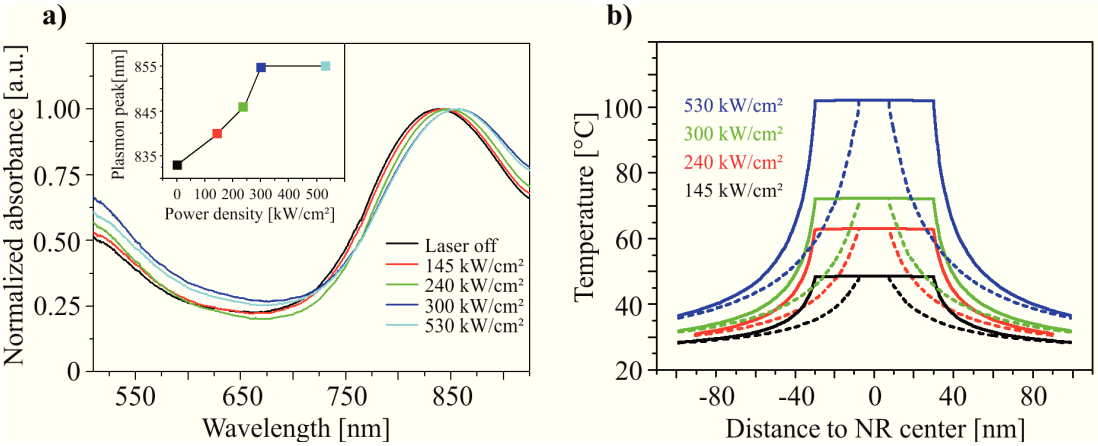

Figure 5.13: **Laser heating of pNIPAM-nanorod suspension with different power densities.** a) Spectra of the extinction at irradiating power densities between 145 and 530 kW/cm^2. The inset shows the position of the longitudinal plasmon peak versus the applied laser power density. b) Simulated heat distribution corresponding to the long (solid curves) and the short (dashed curves) axes of the nanorod at different power densities. (Adapted from [131])

During a stepwise increase of the power density above 145 kW/cm^2, a gradual redshift of the longitudinal plasmon resonance peak can be observed (inset in figure 5.13a). The size of the collapsed inner part of the shell is increasing, leading to the increase of the effective refractive index around the gold nanorod. The maximum redshift of 22 nm is reached at 300 kW/cm^2, at which the region above 33°C is approximately 100 nm from the nanorod surface. This distance corresponds to the radius of the fully collapsed pNIPAM shell, as measured by DLS. Even though the size of the swollen microgel is much bigger than 100 nm, the collapse of the inner core drags the outer shell into the hot regions. Due to this mechanism, the whole microgel is gradually collapsing, starting with the inner region. This mechanism is schematically illustrated in figure 5.14.

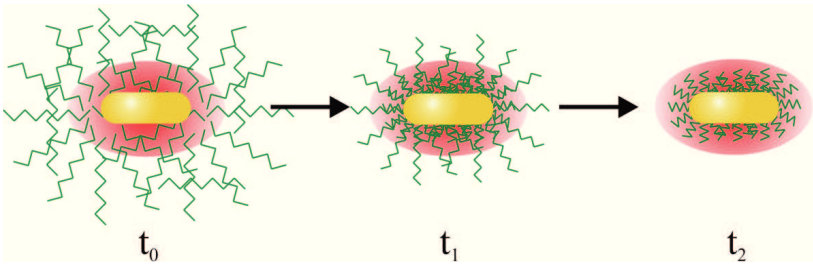

Figure 5.14: **Schematic view of the stepwise collapse process as result of plasmonic heating.** The temperature above the LCST is illustrated as a red region around the nanorod. After the temperature increase at the time t_0, the pNIPAM collapse starts only in the inner part of the microgel. At t_1 the inner part of the microgel is collapsed and drags the outer swollen shell into the hot region where it undergoes a phase transition and collapses at t_2.

This process is different compared to the bulk heating of pNIPAM-nanorod nanocomposite suspension, where the whole microgel volume is heated homogeneously and its collapse occurs at once. In contrast to plasmonic heating, bulk heating of pNIPAM microgel suspension cannot achieve a partial collapse of the polymer shell. By applying different laser powers, plasmonic heating allows the control of the ratio of the collapsed inner and the swollen outer parts of the polymer shell.

5.2.3 Summary and outlook

Both experiments based on bulk and plasmonic heating of pNIPAM coated gold nanorods illustrate the high sensitivity of plasmonic nanoparticles to refractive index changes of the thermally-addressable surrounding medium. Laser heating of pNIPAM-nanorod composites confirm the possibility of complete or partial triggering of polymer phase transition. Local plasmonic heating provides phase transitions only within the focus of the laser beam, the remaining suspension is not affected. A strongly focused laser beam with a diffraction limited spot size of around 600 nm can be used to irradiate only few or even an individual pNIPAM-nanorod nanocomposite. This might allow selective triggering of each single nanocomposite by local optothermal control.

As explained in the theoretical part of this thesis (chapter 2.3), a focused laser beam with 800 nm wavelength exerts a strong optical force on a gold nanorod. The longitudinal plasmon resonance of a swollen pNIPAM-coated nanorod is around 825 nm, which leads to a strong scattering force acting on a nanocomposite along the beam propagation direction. In suspensions containing many nanocomposites, the optical force will not affect the total signal. PNIPAM-nanorod nanocomposites pushed out from the focus below the focal plane are replaced by other nanocomposites pulled into the focus above the focal plane. For single particle experiments, the strong optical force occurring at resonant wavelengths makes selective triggering of single pNIPAM-nanorods not feasible.

A possible approach for single particle experiments can be realized by immobilizing microgel particles on a substrate surface. Individual pNIPAM microgels are visible as a strong scattering structure in the DFM, which allows precise laser focusing on each single nanocomposite. Alternatively, to perform selective measurements and exclude any substrate contribution, it is reasonable to use optical tweezers. A single nanocomposite held inside an optical trap can be simultaneously heated by the trapping laser or by using an additional resonant laser. Previous investigations prove the possibility of thermal manipulations and spectroscopic analysis of optically trapped single nanoparticles [118, 136].

Additionally, laser heating experiments are suitable to investigate the kinetics of the collapse and swelling process of the pNIPAM shell. The steady state

temperature of the microgel is reached within less than 300 ns by using plasmonic heating of gold nanorods. This time can be decreased by preheating the sample close to phase transition temperature. A simulated temperature increase from 30 °C to 34 °C takes less than 100 ns, which is much faster than the collapse time of the microgel (≈600 ns [135]).

6 Nanofabrication with an optically driven gold nanoparticle

In this chapter we introduce and investigate a novel method for polymer nanofabrication by means of simultaneous plasmonic heating and optical guiding of gold nanoparticles. We apply different degrees of plasmonic heating to induce thermal degradation or to accelerate the cross-linking reaction of a polymer. In both cases it is possible to displace gold nanoparticles by applying strong optical forces exerted by a resonant laser beam.

6.1 Milling with an optomechanically driven gold nanoparticle

The strongly localized heat distribution around plasmonically heated gold nanostructures makes them an intriguing candidate as a nanoscopic heat source. Many applications requiring a defined and highly localized temperature increase are based on plasmonic heating of gold nanostructures. In addition, the remote triggering of the heating process can be controlled by electromagnetic radiation. During the last decade, a considerable amount of novel applications, such as selective and remotely triggered drug release [137, 138], cancer diagnostics and treatment [31, 139], optofluidic control [140, 141], DNA melting analysis [27] or photothermal imaging [142], were realized by the concept of plasmonically heated gold nanostructures.

6.1.1 Embossing of gold nanoparticles by optical forces and plasmonic heating

The scattering force acts on a gold nanoparticle along the beam propagation direction (chapter 2.3). In a certain arrangement it is possible to exert optical force on a single gold nanoparticle and push it against a polymer layer. This is the case, if the gold nanoparticle is placed exactly in the focal point of a focused laser beam, which propagates perpendicular to the polymer surface.

Plasmonic heating and optical forces while embossing

Prior calculations are necessary to determine the most important factors influencing the experiment: the heat distribution around the gold nanoparticle and the optical force acting on it. Without heat-induced melting of the polymer, the embossing process would require a much stronger force. Thus, the temperature increase and the heat distribution around the gold nanoparticle has to be calculated as precise as possible.

The surface temperature of the gold nanoparticle strongly depends on the amount of the absorbed light. After the fast temperature increase inside the

gold nanoparticle, the heat dissipates to the surrounding medium until a thermal steady state is reached. The steady state temperature and the spatial heat distribution around the gold nanoparticle depend strongly on thermal properties of the surrounding medium. Especially, the thermal conductivity of the surroundings plays an important role. The amount of the thermal energy dissipating from the heat source is increased with higher values of the thermal conductivity, which leads to lower steady state temperatures.

Considering the same amount of the absorbed electromagnetic energy, different thermal conductivities lead to significantly different temperatures. These temperatures are low for nanoparticles in fluids or inside polymer matrices, and increase significantly for gold nanoparticles surrounded by air. Due to its low thermal conductivity, air acts as a better thermal insulator compared to water or polymers. Figure 6.1 illustrates this effect.

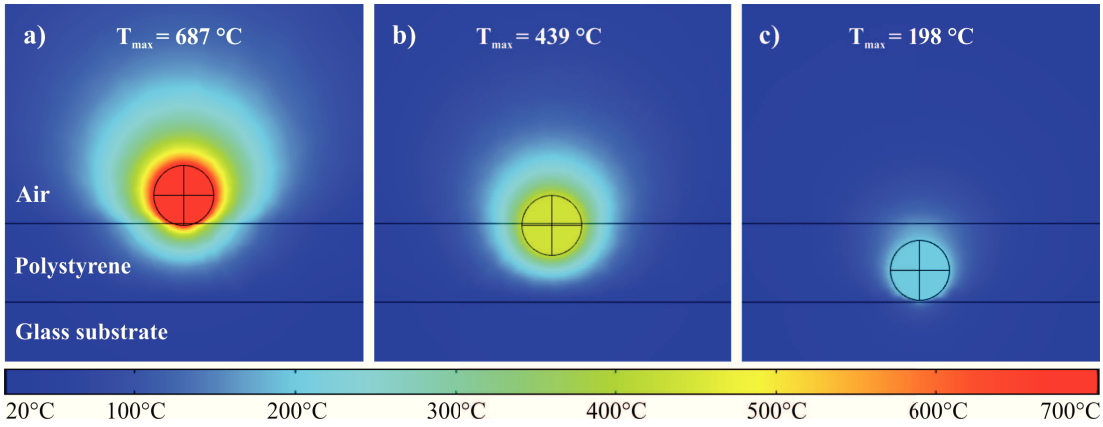

Figure 6.1: **Simulated heat distributions around a single gold nanoparticle with 80 nm diameter under different conditions.** a) The gold nanoparticle is on top of a 100 nm thick PS layer. b) The gold nanoparticle is half embedded into the PS layer. c) The gold nanoparticle is completely embedded into the polymer. In all three cases the amount of the absorbed laser power per volume is 10^{17} W/m^3.

We compare temperature distributions around a single 80 nm gold nanoparticle on top of a polymer layer, half and completely embedded into a polymer matrix. The result of the simulation is shown in figure 6.1. In all three calculations, the gold nanoparticle acts as the only heat source with a defined amount of absorbed laser power per volume Q = 10^{17} W/m^3. The result of the sim-

ulation shows, that in air the steady state temperature induced by the same amount of absorbed power is more than tree times higher. The reason is the lower thermal conductivity of air ($\kappa_{air} \approx 26$ mW/(m· K))[143] compared to PS ($\kappa_{PS} \approx$140 mW/(m·K)) [144].

The previous simulation does not take into account, that the absorption cross section of the gold nanoparticle is connected to the refractive index of the surrounding medium. To calculate the realistic temperature distribution for every embossing step, we have to apply the Mie theory and calculate different absorption cross sections regarding the changing effective refractive index of the nanoparticle surroundings. Figure 6.2a shows the calculated absorption cross section of an 80 nm gold nanoparticle for different refractive indexes of the surrounding medium and a fixed wavelength of 532 nm.

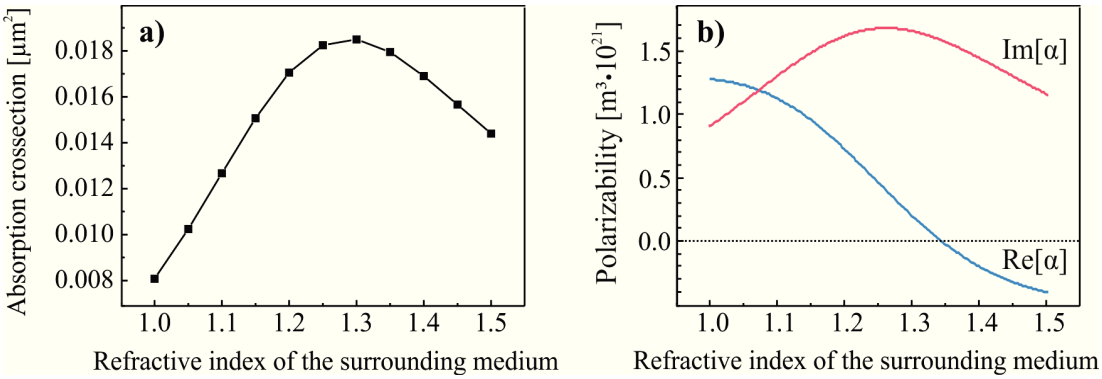

Figure 6.2: **Dependence of the absorption cross section and the polarizability on the refractive index.** Calculated values for the absorption cross section (a) and the complex polarizability (b) of an 80 nm gold nanoparticle at 532 nm versus the refractive index of the surrounding medium.

Additionally, the change of the surrounding medium affects strongly the optical forces. As shown before, the scattering force depends on the imaginary part and the gradient force on the real part of the nanoparticle polarizability. The changing complex polarizability of an 80 nm gold nanoparticle at a fixed wavelength of 532 nm is shown in figure 6.2b. Since the laser beam is focused exactly on the gold nanoparticle, the contribution of the gradient force is negligible due to the absence of the intensity gradient in the focal point. The main contribution to the total force comes from the scattering force.

Experimental configuration

The sample contains gold nanoparticles of 80 nm diameter on top of a thin polymer layer. This configuration is not possible using water soluble polymers, such as PVA, since gold nanoparticles are dispersed in aqueous solution. In such a case, a thin water soluble polymer layer is dissolved during the nanoparticle drop casting process.

PS shows no solubility in water, but can be dissolved in organic solvents. The sample is prepared in a two steps process: spin coating of the polymer layer followed by drop casting of colloidal gold nanoparticles on top of the polymer, as shown in figure 6.3. Plasma treatment of the PS layer increases its hydrophilic properties, which leads to a better drop casting efficiency. The particle concentration is chosen such that the distance between individual gold nanoparticles after drop casting is well above the laser spot size.

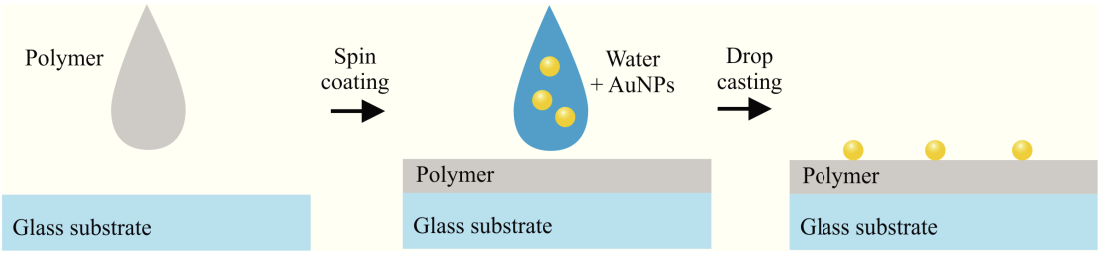

Figure 6.3: **Gold nanoparticles on top of a PS layer.** Polystyrene is dissolved in a nonpolar solvent and spin coated as a thin layer on a glass substrate. Afterwards, colloidal gold is drop casted on top of the polymer layer.

The experimental configuration is realized using a modified DFM with a coupled laser beam, as shown in figure 6.4. The laser beam, bundled by the same objective as used for observation, is focused exactly on a gold nanoparticle located on top of the polymer layer. A thin transparent layer of PS with a thickness around 100 nm is chosen as a model polymer for this experiment. The increasing deformability of PS above the glass transition temperature and the melting point makes it possible for the gold nanoparticle to penetrate the polymer matrix. Optical forces promote the embossing process of the nanoparticle.

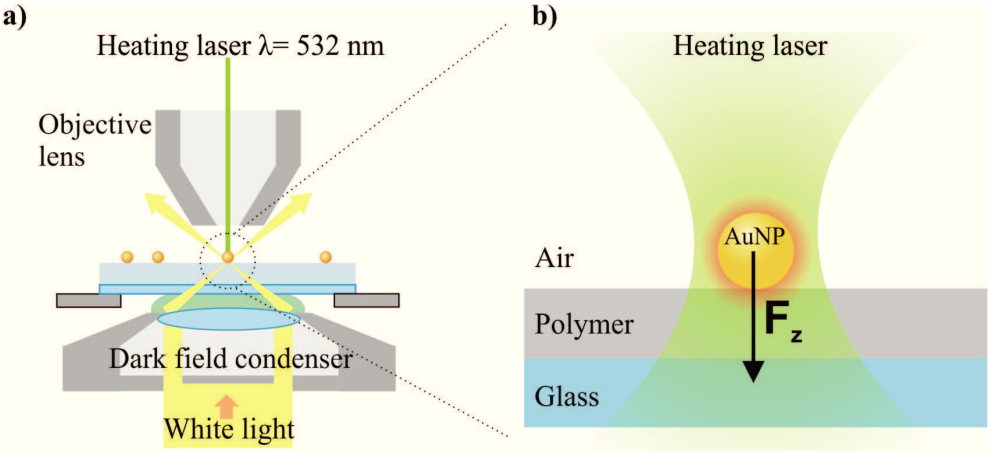

Figure 6.4: **Schematic view of the embossing experiment.** a) The DFM is extended with a 532 nm heating laser which is focused by the same objective as used for observation. b) Detailed view of the area around the gold nanoparticle. $\mathbf{F}_z$ is the total optical force acting on the gold nanoparticle.

Results of the embossing experiment

Observed by the DFM in air, the gold nanoparticles appear as bright, green scatterer. In comparison, same nanoparticles appear yellowish in water, which is a result of the larger refractive index of water compared to air. The color of the light scattered by the nanoparticles on the sample is almost identical, which is a sign of a high monodispersity. A dark field image of a group of five gold nanoparticles before laser heating is shown in figure 6.5a.

During the experiment, the laser beam from the objective is focused on individual gold nanoparticles. The laser beam and the gold particles appear as diffraction limited spots if observed by the DFM. Therefore, a highly precise overlap of both spots is required to reproduce the experimental conditions for each gold nanoparticle. This process is carried out semi-manually: in x- and y-directions by using a stepping motor and in z-direction by moving the focus of the microscope. The overlay quality is controlled by eye.

In this experiment, the scattered light of the gold nanoparticle is the mostly indicative response of changing surrounding conditions. The laser power is increased gradually from zero until a visible change in the scattered light appears. It is notable that different scattering colors and intensities appear during the laser

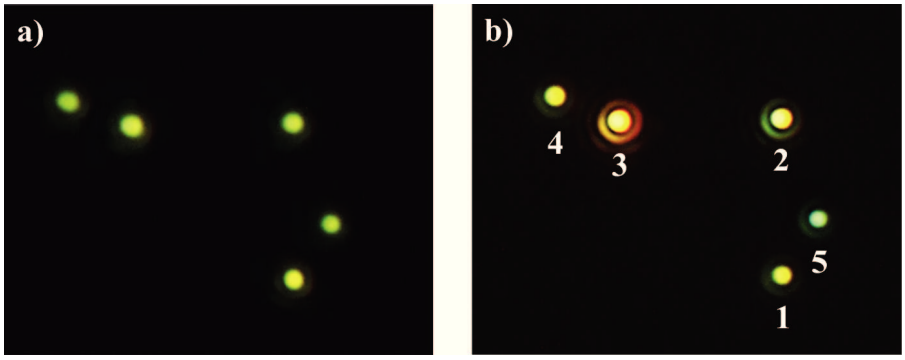

Figure 6.5: **Dark field images of gold nanoparticles before and after laser irradiation.** a) Five gold nanoparticles before laser irradiation. b) Particles after laser irradiation. Ascending numbers correspond to an increasing laser intensity.

power increase. The original greenish color of non-irradiated gold nanoparticles changes to brighter yellow and afterwards to more bright orange. Further increase of the laser intensity changes the nanoparticle color to green-yellow again and to bluish color at highest laser intensities. The result of the experiment is shown in figure 6.5b. Number 1 correspond to the non-irradiated gold nanoparticle. The ascending numbers denote an increasing laser intensity.

In order to investigate each step of the embossing process, the laser intensity increase is stopped after each pronounced change of the scattered light. The scattering spectra of all gold nanoparticles are recorded with a CCD spectrometer. The corresponding laser powers are measured with a power meter. These values allow to calculate the laser power density, the resulting nanoparticle temperature, and the optical force.

After the experiment, the same substrate area is investigated in detail using AFM and SEM. Due to the high reproducibility of the embossing experiment, images from different experimental series show highly comparable structures. The results are summarized in figure 6.6.

The AFM and SEM clearly show different steps of the embossing process and the following thermal degradation of the polymer. In the beginning, the gold nanoparticle is located on top of the polymer layer, where it remains until the laser intensity is sufficient to melt and soften the polymer layer underneath. This first step of the embossing process occurs at a power density around 14 kW/cm^2

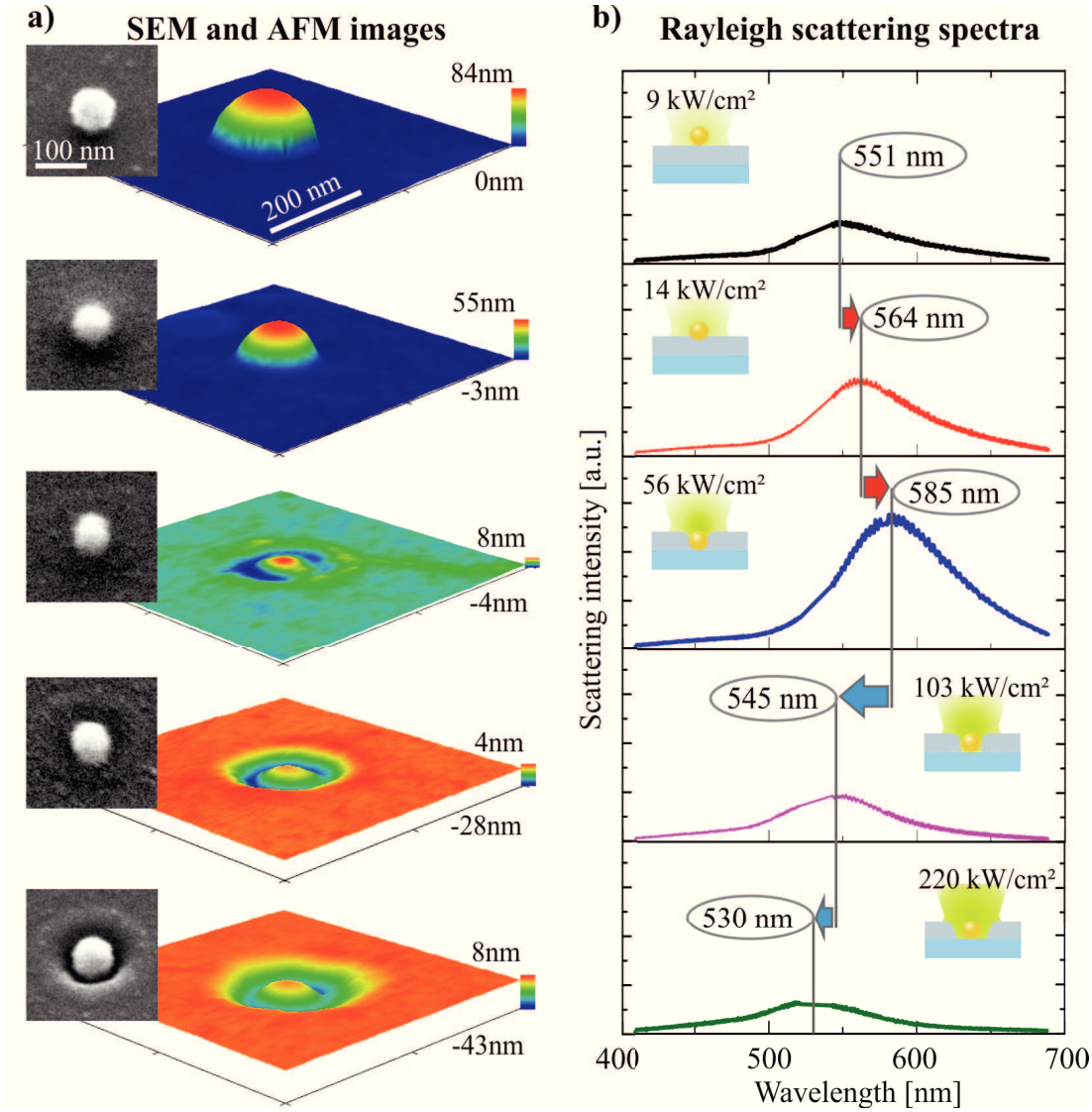

Figure 6.6: **Embossing of gold nanoparticles into a polymer layer.** a) SEM (black and white images, the angle between the sample and the detector is 60°) and AFM (color images) clearly show embossing of an 80 nm gold nanoparticle into the PS layer upon plasmonic heating at lower laser powers and crater formation around the nanoparticle due to the thermal degradation of the PS at higher laser powers. b) Rayleigh scattering spectra show an increasing effective refractive index around the nanoparticle seen as a red shifting and strengthening of the gold nanoparticle scattering. The crater formation results in a blue shift of the spectra, which occurs due to a decrease of the effective refractive index around the nanoparticle. The laser power densities are shown in each frame. (Adapted from [145])

and shows a slight color change of the scattered light. The gold nanoparticle is partly embossed into the polymer by an optical force acting perpendicular to the polymer layer. A further increase of the laser power density to 56 kW/cm^2 leads to temperature rise around the gold nanoparticle and stronger optical forces. The gold nanoparticle is thus pushed deeper into the polymer matrix until it is completely surrounded by the polymer. In these experiments the thickness of the polymer layer is of the same order as the diameter of the gold nanoparticle. The embossing process stops as soon as the nanoparticle reaches the glass surface. The softening temperature of borosilicate glass is above 800°C [146], which is much higher compared to the glass transition temperature of PS at around 100°C.

The scattering spectrum of a fully embedded gold nanoparticle shows the biggest redshift compared to the original spectrum in air. Inside the polymer matrix the effective refractive index of the surrounding medium has the highest value. A further increase of the laser power density to 103 kW/cm^2 heats the gold nanoparticle until its surface temperature is high enough to degrade the surrounding stabilizing ligand layer, which is cetyltrimethylammonium bromide (CTAB). At temperatures around 210°C CTAB shows first signs of thermal degradation [147]. The thermal degradation process starts at the region with the highest temperature: directly on the gold nanoparticle surface. The result of the thermal degradation process is a thin polymer-free layer around the gold nanoparticle, which has a lower thermal conductivity as the polymer matrix. This thermally insulating layer increases the surface temperature of the gold nanoparticle, which leads to further degradation of the surrounding polymer matrix. The process stops, when the polymer layer cannot be degraded by the heat of the gold nanoparticle. During this process, the effective refractive index of the surroundings is reduced, which leads to a blueshift of the plasmon resonance. The peak of the scattered light shifts from orange (580 nm) to yellow-green (545 nm).

During the next heating step with the highest laser power density of 220 kW/cm^2 the plasmon resonance shifts further to shorter wavelengths. The resulting color is even more blueshifted, than the original color of the gold nanoparticles at the beginning of the experiment. This behavior can be explained by a lower refractive index of the glass substrate compared to the polymer matrix. The role of the

substrate refractive index and its contribution to the effective refractive index is explained in the following passage.

The role of the effective refractive index

To compare the experimentally measured scattering spectrum with the calculated values, it is important to clarify the contribution of the substrate to the effective refractive index around the gold nanoparticle. Before irradiation, gold nanoparticles are deposited on top of the PS layer. This can be proved by analyzing the scattering spectra of gold nanoparticles and by SEM and DFM images of the polymer surface. The main surrounding medium around the gold nanoparticle is air, which has a refractive index $n_{air} = 1.00$. At the same time, the gold nanoparticle is touching the polymer surface, which has a higher refractive index $n_p = 1.59$ [148]. To be able to calculate the exact scattering cross section by using the Mie theory, an effective refractive index n_{eff} is introduced. The effective refractive index is a combination of refractive indexes of both materials with different contributions. In the case of a planar polymer layer as a substrate, the effective refractive index is calculated as [149]:

$$n_{eff} = \alpha \cdot n_{air} + (1 - \alpha) \cdot n_p. \tag{6.1}$$

For this equation the weighting factor α is calculated using an approach based on an exponential decrease of the nanoparticle's refractive index sensitivity with increasing distances to its surface. Integrating from the gold nanoparticle surface to the infinity provides a weighting factor $\alpha = 0.7$ for the air-surrounded part of the particle. The substrate contribution is weighted with a factor 0.3.

The measured scattering spectra of the gold nanoparticles are shown in figure 6.7. A Mie theory based calculation using an 80 nm gold nanoparticle and the calculated effective refractive index $n_{eff} = 1.156$ is shown in the same graph. We have to consider a thin ligand layer (CTAB) on the surface of the gold nanoparticle. The CTAB layer has a thickness of 4.4 nm [150] and a refractive index of 1.435 [151]. Both, theoretical and experimental spectra are in a good agreement to each other.

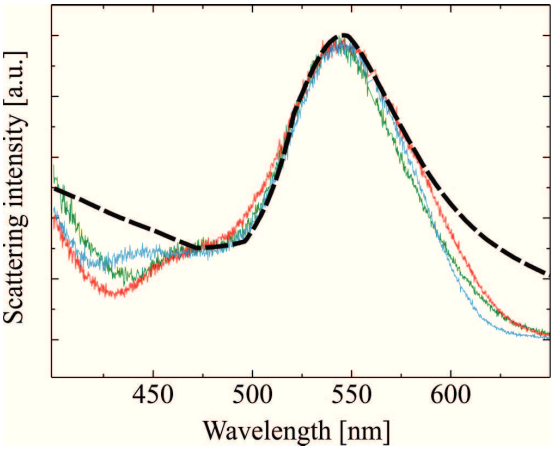

Figure 6.7: **Comparison of theoretical and measured scattering spectra.** Black dashed line: theoretically calculated scattering spectrum of an 80 nm gold nanoparticle. Measured spectra of drop casted 80 nm gold nanoparticles (thin red, blue and green lines).

Same calculations are done for the following embossing steps. It is important to calculate the contribution of all surrounding materials, depending on the embossing stage. The refractive index of air is 1.00, of PS is 1.59 [148] and of glass is 1.51 [152]. Considering the geometry and the equation (6.1), the refractive index contribution can be split into three layers, above and below the gold nanoparticle (each weighted with 0.3) and the layer containing the gold nanoparticle (weighted with 0.4). The stabilizing CTAB layer around the gold nanoparticle remains until the third heating step, where the ligand layer is thermally degraded. The corresponding effective refractive indexes are listed in figure 6.8a for each heating step. In the third step we assume that the nanoparticle is still not in contact with the glass surface. It touches the glass surface in the following two steps, which is proved by comparing the height of the polymer surface relative to the gold nanoparticle surface on the AFM image (figure 6.6a, between the third and fourth embossing steps). By using the calculated values for each effective refractive index, we calculate the corresponding scattering cross sections (figure 6.8b). The calculated peak position is in a good agreement with the measured values, which are shown in each frame.

After obtaining the exact effective refractive index and precise determination of the particle position inside the polymer layer, it is possible to calculate the temperature increase and the optical force on the nanoparticle during each embossing step. The resulting temperature distribution and optical force in z-direction are

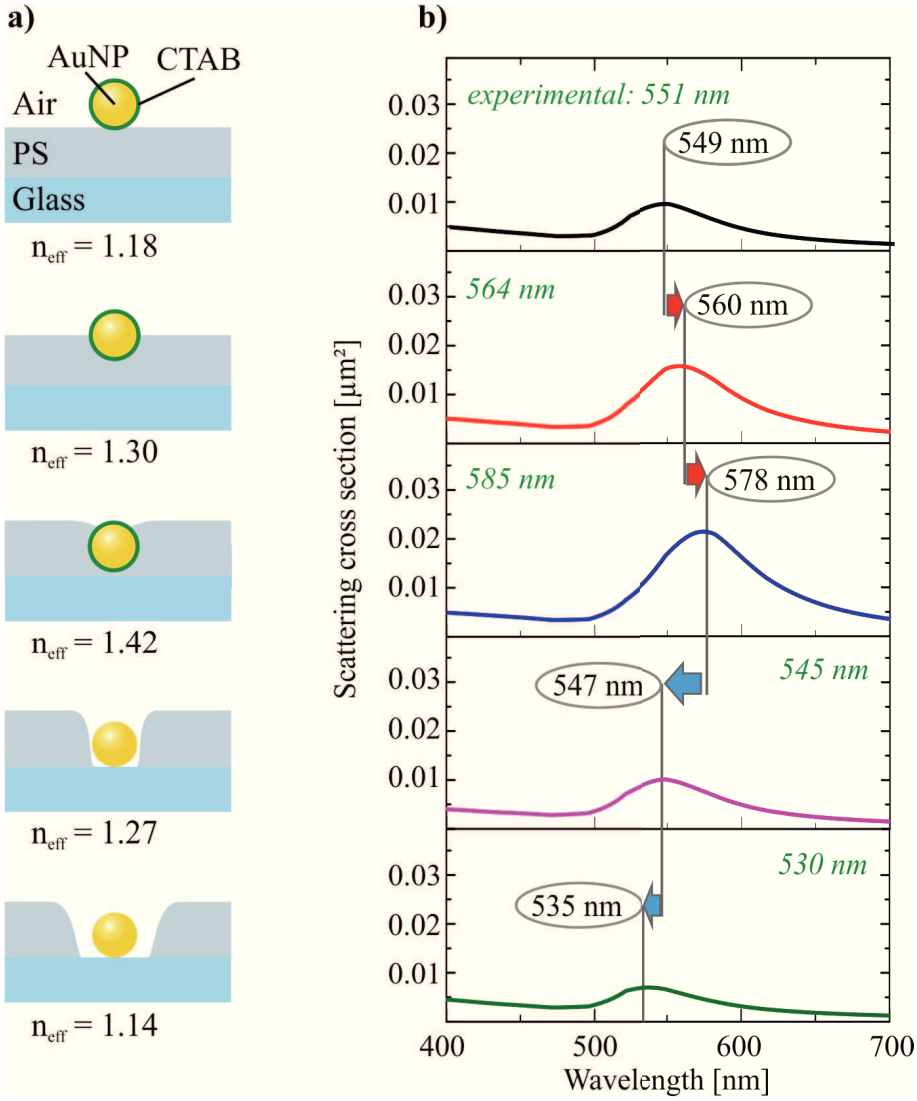

Figure 6.8: **Theoretical calculation of scattering cross sections for different embossing steps.** a) Schematics of each embossing step with the corresponding effective refractive index n_{eff}. b) Calculated scattering cross sections for each n_{eff}. Corresponding measured values are shown in green as an inset.

shown in figure 6.9. Since laser embossing is a dynamic process, only the starting condition of every step is simulated, as explained in the following.

Before irradiation, the gold nanoparticle is placed on top of the polymer layer and the first visible color change is observed at laser power densities of 14 kW/cm^2 with a corresponding nanoparticle temperature of about 115°C. This tempera-

ture is above the glass transition temperature of PS (100°C) and the underlying polymer surface becomes soft. At the same time, the optical force of 0.085 pN is pushing the gold nanoparticle into the polymer matrix. Polystyrene has a higher thermal conductivity, which again decreases the nanoparticle surface temperature by increasing the heat dissipation rate. The embossing process stops, when the nanoparticle temperature drops below the glass transition temperature and the polymer becomes solid. The applied optical force is not sufficient to press the nanoparticle into the solid PS. At the end of this step the gold nanoparticle is partly embedded in the polymer matrix.

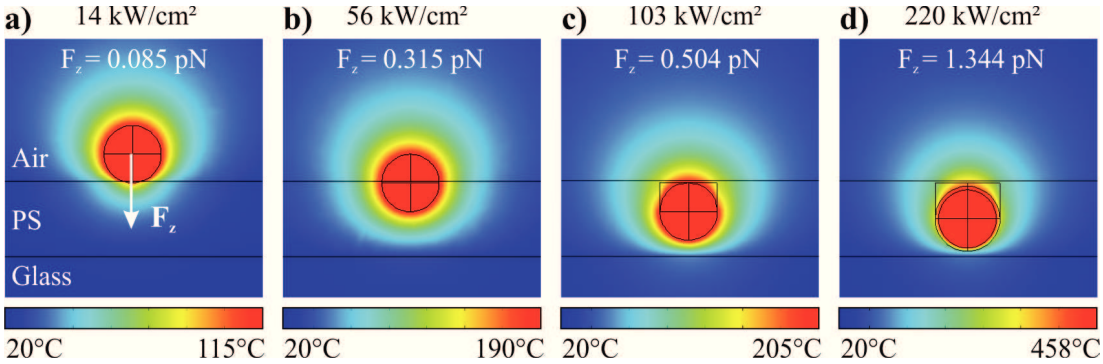

Figure 6.9: **Simulated temperature distributions for each embossing step.** a) The gold nanoparticle is on top of the polymer layer before being pushed into the polymer layer. b) The next step with a partly embossed nanoparticle. c) The gold nanoparticle is inside the polymer matrix, the degradation of the ligand layer starts. d) The nanoparticle is close to the glass substrate, a further increase of the polymer-free area is observed.

Further increase of the laser power density is necessary to soften the polymer again and continue the embossing process. At power densities of 56 kW/cm^2 the partly embossed gold nanoparticle is pressed by an optical force of 0.315 pN until it is almost completely surrounded by the polymer. The calculated temperature at the beginning of the process is 190°C, which is well above the glass transition temperature. The process stops again, when the high thermal conductivity of the polymer matrix reduces the steady state temperature of the gold nanoparticle at the applied power density.

During the next heating step the laser power density of about 100 kW/cm^2 leads to the nanoparticle temperature above 200°C. At these temperatures the

stabilizing ligand around the gold nanoparticle (CTAB) starts to degrade, which creates a thin thermally insulating layer followed by a raise of the temperature around the gold nanoparticle. A crater or a well-like structure is formed around the nanoparticle due to thermal degradation of the polymer matrix. Higher power densities increase the size of the well structure around the gold nanoparticle by further degradation the polymer. The size of the well structure is limited by the thermal stability of the gold nanoparticle. It is known from the literature that spherical gold nanoparticles are relatively stable up to 1065°C [153], which is the melting temperature of gold. At this temperature, the theoretically predicted well diameter would be about 300 nm.

Overall, the simulated temperatures are in a good agreement with the experimental results regarding the glass transition and thermal degradation temperatures of PS. The embossing process of the gold nanoparticle occurs at temperatures above the glass transition of PS, when the solid polymer becomes soft and allows the penetration by the gold nanoparticle. Growth of a well structure around the gold nanoparticle is observed only at temperatures above the thermal degradation temperature of PS. These theoretical considerations allow to predict the experimental result, in order to create partially embedded nanoparticles with a desired embedding ratio, or to create nanoscopic well structures with certain diameters around a single gold nanoparticle.

During all laser mediated embossing experiments, the total optical force acts along the optical axis, which is perpendicular to the polymer and substrate surfaces. Such a configuration is only possible if the gold nanoparticle is placed exactly on the optical axis of the focused laser beam. For particles above and below the focal plane and outside the optical axis, the total optical force exhibits components which are parallel to the polymer and substrate surface. These radial components of the optical force open a possibility to move gold nanoparticles laterally on the substrate surface by irradiating them with a focused laser beam.

6.1.2 Subdiffraction-limited milling with a single gold nanoparticle

As shown in figure 2.12, theoretical calculations predict not only a strong scattering force in the region of the plasmon resonance, but also a repulsive gradient force acting on a gold nanoparticle, which is surrounded by high refractive index media (e.g. polymers). Under special experimental conditions these forces are sufficient to move gold nanoparticles inside a polymer matrix. A combination of nanoparticle movement with plasmonic heating induced by the same laser beam appears to be an interesting optothermal and optomechanical tool.

Plasmonic properties of gold nanoparticles, however, appear to be a disturbance for controlled optomechanical manipulations for the reason that as soon as the scattering force overcomes the gradient force, the nanoparticle is pushed out of the optical trap. Additionally, the temperature of the trapped gold nanoparticle might disturb optical trapping and leads to release of trapped nanoparticles [118].

High temperatures are required to melt and degrade a polymer matrix, which is achieved by irradiating the gold nanoparticle with resonant wavelengths at laser powers of several milliwatts. Also, the total optical force on a gold nanoparticle by a focused laser beam at resonant conditions ($\lambda \approx 570$ nm) is two order of magnitude higher, than the total force at wavelength far away from the plasmon resonance (e.g. $\lambda \approx 1000$ nm).

Repulsive optical forces on plasmonic nanoparticles

The calculated total force distribution exerted on a spherical gold nanoparticle by a focused laser beam is shown in figure 6.10a. The diameter of the nanoparticle is 80 nm, the surrounding medium has a refractive index of 1.55 and the laser beam with a wavelength of 532 nm, which is focused with NA = 0.9. The beam propagation direction is along the z-axis from top to bottom. Additionally, only the radial component (perpendicular to the propagation direction) of the optical force is shown in figure 6.10b. It is remarkable that the radial force acts toward the optical axis above the focal plane (attractive radial force) and away from the optical axis below the focal plane (repulsive radial force). Considering the radial components of the force only, a successful movement of the gold nanoparticle

should be possible by using the stronger repulsive radial component, rather than the weaker attractive component of the optical force.

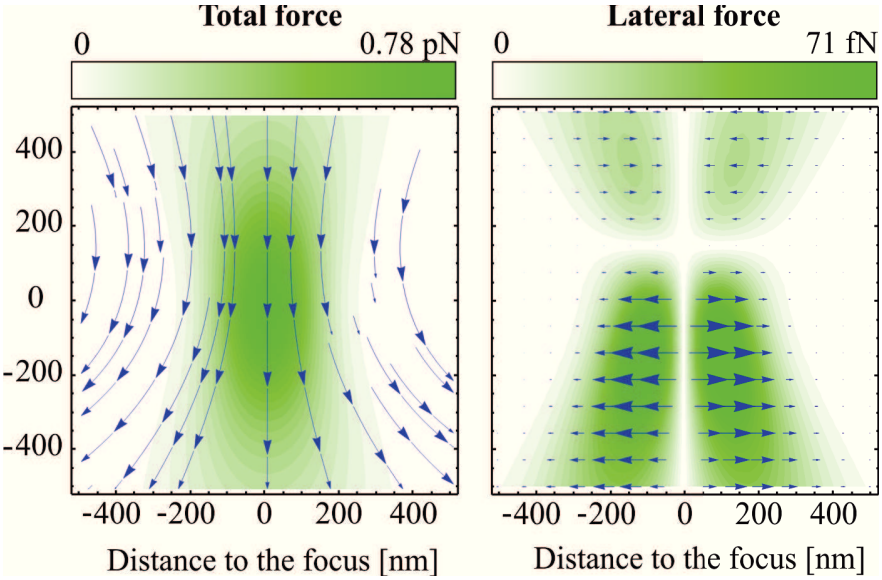

Figure 6.10: **Calculated optical forces on a gold nanoparticle.** a) The total optical force on an 80 nm gold nanoparticle inside a polymer matrix, exerted by a 532 nm laser beam, which is focused with a 0.9 NA objective. The beam intensity is 1 mW. b) The radial component of the total optical force on the same nanoparticle at same conditions. The radial component of the optical force is one order of magnitude weaker than the total optical force. In this plot, the size of arrows exceptionally corresponds to the magnitude of the force.

In the case of gold nanoparticles on a glass surface and a focused laser beam propagating perpendicular to the surface, the underlying substrate confines the movement of the gold nanoparticle in z-direction. The particles can therefore only be moved in x- and y-directions: there is no force component acting into the positive z-direction (compare with figure 6.10a). The glass substrate cannot be penetrated by the resonantly irradiated gold nanoparticle. In several heating experiments performed as a control, the gold nanoparticle is destroyed by plasmonic heating before the surface of the glass substrate is observably modified by the produced heat.

The radial component of the optical force on a gold nanoparticle shows its highest values slightly below the focal plane in a region between 150 and 200 nm away from the optical axis (figure 6.10b). At the same time, the refractive index of

the surrounding medium plays an important for the total optical force. Previous calculations show a repulsive gradient force, which appears in high refractive index surrounding media (chapter 2.3). This effect is predicted for surrounding media with $n > 1.35$, and cannot not observed in air or water. Therefore, the favorable configuration with a strong radial component of the total optical force is provided by a gold nanoparticle on a glass surface and fully embedded inside a polymer matrix.

The setup configuration and experimental results

The sample contains gold nanoparticles inside the polymer layer. This configuration was achieved by using a water soluble polyvinyl alcohol (PVA) polymer. Colloidal gold nanoparticles with diameters of 40 or 80 nm are mixed with the polymer-water solution. Afterwards, the polymer-nanoparticle suspension is spin coated on a glass substrate (6.11). The polymer density and the spin coating speed determine the thickness of the polymer layer.

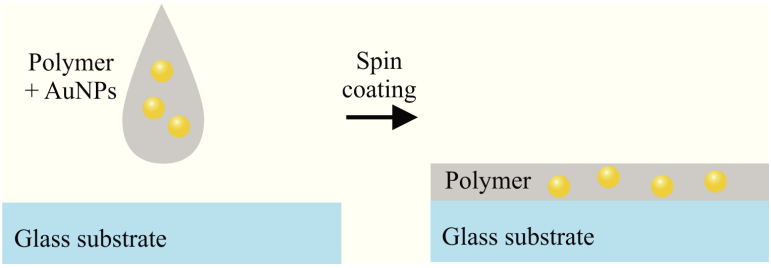

Figure 6.11: **Polyvinyl alcohol with gold nanoparticles.** A polymer solution with gold nanoparticles is spin coated on a glass substrate. The water solubility of polyvinyl alcohol allows direct mixing of colloidal gold with the dissolved polymer.

The resulting thickness of the polymer layer is on the same order as the gold nanoparticle diameter and most of the gold nanoparticles are embedded inside the resulting polymer layer. The low distribution density of gold nanoparticles inside the polymer allows single particle manipulation: the typical distance between the singe nanoparticles inside the polymer matrix is on order of several micrometers. Each nanoparticle is controlled by recoding its scattering spectrum to exclude aggregated nanoparticles from the experiment.

Both optical forces (scattering and gradient force) are connected to the intensity of the focused beam. In order to move gold nanoparticles over distances bigger than the spot size, the substrate is moved toward the focused beam. The further displacement of the gold nanoparticle is guided by the laser spot. At the same time, the localized heat generated by the gold nanoparticle leads to melting and thermal degradation of the polymer matrix close to the nanoparticle surface. The result of the experiment is a groove in a polymer matrix, which appears along the displacement path of the gold nanoparticle. This process is shown schematically in figure 6.12.

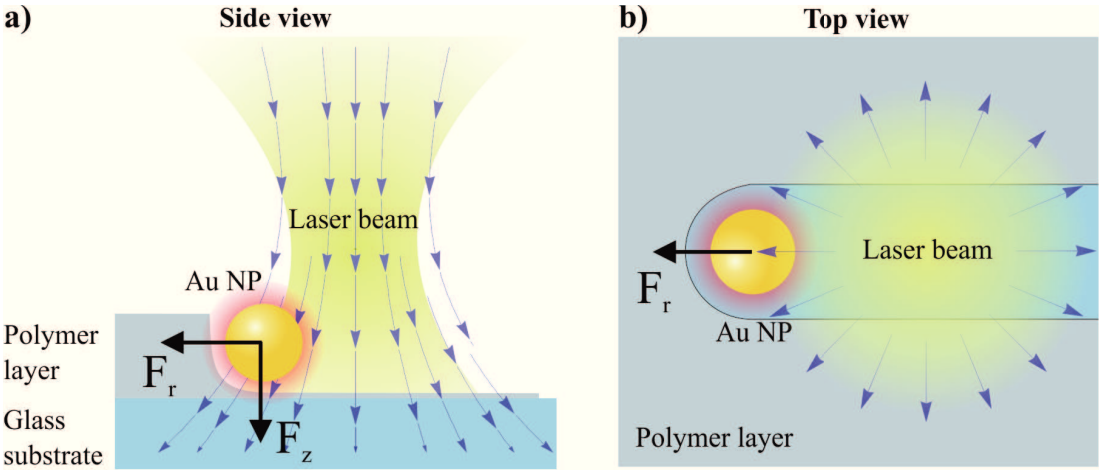

Figure 6.12: **Schematic view of the nanoparticle milling process.** a) Schematic view of the milling experiment. A slightly defocused laser beam is used to displace the nanoparticle laterally. b) Top view of the experimental arrangement: the radial component of the laser beam pushes the gold nanoparticle away from the region of the highest intensity. The hot gold nanoparticle moves and decomposes the surrounding polymer matrix.

The particle moving experiment is performed inside the modified DFM, which allows simultaneous observation and manipulation of the sample. The laser beam with a wavelength of 532 nm is focused slightly above the substrate surface and its height is controlled manually by defocussing the observed image. The exact position of the beam on the sample surface is achieved by using precise stepping motors for the x and y axes.

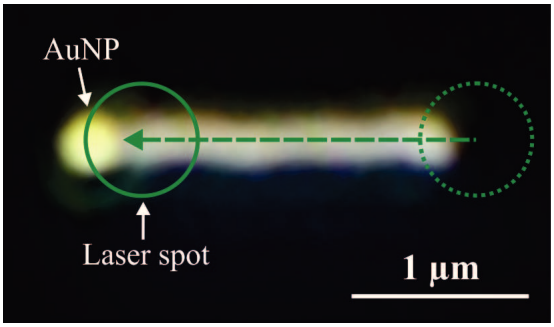

Figure 6.13: **The milling experiment.** A slightly defocused laser beam is used to displace the nanoparticle laterally. The original position of the beam is marked with a dashed green circle. The green arrow denotes the nanoparticle movement and the resulting structure inside the polymer matrix.

During the experiment, the laser spot is moved with a defined speed towards the gold nanoparticle. Typical values for the speed vary between 1 and 5 μm/s. The applied laser power is set between 4 and 10 mW. When the heat around the gold nanoparticle is sufficient to melt and degrade the surrounding polymer matrix, the gold nanoparticle is immobilized and can be guided by the laser spot. An elongated (several microns long) scattering structure is produced by the moving gold nanoparticle (6.13). The movement of the nanoparticle stops, as soon as it leaves the spot area and the nanoparticle surrounding temperature drops below the thermal degradation temperature of PVA. Due to the round shape of the laser spot and the radial distribution of the optical force, the displacement process of the gold nanoparticle must be simultaneously corrected.

After the manipulation step, the grooves produced in the polymer layer are investigated with an AFM. The resulting images are shown in figure 6.14. A thin artificial groove is found on the polymer surface. The shape of this channel corresponds to the structure observed in the DFM. In both cases with different gold nanoparticle sizes, the thickness of the resulting channel corresponds to the nanoparticle diameter. The groove, made with a 40 nm gold nanoparticle has a width of 49 nm. By using an 80 nm gold nanoparticle, the width of the resulting groove is increased to 98 nm. Both sizes are well below the diffraction limit of the applied laser beam with 532 nm wavelength. The assumption of the thermal degradation of the polymer is supported by the AFM images: no signature of polymer pressed out by the nanoparticle is observed around the produced groove. The polymer inside the groove is degraded by the heat around the gold nanoparticle.

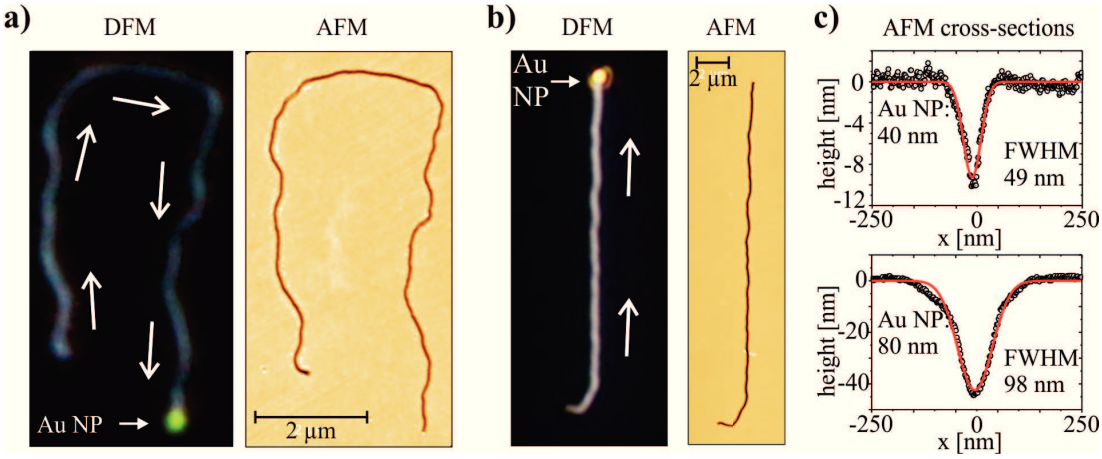

Figure 6.14: **Grooves formed by gold nanoparticle milling.** a) A dark field image of the groove made with a 40 nm nanoparticle. Same area scanned with an AFM. b) A dark field image of the groove made with an 80 nm nanoparticle. Same area scanned with an AFM. Both structures are made at the speed of 5 µm/s and are longer than 10 µm. c) AFM cross sections of the grooves made with gold nanoparticles of different diameters. (Adapted from [145])

In the DFM the gold nanoparticle is observed as a bright scattering object at the end of each nanochannel. The high resolution AFM images of the channel end emphasizes the crucial role of the gold nanoparticle during the milling process (figure 6.15a).

The small width of the channel made by the optically guided gold nanoparticle is connected to the strongly localized heat distribution around it. The laser power of 6 mW corresponds to a power density of around 540 kW/cm^2 in the region 200 nm away from the optical axis. The calculated surface temperature of an 80 nm gold nanoparticle is around 520°C. This temperature is well above the thermal degradation temperature of PVA, which is around 450°C. The simulated heat distribution is shown in figure 6.15b. Similar to the experiments in the previous section, the shape of the groove wall is determined by the flow of the melted polymer from the outer regions of the gold nanoparticle surroundings.

Control experiments are performed with polymer layers not containing gold nanoparticles. No comparable behavior is observed. The absorption of the polymer layer is much lower than the absorption of the gold nanoparticle. A visible change of the polymer by the focused laser beam is only observed at power den-

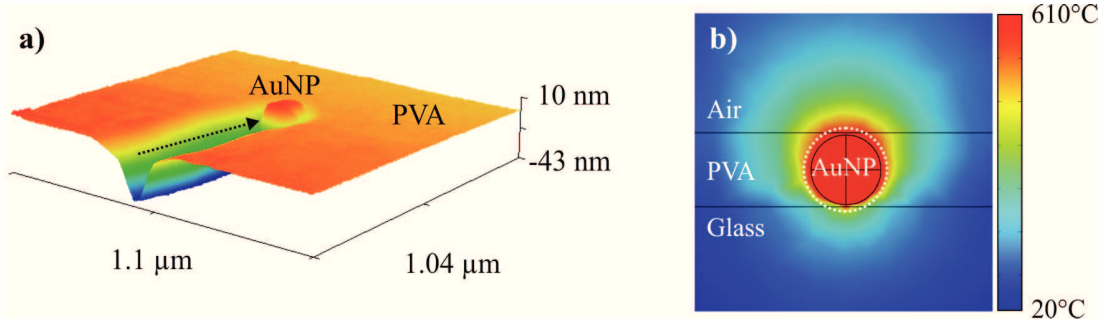

Figure 6.15: **AFM scan of a groove and the simulated heat distribution around the gold nanoparticle.** a) An AFM image of the end of the produced nanochannel. The gold nanoparticle can be found at the end of the structure. The dashed arrow denotes the movement direction. b) Simulated temperature distribution around the gold nanoparticle inside the PVA layer with 80 nm thickness. The corresponding power density is around 540 kW/cm^2. Temperatures above the thermal degradation temperature of PVA are marked with a dashed white circle.

sities which are two orders of magnitude bigger than power densities during the milling experiment. Also the thickness of the structure made by the laser beam is much bigger than the thickness of the groove produced by the nanoparticle.

How the surrounding polymer affects the optical force

During the milling process, the right balance between the radial optical force and the temperature generated by the plasmonic heating is of high importance. If the thermal degradation is reached without applying the required optical force, the nanoparticle will only degrade the surrounding polymer without any movement. According to the theoretical calculation, the repulsive radial force has its maximum in the region 150 to 200 nm below the focal plane and same distance away from the optical axis (see figure 6.10b). In the middle of the spot the radial force is zero, contrary to the surface temperature of the gold nanoparticle, which shows its maximum there. In the ideal case, the thermal degradation of the polymer must start in the region of the maximal repulsive force. According to the calculation, the surface temperature of 450°C (thermal degradation temperature of PVA) is reached at the power density of 480 kW/cm^2. In the region with maximal optical force (200 nm below the focal plane and away from the optical axis), these power density value is provided by a laser beam with 5.5 mW total

power. This calculated laser power is in a good agreement with the experimental laser power between 5 and 10 mW.

Overall, the displacement speed of the gold nanoparticle is determined by the intensity of the laser beam, the effective refractive index of the nanoparticle surroundings, and the thermal degradation rate of the polymer. The laser intensity affects the optical forces acting on the gold nanoparticle and the temperature increase due to plasmonic heating. At the same time, the degrading polymer matrix leads to a change of the effective refractive index, which affects both, the optical force and the plasmonic heating of the gold nanoparticle. If the thermal degradation rate would be faster than the movement of the gold nanoparticle, a polymer-free area would be produced around it. All these factors affect each other, which makes the milling process sensitive to large parameter variations. An example of the parameter variation is shown in the figure 6.16. Here we calculate the radial and the axial components of the total optical force depending on the effective refractive index. This calculation shows how the thermal degradation process leads to a decrease of the effective refractive index and affects the total optical force.

The plot of the total optical force in figure 6.16a shows variations of the axial $\mathbf{F}_z$ and the radial $\mathbf{F}_r$ forces acting on an 80 nm gold nanoparticle surrounded by PVA matrix (n = 1.55 [154]) or surrounded by air (n = 1.0). The axial force magnitude changes by two-fold upon a stepwise change from one surrounding medium to another. The value of this force remains positive as it acts always along the beam propagation direction. The radial component of the optical force becomes zero if the effective refractive index equals 1.1. At this point the radial force changes its direction: in a range between n = 1.0 to 1.1 it acts toward the optical axis ($\mathbf{F}_r$ in figure 6.16b), for n $>$ 1.1 it acts away from the optical axis (see $\mathbf{F}_r$ in figure 6.16c). By comparing these theoretical results, it can be concluded, that the repulsive component of the radial force present in a polymer matrix is not existing if the nanoparticle is surrounded by air. This conclusion is in a good agreement with the experimental results. First, no optically induced movement was observed during control experiments with gold particles on a glass substrate, it is only possible inside a polymer layer. Second, at high laser powers,

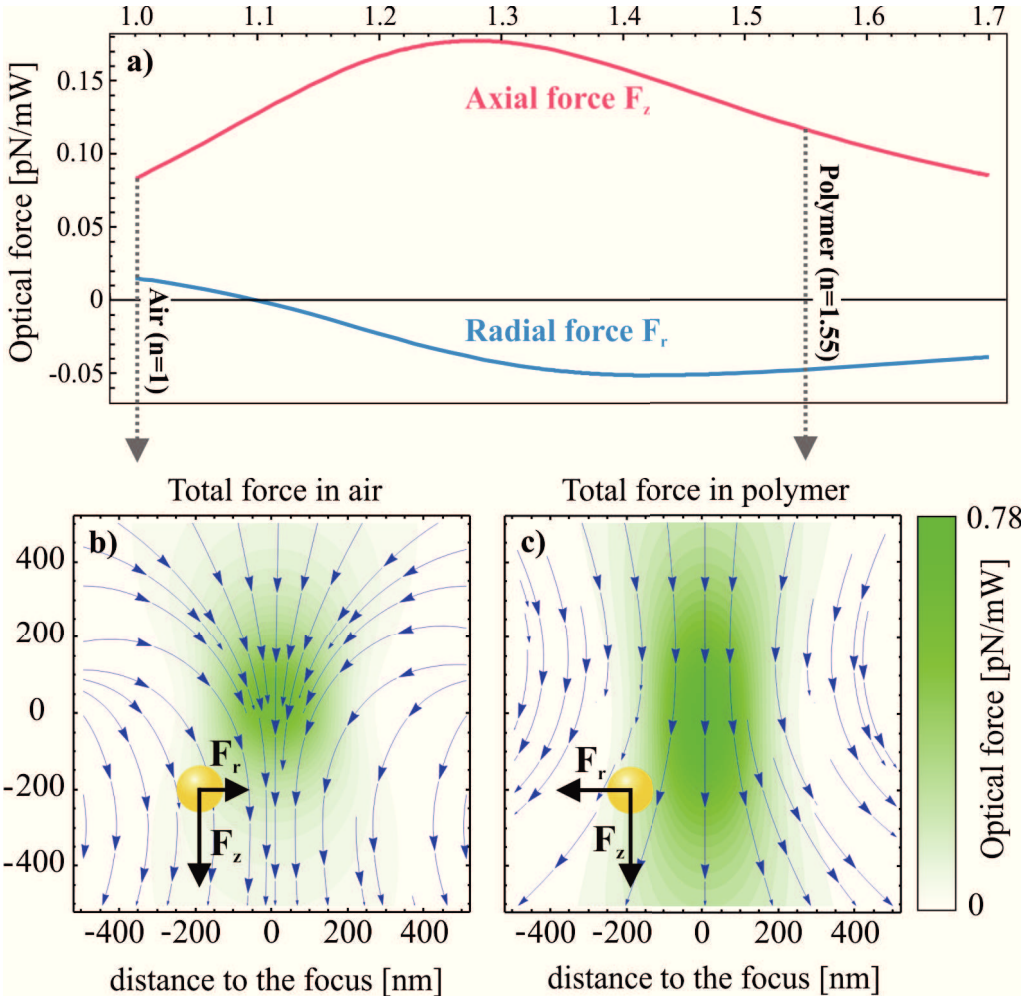

Figure 6.16: **Calculated axial and radial components of the optical force.** a) Optical force on a gold nanoparticle versus the refractive index of the surrounding medium. The nanoparticle is placed 200 nm away from the optical axis and 200 nm below the focal plane. b) and c) Plots of total optical forces for n = 1.00 and 1.55 respectively.

a formation of a polymer free area around the gold nanoparticle prevents it from being guided by the laser beam.

6.1.3 Summary and outlook

The milling process investigated in the previous chapter is based on two effects: the repulsive optical force and efficient plasmonic heating of the gold nanopar-

ticle by the laser beam. Both are directly connected to plasmonic properties of the employed nanostructure. The milling process depends on the direction of the optical force, which pushes the gold nanoparticle away from the optical axis. Figure 6.17 illustrates the region of the repulsive optical force for 80 nm gold nanoparticle as a function of the wavelength and the refractive index of the surrounding medium.

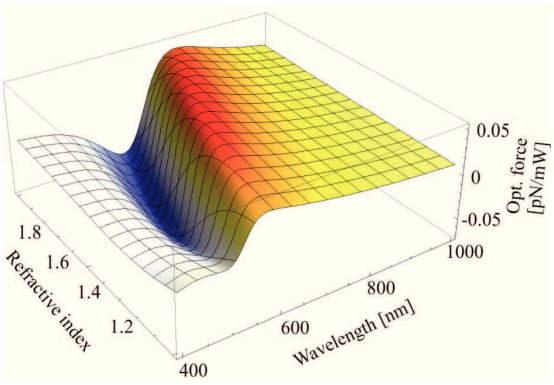

Figure 6.17: **Radial optical force on a gold nanoparticle.** Dependence of the total radial optical force (sum of radial components of the scattering and gradient forces) on the refractive index and applied wavelength. The diameter of the gold nanoparticle is 80 nm, it is placed 200 nm below and 200 nm away from the focal point. In the blue region of the plot, the radial optical force acts away from the optical axis, in the red and yellow regions it acts toward the optical axis.

Both, the radial and axial components of the optical force are affected by the focusing angle of the laser beam. Oil immersed objectives provide an NA up to 1.45, which allows stronger focusing of the laser beam. Figure 6.18 illustrates both components of the optical force for different values of the NA.

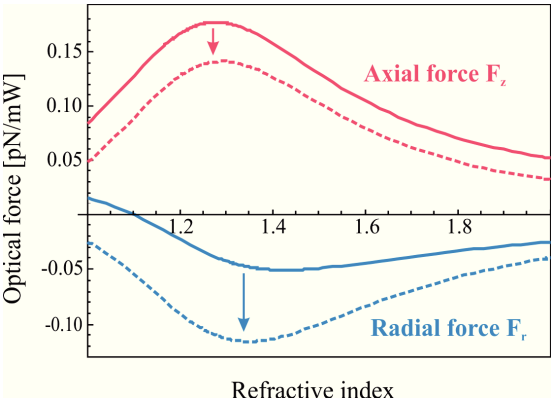

Figure 6.18: **Optical forces on a gold nanoparticle at different focusing angles.** Changing of the NA affects the axial (red curves) and radial (blue curves) optical forces due to changing angle of the focused light. Solid lines correspond to NA = 0.9, dashed to NA = 1.45. The nanoparticle is placed 200 nm below and 200 nm away from the focal point.

An alternative improvement of the milling process can be achieved by changing the beam propagation direction. In our experiment we use radial components of the optical force. These components are usually weaker than the scattering force

along the optical axis. In order to create similar structures the laser beam must propagate parallel to the substrate surface.

6.2 Polymer cross-linking with a gold nanoparticle

The reaction rate of chemical reactions is temperature dependent. This behavior is expressed by the Q10 factor or the rule of van't Hoff [155]. The cross-linking reaction of certain polymers follow this rule [156]. While the cross-linking reaction is slow at room temperature, it can be accelerated significantly by the temperature increase.

Polydimethylsiloxane (PDMS) is a well known thermosetting polymer, which is widely used for scientific applications. In this section we investigate a novel nanofabrication method which uses plasmonically heated gold nanoparticles to accelerate the cross-linking reaction of PDMS components.

6.2.1 PDMS shell cross-linking by plasmonic heating

As shown in the previous section experimentally and theoretically, the heat generated by irradiating gold nanoparticles is highly localized. To prove the concept of using plasmonic heating to accelerate the cross-linking reaction of PDMS, a glass substrate with 82 nm gold nanoparticles is covered with a fluid PDMS precursor.

The laser irradiating experiments are performed using the same DFM as in the previous section. After irradiating gold nanoparticles, the remaining layer of not cross-linked silicone is removed by rinsing the substrate with hexane. Due to the different solubility of the fluid precursor and the cross-linked PDMS, the heat-cured PDMS shell is not dissolved by the solvent.

During the first experiment, the laser beam is focused on a single gold nanoparticle for a fixed time and laser intensity of 3 mW to trigger the cross-linking reaction of PDMS. It is remarkable, that the color of the light scattered by the gold nanoparticle before and after the irradiation process is almost not changing. The corresponding dark field pictures and the collected scattering spectrum are shown in figure 6.20a-c. Due to a small difference between the refractive indexes of the cross-linked PDMS and its surrounding fluid silicone, it is not possible to see the PDMS shell around the irradiated gold nanoparticle with the naked eye. The time frame for mixing the silicone components, performing laser heating ex-

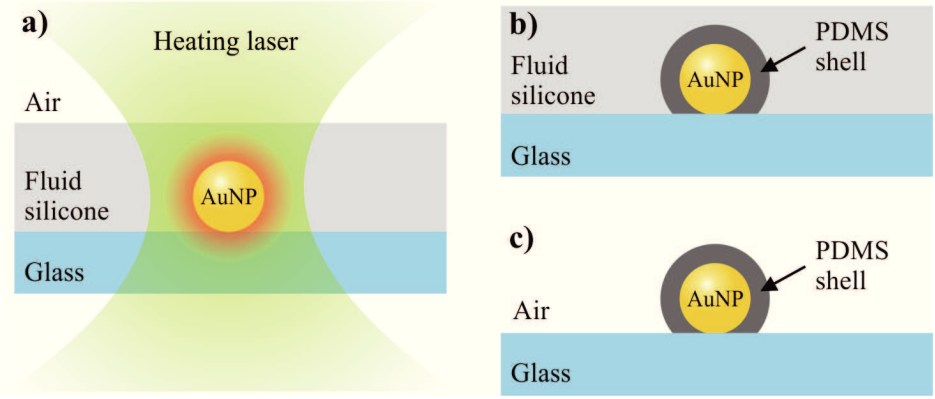

Figure 6.19: **Schematic view of the laser heating experiment.** a) A gold nanoparticle with 80 nm diameter is placed on top of a glass substrate and covered with a fluid PDMS precursor. A focused laser beam with a wavelength of 532 nm is focused on the gold nanoparticle. b) Increased temperature around the gold nanoparticle accelerates the cross-linking reaction of PDMS. c) The fluid, not cross-linked silicone layer is dissolved by hexane.

periments and dissolving the remaining fluid silicone layer is usually kept under 2 hours, as suggested in the literature [101], to avoid PDMS cross-linking at room temperature.

A significant difference between irradiated and not-irradiated nanoparticles is observed after dissolving the fluid silicone layer with hexane. The region around the laser-heated gold nanoparticles appear as a bight white scatterer, which can be explained by a notable difference between the refractive index of the PDMS ($n = 1.43$ [157]) and air ($n = 1$). The result of the experiment is illustrated in figure 6.20d, which shows the same sample area after dissolving the fluid silicone layer.

The amount of the light scattered by the resulting PDMS structure shows a strong dependence on the laser spot overlap with the gold nanoparticle, the laser irradiation time and the laser intensity. In order to reproduce the result, the laser spot is focused as exactly as possible on the gold nanoparticle using a precise stepping motor. Comparable to the heating experiments from the previous section, already a small variation of the laser beam position relative to the gold nanoparticle results in a change of the laser power density due to its Gaussian distribution around the optical axis. Longer irradiation times and higher laser

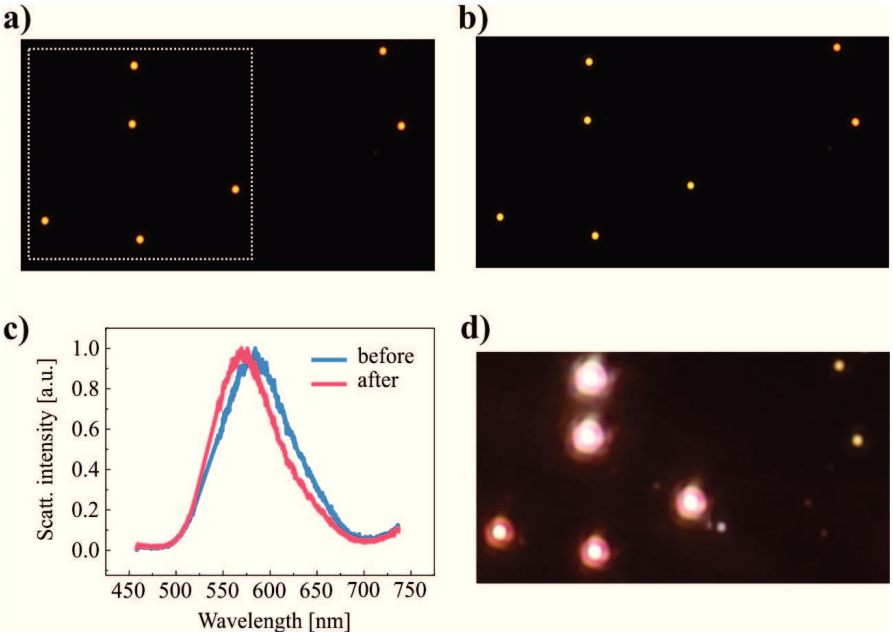

Figure 6.20: **DFM characterization of the laser heating experiment.** a) Gold nanoparticles inside the marked area are irradiated with the laser beam. The two particles on the right side of the image are not irradiated. b) After irradiation, a small change of the scattered light is observed. c) Spectral shift of the scattered light before (blue curve) and after (red curve) laser irradiation. d) The sample region after dissolving the fluid precursor. Big, strongly scattering structures are observed around irradiated gold nanoparticles.

intensities lead to a bigger PDMS shell due to the increased duration of the cross-linking reaction and higher temperatures respectively.

Several series of experiments with varying irradiating times and laser powers are performed in order to study corresponding shell size dependences. Since changing of each of these factors result in a different PDMS shell thickness, it is reasonable to perform independent experiments with a fixed laser power and varying irradiation times and other way around.

Experiments with a constant laser power

The result of the experiment, which is performed with a constant laser power of 2 mW but different irradiation times between 0 and 16 s is illustrated in figure 6.21a. In all SEM images a clear difference between non-irradiated and irra-

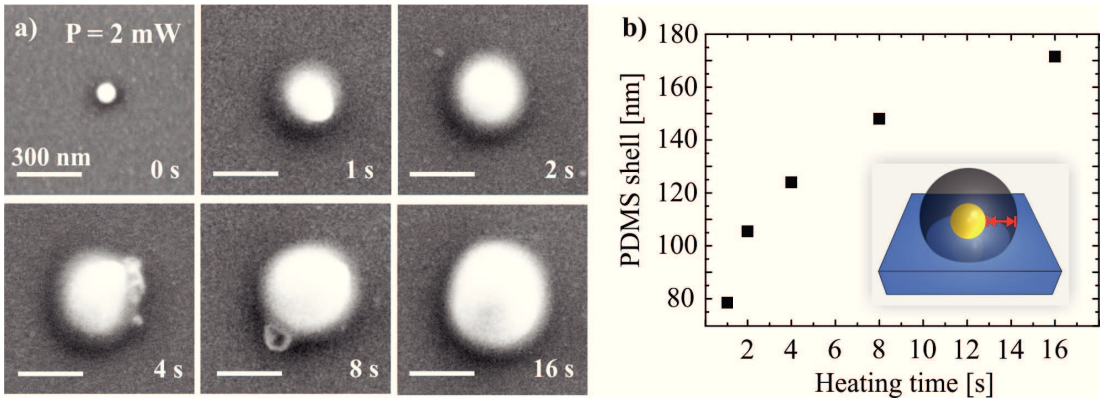

Figure 6.21: **SEM images and characterization of the PDMS shell with constant laser power.** a) SEM images of the produced PDMS shell resulting after different irradiation times between 0 and 16 s. The laser power is held constant during the experiment (2 mW). b) A plot of the resulting PDMS shell thickness versus the irradiation time. The scheme in the low right corner illustrates the shell thickness by a red arrow.

diated nanoparticles is visible. Non-irradiated gold nanoparticles appear as a bright spot with a diameter of around 80 nm. All irradiated gold nanoparticles appear much bigger compared to non-irradiated particles. SEM images show a round shell-like structure at the same position as the previously irradiated gold nanoparticle. The gold nanoparticle itself is not visible due to the polymer layer. The symmetric shape of the shell and its appearance only around laser irradiated gold nanoparticles leads to the assumption, that the shell is produced by the thermally activated cross-linking reaction of PDMS. SEM images allow to measure the size of the resulting structure with a nanoscopic precision. To calculate the shell thickness, the known radius of the gold nanoparticle is subtracted from the radius of the PDMS structure, which is measured by SEM.

The shell thickness is increasing with longer laser irradiation times. It varies between 80 nm for 1 s and 170 nm for 16 s of laser heating, as shown in figure 6.21b. The graph also shows a nonlinear growth of the shell for increasing experimental times. A reasonable explanation of this behavior is provided by a nonlinear decrease of the temperature around a plasmonically heated gold nanoparticle depending on the distance to the nanoparticle surface. In order to understand the growth process of the PDMS shell, temperature distribution around the heated

gold nanoparticle is simulated. The necessary material properties of the fluid silicone are taken from the literature [158, 159].

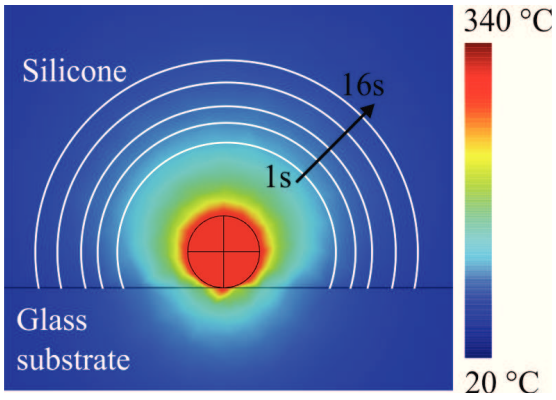

Figure 6.22: **Simulation of the heat distribution around the irradiated gold nanoparticle.** Heat distribution around an 82 nm gold nanoparticle on top of a glass substrate and surrounded by a fluid PDMS precursor. The laser power density is 371 kW/cm^2. White concentric lines denote the resulting PDMS shell after different times.

Figure 6.22a shows the calculated heat distribution. The graph shows the steady state temperature, around an 82 nm gold nanoparticle irradiated with a focused laser beam of 2 mW power and 532 nm wavelength. Time dependent simulations show, that 95% of the steady state temperature is already reached 200 ns after switching the laser on. This time is well below the shortest irradiation time of 1 s. In addition to the temperature distribution, the measured size of the PDSM shell is overlaid in the same graph in order to illustrate the resulting shell after different irradiation times between 1 and 16 s.

Computer based simulations of the heat distribution allow to predict the resulting size of the PDMS shell after different nanoparticle irradiation times. These theoretical calculations are important if the technique is used to manufacture structures with defined sizes and properties. However, the simulation does not take into account some processes, which might occur in a dynamic system around a localized heat source. Firstly, the high temperature of the gold nanoparticle leads to a convectional flow of the fluid silicone around it. This flow can disturb the cross-linking reaction by decreasing the nanoparticle temperature. Secondly, thermal properties of the cross-linked PDMS differ from the fluid silicone, which affects the heat distribution around the gold nanoparticle. Thirdly, material properties, such as heat capacity and thermal conductivity are usually temperature dependent. In case of the PDMS precursor, these values are assumed to

be constant. Implementing these factors into the simulation will lead to a more precise results but would also increase the calculation effort significantly.

Experiments with a constant irradiation time

An additional experiment is performed to investigate the PDMS shell formed for different laser powers while keeping the irradiation time constant. The sample is prepared using the same method as in the previous experiment. A irradiation time of as 8 s is chosen and the laser power is increased from 2.5 mW to 12.5 mW in 2.5 mW steps. Side view SEM images of PDMS structures resulting from different laser powers are shown in figure 6.23a. An additional structure is produced at a relatively high laser power around 20 mW. During the laser irradiation process at this power formation of strongly scattering objects is observed around the gold nanoparticle. Most likely, these scatterers are vapor bubbles, which are formed at high temperatures around the gold nanoparticle and disturb the reproducibility of the formation of PDMS shell. Therefore, only experiments without any bubble formation during the laser irradiation process are evaluated.

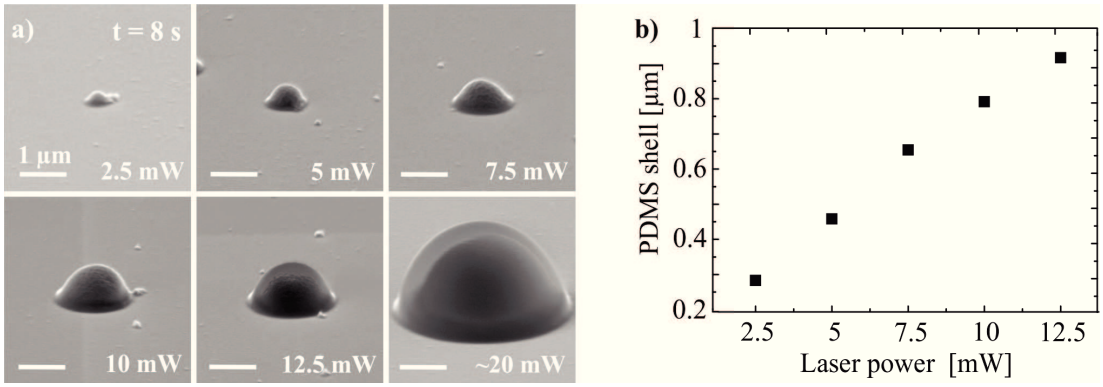

Figure 6.23: **SEM images and characterization of the PDMS shell with varying laser power.** a) Tilted SEM images of the PDMS shell produced by using different laser powers between 2.5 and 12.5 mW. The irradiation time is held constant at 8 s. An additional structure is shown for laser power of 20 mW. This structure is not investigated further due to bubble formation during the heating process. b) The resulting PDMS shell thickness versus the power of the heating laser.

Again, only laser irradiated gold nanoparticles are surrounded by the PDMS shell. Comparable to the previous experiment, the cross-linked structure is located concentric around the gold nanoparticle. By tilting the sample it is possible to obtain a partial side view of the region of interest. SEM images from tilted samples show the regular hemispherical shape of the cross-linked PDMS structure. The height of the structure corresponds approximately to the horizontal radius, which results from the nearly concentric heat distribution around the laser heated gold nanoparticle.

The thickness of the PDMS shell is measured and plotted against the corresponding laser power (figure 6.23b). A linear shell thickness dependence on the laser power, which is observed in the graph, is provided by the linear temperature increase around the gold nanoparticle with an increasing laser power. In order to calculate the corresponding temperature, simulations for different laser intensities are performed. The temperature, at which the shell stops to grow is between 53°C and 55°C for different laser powers. This value is in a good agreement to the temperature corresponding to 8 s irradiation time from the previous experiment of around 52°C.

The calculated temperature of the gold nanoparticle surface varies between 800 and 2000°C for 5 and 12.5 mW laser power respectively. At such high temperatures the inner part of the cross-linked PDMS shell could thermally degrade.

Experiments with low laser intensities

It is important that the nanoparticle temperature is kept below the thermal degradation temperature of PDMS. A laser power of 2 mW in current configuration leads to maximum temperature about 340°C, which is below the thermal degradation temperature of PDMS. To produce a relatively thick PDMS shell of more than 300 nm, it is preferable to increase the irradiation time instead of increasing the power of the heating laser above 2 mW. Due to the previously observed exponential behavior of the polymerization time at constant laser intensity, it will take several minutes to cross-link a polymer shell thicker than 300 nm. This process is limited by the cross-linking reaction at room temperature, which starts about two hours after mixing the PDMS components.

Theoretically, short irradiation times and lower laser intensities should lead to a thin cross-linked layer around a gold nanoparticle. To investigate this behavior, the laser power is decreased to a range between 0.5 to 1 mW. Due to the manual control and mechanical process of the laser shutter the irradiation time is kept above 1 s. Shorter laser times would otherwise decrease the reproducibility of the experiment.

The result of the low laser power experiment is different in comparison to experiments at powers above 2 mW. A small displacement (below 1 µm) of the irradiated gold nanoparticle is observed short time after switching the laser on. The particle movement stops and cannot be detected during the second laser irradiation period. SEM image of the displaced gold nanoparticle shows two different types of elongated structures. In the first case, the structure ends with a PDMS shell (figure 6.23a) which is similar to PDMS shells produced by heating gold nanoparticles with a laser power above 2 mW. At the end of the second type of the elongated structure no comparable polymer shell is visible. The structure ends with the gold nanoparticle (figure 6.23b) which is displaced by the laser beam during the experiment. Both figures show the movement of the gold nanoparticle (marked with a green arrow) with respect to the laser beam (green dashed circle). Despite of the different shape at the end, the width of both elongated structures is around 140 nm.

An obvious explanation for occurrence of different structure types is based on different directions of the total optical force. These force directions are illustrated in figure 6.23c for gold nanoparticles slightly above or below the focal plane. The first structure results if the gold nanoparticle is pulled toward the optical axis by the optical force. The nanoparticle movement stops if the radial component vanishes in the region close to the optical axis. In this region the laser power density is higher compared the regions away from the optical axis. A cross-linked PDMS shell grows around the gold nanoparticle after it stops the movement. The second structure is produced by pushing the gold nanoparticle away from the optical axis by the repulsive optical force as shown in figure 6.23c (the gold nanoparticle is slightly below the focal plane). In this case the gold nanoparticle moves from a region with high power density to a region with low power density. At the end of its movement, the gold nanoparticle is practically pushed out from the laser

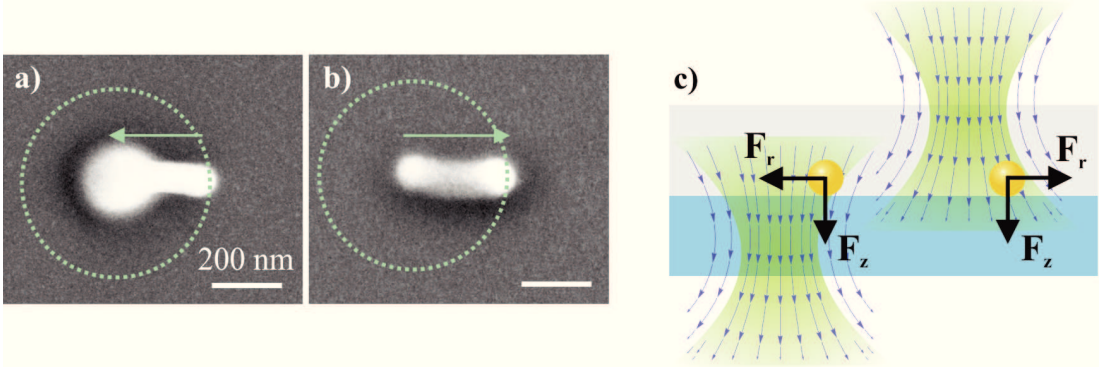

Figure 6.24: **Gold nanoparticle displacement by the laser beam.** a) The gold nanoparticle is pulled by the laser beam toward the optical axis. b) The gold nanoparticle is pushed away from the optical axis. In both images the green dashed circle denotes the laser beam and the green arrow denotes the nanoparticle displacement. c) Optical forces on gold nanoparticles above and below the focal plane. The corresponding radial force F_r acts into different directions.

spot. The temperature of the nanoparticle is decreasing and consequently none or only a thin cross-linked polymer shell is formed around it.

Different conditions and results of the last experiment prove the possibility of applying optical forces in order to displace gold nanoparticles laterally inside the fluid polymer precursor to and use the plasmonic heating, to cross-link the polymer along the nanoparticle displacement. It is reasonable to use the repulsive radial force to create structures longer than laser spot diameter, since structures produced with the attractive optical force are terminated by a growing polymer shell. In the following section we proceed with investigation on the gold nanoparticle displacement inside the fluid polymer by using a focused laser beam.

6.2.2 PDMS nanowire formation

In following experiments we investigate how a resonant laser beam can be applied to guide gold nanoparticles and to trigger the cross-linking reaction by plasmonic heating.

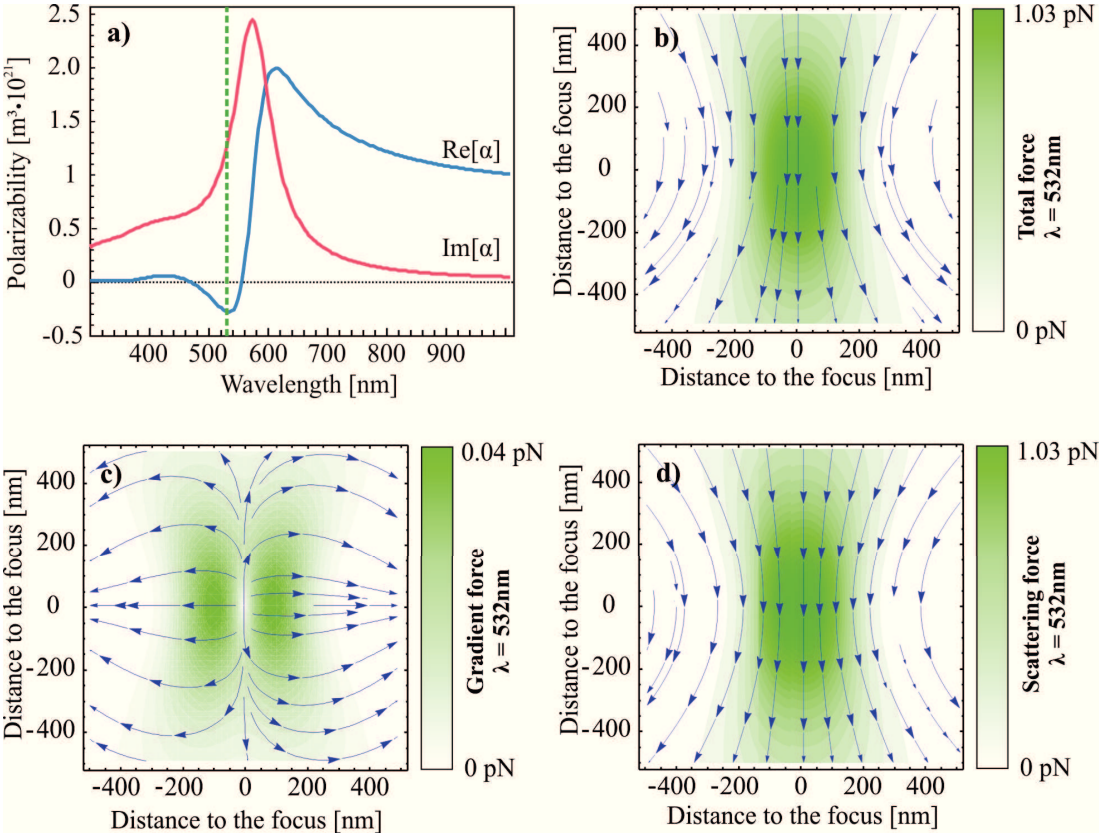

Figure 6.25: **The complex polarizability and optical forces on a 82 nm gold nanoparticle in PDMS.** a) Real and imaginary parts of the polarizability are shown in blue and red respectively. The applied wavelength of 532 nm is denoted by the green dashed line. The total (b), the gradient (c) and the scattering force (d) on the gold nanoparticle, provided by the previously calculated polarizability.

Optical forces and experimental configuration

Optical forces acting on a gold nanoparticle depend on its complex polarizability as explained in the theory chapter (2.3). In order to understand the interaction between the focused laser beam and a gold nanoparticle surrounded by the PDMS precursor, it is important to calculate the polarizability and the resulting optical forces. Figure 6.25a shows the real and the imaginary part of the complex polarizability of a spherical nanoparticle of 82 nm diameter embedded in a medium with a refractive index of 1.43. Additionally, the green dashed line denotes the wavelength of the applied laser beam of 532 nm. The total optical force (figure

6.25b) is divided into the gradient force and the scattering force (figure 6.25c and d respectively). It is important to emphasize the repulsive nature of the gradient force again, which results from the negative value of the real part of the polarizability at 532 nm wavelength.

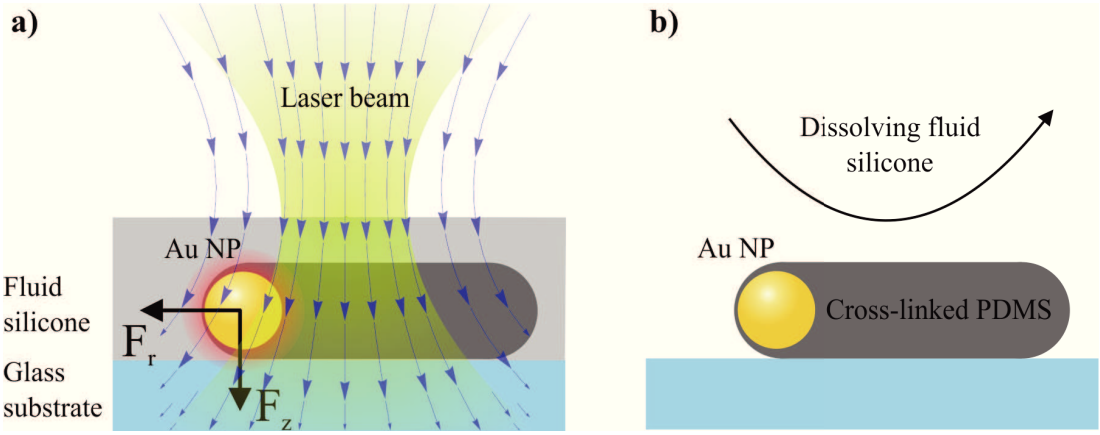

Figure 6.26: **Schematic view of the experimental configuration for nanoparticle displacement.** a) A focused laser beam exerts optical forces (denoted by blue arrows) and heats the gold nanoparticle simultaneously. The cross-linking reaction of PDMS is accelerated by the local heat increase around the nanoparticle. b) A free-standing PDMS structure after dissolving the fluid silicone with hexane.

The experimental configuration is shown in figure 6.26a. The focal plane of laser beam is slightly above the glass surface and the beam is moved toward the gold nanoparticle until the optical force is strong enough to displace the gold nanoparticle. It is remarkable, that it is possible to move gold nanoparticles only at laser intensities below 1 mW. At higher intensities no nanoparticle movement is achieved. Instead, a PDMS shell grows instantly around the gold nanoparticle. The direction of the nanoparticle displacement is controlled by the direction of the approaching laser beam. Similar to other experiments with fluid PDMS precursor, the resulting cross-linked structure is almost not visible until the fluid silicone is dissolved by a solvent. The reason for this is the small difference in refractive indexes between fluid precursor and cross-linked PDMS and big difference between PDMS and air.

PDMS nanowire formation

After removing the fluid PDMS precursor, the resulting cross-linked structure is easily observed by the DFM. The length of the PDMS structure is several microns. The thickness of the resulting structure cannot be resolved by conventional optical microscopy. Each PDMS structure contains the gold nanoparticle, which was guided by the laser beam during the prior experiment. On the dark field images the gold nanoparticle is clearly recognizable by the specific color of the scattered light. Figure 6.27a shows a dark field image of a nanowire produced by an optically driven gold nanoparticle. The length of this specific structure is around 4 µm. The clearly distinguishable gold nanoparticle a the end of the structure is denoted by the white arrow. Typically, it is possible to produce structures with lengths between 1 and 20 µm. The shape of each structure is mainly determined by the moving direction of the laser beam.

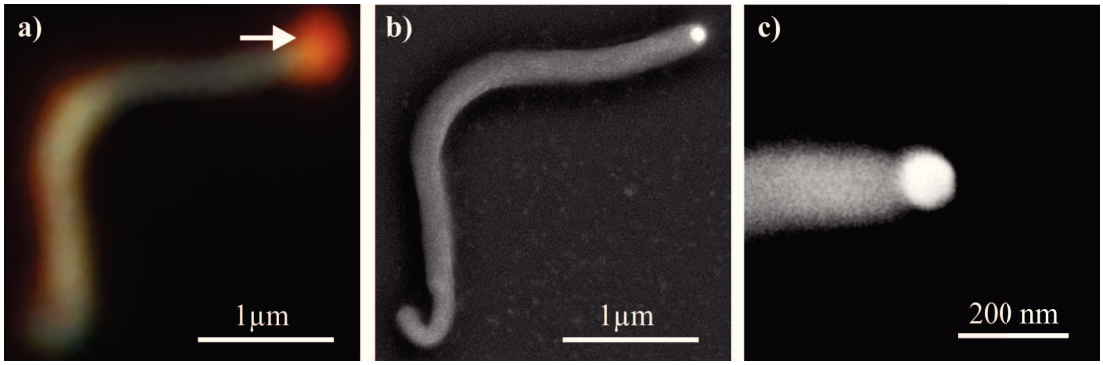

Figure 6.27: **DFM and SEM images of the resulting PDMS structure.** a) DFM image made with 100x magnification. White arrow denotes the gold nanoparticle. b) SEM image of the same PDMS structure. The measured thickness is around 130 nm, the total length is about 4 µm. Again, the gold nanoparticle at the end of the structure is clearly visible. c) A detailed SEM image of the gold nanoparticle at the end of a typical PDMS structure.

To obtain high resolution SEM images of the cross-linked PDMS, the sample is cleaned to remove the immersion oil and a thin layer of carbon of about 5 nm is evaporated on top of it. SEM images allow to measure the exact size of the cross-linked PDMS, which is for this structure around 130 nm (figure 6.27b). Usually, the thickness of cross-linked PDMS is between 120 and 200 nm. A detailed SEM

image of the gold nanoparticle at the end of a typical PDMS structure is shown in figure 6.27c. The contrast in this image is chosen to stress the difference between glass substrate (shown in black), the PDMS structure (shown in gray) and the gold nanoparticle (shown in white). This image stresses the role of the gold nanoparticle as the cross-linking reaction promoter.

A closer look at the high resolution SEM image displaying the gold nanoparticle reveals the possible mechanism of the PDMS cross-linking during the nanoparticle displacement. The gold nanoparticle is inhomogeneously covered by the PDMS layer: the thickness of the PDMS shell toward the moving direction, is much smaller than the thickness on all other sides. This result is explained if the cross-linking reaction starts some time after the temperature increase. The solid cross-linked polymer is formed with a delay behind the gold nanoparticle and cannot hinder the further movement of the nanoparticle. An immediately starting cross-linking reaction would lead to a instantaneously formed PDMS shell with a homogeneous thickness, as observed for laser powers above 2 mW.

Obviously, two factors play an important role during the cross-linking process, the surrounding temperature and the cross-linking delay relative to the moving speed of the gold nanoparticle. The observed speed of the gold nanoparticle is usually on order of 1 µm/s. With this speed it is enough if the cross-linking reaction starts at least 40 ms after the temperature has reached its maximum. Figure 6.28a illustrates the processes of the delayed cross-linking of PDMS schematically. It takes 40 ms for the nanoparticle to pass a distance, which is equal to its radius at 1 µm/s moving speed. Additionally, figure 6.28b shows the simulated temperature profile around the gold nanoparticle with 82 nm diameter placed 200 nm below the focal plane and 200 nm away from the optical axis. The gold nanoparticle is heated by a laser beam with a power of 0.7 mW, which corresponds to a laser power density of around 60 kW/cm^2 at the nanoparticle position.

The simulated temperature of the gold nanoparticle is around 70°C. In previous experiments with a cross-linking PDMS shell, it took 1 s to cross-link PDMS at a comparable temperature of around 79°C. The difference between the laser guiding experiment and heating of static particles is that in the case of moving particles the temperature of the fluid silicone drops to room temperature 200 ns after the heat source leaves the heated volume. In the case of static particles the high

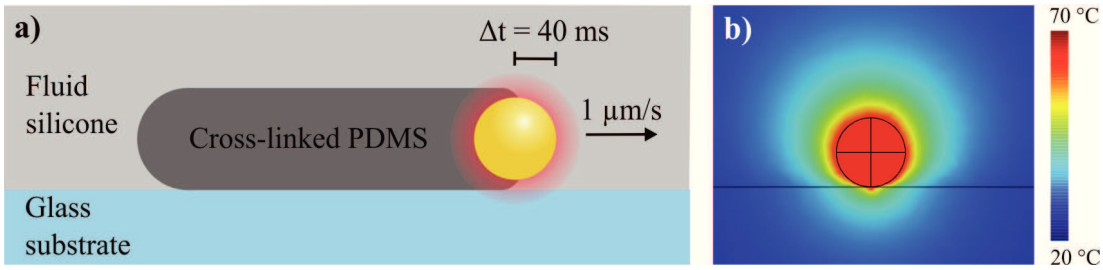

Figure 6.28: **The concept of a delayed cross-inking reaction and the temperature simulation.** a) The cross-linked PDMS shell is formed at least 40 ms after the temperature increase. b) The temperature distribution around an 82 nm gold nanoparticle, irradiated with 60 kW/cm^2.

temperature remains as long as the laser irradiation is switched on. The heat around a moving gold nanoparticle acts as trigger for the cross-linking reaction which takes place shortly after the temperature increase. Particle movement by laser guiding is only observed at laser power below 1 mW. At higher intensities the cross-linking reaction is faster than the nanoparticle displacement and the cross-linked PDMS makes the particle movement impossible. To our knowledge the time delay for cross-linking reaction of PDMS is not studied yet. Future experiments with moving gold nanoparticles using different irradiation intensities could provide more information about the temperature dependent cross-linking kinetics of PDMS on the nanoscale.

Applying circular polarized light

In all nanoparticle heating experiments in this chapter the linear polarization of the laser beam remains unchanged on its way to the sample. Almost all structures made with a linearly polarized laser beam have a relatively straight shape. In order to investigate the shape dependence on the polarization of the applied laser beam, experiments with circular polarized beam are performed.

It is known from the literature that the circular polarized light carries a spin angular momentum, which is provided by the spin of each photon. For paraxial light, the value of the angular spin momentum per photon is $\pm\hbar$ [160]. This spin momentum is transferred to irradiated structures and can be used experimentally to rotate small structures with a circularly polarized light [161, 162]. However,

in the case of a beam focused by a symmetric lens, the direction of the spin is changed as shown in figure 6.29a [163]. It illustrates the change of the initial spin flux density S_0, which is parallel to the optical axis, after a focusing lens. After the lens the resulting spin flux density vector is denoted by S_1, but only the component parallel to the optical axis (denoted by S_z) contributes to the total spin flux of the beam. In order to compensate the reduction of the total spin flux, an orbital angular momentum is introduced into the beam. Due to this consideration, the introduced orbital momentum flux is equal zero on the optical axis, where vector of the spin flux density is unchanged, and increases away from the optical axis, where the angle θ between both components S_z and S_1 is changing.

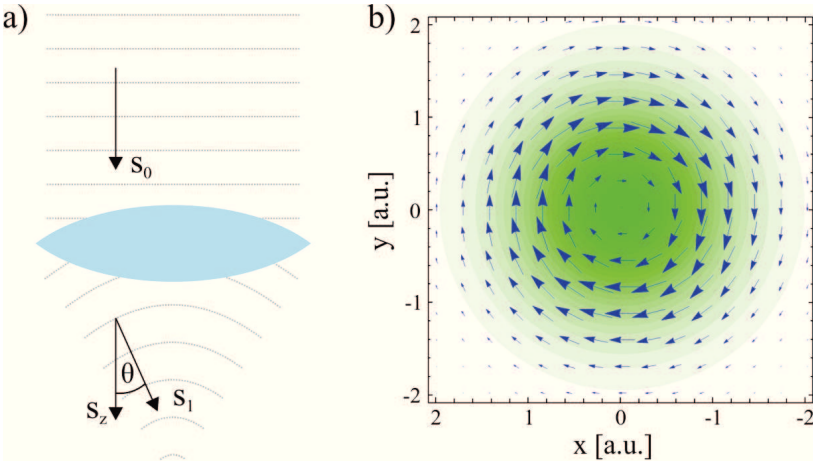

Figure 6.29: **Orbital optical momentum due to the focusing of the beam.** a) A lens changes the direction of the spin flux density by an angle θ in regions away from the optical axis. In order to compensate the reduced spin flux density in z-direction, an additional orbital momentum is introduced (adapted from [163]). b) The calculation of the introduced orbital momentum (blue arrows) of the focused Gaussian beam (green area).

Figure 6.29b shows a plot of the introduced orbital angular momentum (blue arrows), calculated for a Gaussian beam (shown in green) with a convergence angle of 64.16°, for an NA of 0.9. The plot illustrates the orbital nature of the introduced angular momentum which is not connected to the size of the beam, only the divergence angle plays a role. The calculation is based on equations from a theoretical paper [163]. In the case of the optical trap, the nanoparticle is

located close the focus of the laser beam, thus no orbital movement is observed. In our case, no trapping is possible due to the repulsive gradient force. The gold nanoparticle is thus pushed out from the high intensity region of the laser beam.

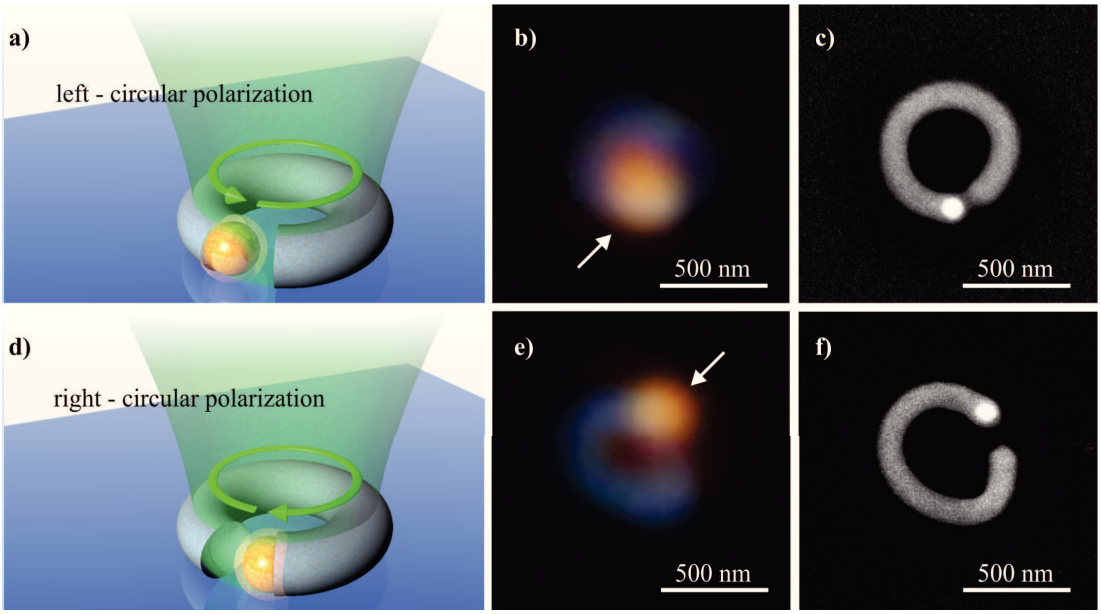

Figure 6.30: **Schematics and results of the experiment with circularly polarized light.** Schematics of the nanowire formation with different directions of the circularly polarized light: left-handed (a) and right-handed (d) polarization. DFM (b) and SEM (c) images of the PDMS wires for left-circular polarized light. DFM (e) and SEM (f) images of the structure produced with right-circular polarized light.

The previous experimental configuration is modified by a $\lambda/4$ wave plate in the laser beam path in order to convert the linear polarization of the beam into the circular polarization. The sample for this experiment is prepared in the same way as for the previous experiment: a glass substrate with gold nanoparticle on it is covered with a layer of fluid PDMS precursor. During the experiment the gold nanoparticle is located in the focus of the circularly polarized laser beam, as shown in figure 6.30a. The dark field image of the resulting PDMS structure is shown in figure 6.30b, where only the gold nanoparticle is clearly visible (marked by the white arrow). Further details of the structure are not resolved by optical microscopy. SEM images of the structure are shown in 6.30c, where the round shape of the cross-linked polymer and the corresponding gold nanoparticle can

be seen. The measured thickness of the cross-linked PDMS is around 120 nm. By changing the handedness of the laser beam polarization from left to right it is possible to change the orbiting direction of the gold nanoparticle. Figure 6.30d shows schematically the experiment with the right circular polarized laser beam. Again, detailed features cannot be resolved by the DFM as shown in figure 6.30e and only on SEM images it is possible to observe the change of the structure handedness 6.30f.

Experiments with different handedness of the circularly polarized laser beam additionally prove the assumption of dominating optical forced during gold nanoparticle displacement. The total diameter of the round PDMS structure correspond to the measured size of the focused laser beam, which has a full width half maximum around of 680 nm.

6.2.3 Summary and outlook

The experiments shown in this chapter prove the possibility of controlled thermal triggering of a chemical reaction around a single gold nanoparticle by means of plasmonic heating. Most experimental principles can be adapted from the previous section of this chapter. Therefore, too strong heating of the gold nanoparticle prevents its displacement due to fast cross-linking of a PDMS shell. A successful nanoparticle displacement is possible by balancing plasmonic heating and optical forces. Additionally, a higher refractive index of the surrounding polymer and a stronger focusing angle of the laser beam might increase the contribution of the radial optical force and improve the quality of the cross-linking process.

An interesting application of this technique can be envisioned by applying three dimensional confinement of spherical gold nanoparticles with a non-resonant laser beam (around 1000 nm wavelength) and extending the method to nanofabrication in three dimensions.

7 Conclusions and outlook

The possibilities of applying plasmonic nanostructures as sensors and triggers for nanoscopic modifications of polymer properties are investigated in this work. Plasmon coupling and refractive index sensitivity are successfully applied to monitor polymer changes in the vicinity of gold nanostructures. Temperature dependent polymer properties, such as shrinking or volume changes can be measured and compared to theoretically predictable plasmon behavior. Furthermore, plasmonic heating and optical manipulation are used to modify polymer properties locally. These experiments demonstrate that optically driven plasmonic nanoparticles are a promising alternative to conventional technology for polymer nanostructuring.

The experiments in the first part of the thesis are based on thermoresponsive behavior of some example polymers, such as thermally induced shrinking of the pre-stressed polystyrene (PS) or volume phase transitions of pNIPAM. In case of shrinking PS, gold nanoparticles are used as nanoscopic markers and rulers on top the polymer surface. Arrays of gold nanoparticles are printed by optical force and transferred to the polymer surface. Plasmonic coupling between these particles can be achieved after the shrinking process of the substrate. This technique can be considered as an alternative preparation method for plasmon coupled nanostructures of arbitrary planar configuration (dimers, tetramers, octamers etc.). The thermoresponsive properties of pNIPAM are investigated with the help of plasmonic properties of gold nanorods. Here, single gold nanorods are incorporated into pNIPAM microgels. The temperature-induced volume phase transition of the microgel is investigated by bulk heating of the microgel-nanorods suspension and by selective plasmonic heating of incorporated gold nanorods with a laser beam. In these experiments the pNIPAM collapse is followed by the plasmon shift of the gold nanorod, which is connected to different refractive indexes

of the swollen and collapsed pNIPAM shell. PNIPAM is known to be useful for biomedical applications, such as targeted drug delivery [164] or as thermally controlled microscopic actuators [165]. The findings of this work suggest that these applications could be expanded to a concept of selective targeting by light. In addition, the fast temperature increase of the microgel due to plasmonic heating of enclosed gold nanostructures, allows to study the kinetics of the microgel collapse.

In the second part, novel concepts of polymer nanostructuring based on plasmonic heating of gold nanoparticles are introduced. First, strong plasmonic heating with temperatures up to 600 °C are used to melt and thermally degrade a polymer film. In combination with optical manipulation, gold nanoparticles act as a tool for controlled polymer nanolithography. Applying the axial component of the optical force, gold nanoparticles can be embossed into the polymer matrix and the generation of a polymer-free area around the nanoparticle can be observed. The radial component of the optical force acts perpendicular to the optical axis and allows to displace plasmonically heated gold nanoparticles by guiding them with a laser beam. Micrometer long grooves which are less than 100 nm wide are produced by this method. The shape of the groove is controlled by the moving direction of the laser beam. Instead of thermal degradation, optothermally manipulated gold nanoparticles can also be used to control cross-linking reactions. At moderate temperatures, the reaction of PDMS is controlled by the amount of heat generated around a laser-irradiated gold nanoparticle. The result is a concentric cross-linked polymer shell with a defined thickness between 80 nm and 1 µm. We investigate the role of laser irradiation time and laser intensity to control the cross-linking process. It is observed that the growing PDMS shell hinders the displacement of the gold nanoparticle by optical forces, which can be avoided by reducing the cross-linking rate at a lower laser intensity. Again, radial components of the optical force can be applied to guide nanoparticles and cross-link the polymer on its way. The resulting structures are several micrometer long and between 120 to 150 nm thick. Both methods presented in this experimental part allow to produce polymer structures with dimensions below the wavelength of the employed laser beam due to the strongly localized heat generation around gold nanoparticles. The size of the resulting structure thereby depends on the

diameter of gold nanoparticles and the heat distribution around them. The applications of this method can vary from micro- and nanofluidics manufacturing, thermally controlled nanofabrication in three dimensions and possible even optical waveguide fabrication.

Bibliography

[1] P. Sciau, *Nanoparticles in ancient materials: the metallic lustre decoration of medieval ceramics*. Chapter, 2012.

[2] P. Colomban, "The use of metal nanoparticles to produce yellow, red and iridescent colour, from bronze age to present times in lustre pottery and glass: solid state chemistry, spectroscopy and nanostructure," *Journal of Nano Research*, vol. 8, p. 109–132, 2009.

[3] M. Faraday, "The bakerian lecture: experimental relations of gold (and other metals) to light," *Philosophical Transactions of the Royal Society of London*, vol. 147, p. 145–181, 1857.

[4] G. Mie, "Beiträge zur optik trüber medien, speziell kolloidaler metallösungen," *Annalen der Physik*, vol. 330, no. 3, p. 377–445, 1908.

[5] F. Kim, S. Connor, H. Song, T. Kuykendall, and P. Yang, "Platonic gold nanocrystals," *Angewandte Chemie*, vol. 116, no. 28, p. 3759–3763, 2004.

[6] C. L. Nehl, H. Liao, and J. H. Hafner, "Optical properties of star-shaped gold nanoparticles," *Nano letters*, vol. 6, no. 4, p. 683–688, 2006.

[7] J. Aizpurua, P. Hanarp, D. S. Sutherland, M. Käll, G. W. Bryant, and F. J. Garcia de Abajo, "Optical properties of gold nanorings," *Physical Review Letters*, vol. 90, no. 5, p. 057401, 2003.

[8] Y.-Y. Yu, S.-S. Chang, C.-L. Lee, and C. C. Wang, "Gold nanorods: electrochemical synthesis and optical properties," *The Journal of Physical Chemistry B*, vol. 101, no. 34, p. 6661–6664, 1997.

[9] M.-C. Daniel and D. Astruc, "Gold nanoparticles: assembly, supramolecular chemistry, quantum-size-related properties, and applications toward biology, catalysis, and nanotechnology," *Chemical Reviews-Columbus*, vol. 104, no. 1, p. 293, 2004.

[10] P. K. Jain, K. S. Lee, I. H. El-Sayed, and M. A. El-Sayed, "Calculated absorption and scattering properties of gold nanoparticles of different size, shape, and composition: applications in biological imaging and biomedicine," *The Journal of Physical Chemistry B*, vol. 110, no. 14, p. 7238–7248, 2006.

[11] S. Eustis and M. A. El-Sayed, "Why gold nanoparticles are more precious than pretty gold: noble metal surface plasmon resonance and its enhancement of the radiative and nonradiative properties of nanocrystals of different shapes," *Chemical Society Reviews*, vol. 35, no. 3, p. 209–217, 2006.

[12] E. N. Economou, "Surface plasmons in thin films," *Physical Review*, vol. 182, no. 2, p. 539, 1969.

[13] H. Raether, "Surface plasmons on smooth and rough surfaces and on gratings," *Springer tracts in modern physics*, vol. 111, 1988.

[14] I. O. Sosa, C. Noguez, and R. G. Barrera, "Optical properties of metal nanoparticles with arbitrary shapes," *The Journal of Physical Chemistry B*, vol. 107, no. 26, p. 6269–6275, 2003.

[15] K. L. Kelly, E. Coronado, L. L. Zhao, and G. C. Schatz, "The optical properties of metal nanoparticles: the influence of size, shape, and dielectric environment," *The Journal of Physical Chemistry B*, vol. 107, no. 3, p. 668–677, 2003.

[16] H. Chen, X. Kou, Z. Yang, W. Ni, and J. Wang, "Shape-and size-dependent refractive index sensitivity of gold nanoparticles," *Langmuir*, vol. 24, no. 10, p. 5233–5237, 2008.

[17] M. M. Miller and A. A. Lazarides, "Sensitivity of metal nanoparticle surface plasmon resonance to the dielectric environment," *The Journal of Physical Chemistry B*, vol. 109, no. 46, p. 21556–21565, 2005.

[18] J. N. Anker, W. P. Hall, O. Lyandres, N. C. Shah, J. Zhao, and R. P. Van Duyne, "Biosensing with plasmonic nanosensors," *Nature materials*, vol. 7, no. 6, p. 442–453, 2008.

[19] B. J. Messinger, K. U. Von Raben, R. K. Chang, and P. W. Barber, "Local fields at the surface of noble-metal microspheres," *Physical Review B*, vol. 24, no. 2, p. 649, 1981.

[20] K. B. Crozier, A. Sundaramurthy, G. S. Kino, and C. F. Quate, "Optical antennas: Resonators for local field enhancement," *Journal of Applied Physics*, vol. 94, no. 7, p. 4632–4642, 2003.

[21] J. J. Mock, D. R. Smith, and S. Schultz, "Local refractive index dependence of plasmon resonance spectra from individual nanoparticles," *Nano Letters*, vol. 3, no. 4, p. 485–491, 2003.

[22] G. Raschke, S. Kowarik, T. Franzl, C. Sönnichsen, T. A. Klar, J. Feldmann, A. Nichtl, and K. Kürzinger, "Biomolecular recognition based on single gold nanoparticle light scattering," *Nano letters*, vol. 3, no. 7, p. 935–938, 2003.

[23] Y. C. Cao, R. Jin, and C. A. Mirkin, "Nanoparticles with raman spectroscopic fingerprints for DNA and RNA detection," *Science*, vol. 297, no. 5586, p. 1536–1540, 2002.

[24] K. Kneipp, A. S. Haka, H. Kneipp, K. Badizadegan, N. Yoshizawa, C. Boone, K. E. Shafer-Peltier, J. T. Motz, R. R. Dasari, and M. S. Feld, "Surface-enhanced raman spectroscopy in single living cells using gold nanoparticles," *Applied Spectroscopy*, vol. 56, no. 2, p. 150–154, 2002.

[25] H. H. Richardson, Z. N. Hickman, A. O. Govorov, A. C. Thomas, W. Zhang, and M. E. Kordesch, "Thermooptical properties of gold nanoparticles embedded in ice: characterization of heat generation and melting," *Nano letters*, vol. 6, no. 4, p. 783–788, 2006.

[26] A. O. Govorov, W. Zhang, T. Skeini, H. Richardson, J. Lee, and N. A. Kotov, "Gold nanoparticle ensembles as heaters and actuators: melting and collective plasmon resonances," *Nanoscale Research Letters*, vol. 1, no. 1, p. 84–90, 2006.

[27] J. Stehr, C. Hrelescu, R. A. Sperling, G. Raschke, M. Wunderlich, A. Nichtl, D. Heindl, K. Kurzinger, W. J. Parak, T. A. Klar, and J. Feldmann, "Gold NanoStoves for microsecond DNA melting analysis," *Nano Letters*, vol. 8, pp. 619–623, Feb. 2008.

[28] V. Kotaidis, C. Dahmen, G. Von Plessen, F. Springer, and A. Plech, "Excitation of nanoscale vapor bubbles at the surface of gold nanoparticles in water," *The Journal of chemical physics*, vol. 124, p. 184702, 2006.

[29] T. B. Huff, L. Tong, Y. Zhao, M. N. Hansen, J.-X. Cheng, and A. Wei, "Hyperthermic effects of gold nanorods on tumor cells," *Nanomedicine*, vol. 2, no. 1, p. 125–132, 2007.

[30] X. Huang, P. K. Jain, I. H. El-Sayed, and M. A. El-Sayed, "Plasmonic photothermal therapy (PPTT) using gold nanoparticles," *Lasers in medical science*, vol. 23, no. 3, p. 217–228, 2008.

[31] X. Huang, P. K. Jain, I. H. El-Sayed, and M. A. El-Sayed, "Gold nanoparticles: interesting optical properties and recent applications in cancer diagnostics and therapy," *Nanomedicine*, vol. 2, no. 5, p. 681–693, 2007.

[32] S. Nedev, A. S. Urban, A. A. Lutich, and J. Feldmann, "Optical force stamping lithography," *Nano Letters*, vol. 11, pp. 5066–5070, Nov. 2011.

[33] A. S. Urban, A. A. Lutich, F. D. Stefani, and J. Feldmann, "Laser printing single gold nanoparticles," *Nano letters*, vol. 10, no. 12, p. 4794–4798, 2010.

[34] A. S. Urban, T. Pfeiffer, M. Fedoruk, A. A. Lutich, and J. Feldmann, "Single-step injection of gold nanoparticles through phospholipid membranes," *ACS nano*, vol. 5, no. 5, p. 3585–3590, 2011.

[35] M. Ploschner, T. Čižmár, M. Mazilu, A. Di Falco, and K. Dholakia, "Bidirectional optical sorting of gold nanoparticles," *Nano Letters*, vol. 12, pp. 1923–1927, Apr. 2012.

[36] C. Paquet and E. Kumacheva, "Nanostructured polymers for photonics," *Materials Today*, vol. 11, no. 4, p. 48–56, 2008.

[37] Y. Lu and S. C. Chen, "Micro and nano-fabrication of biodegradable polymers for drug delivery," *Advanced drug delivery reviews*, vol. 56, no. 11, p. 1621–1633, 2004.

[38] A. C. Mayer, S. R. Scully, B. E. Hardin, M. W. Rowell, and M. D. McGehee, "Polymer-based solar cells," *Materials today*, vol. 10, no. 11, p. 28–33, 2007.

[39] R. Riehn, A. Charas, J. Morgado, and F. Cacialli, "Near-field optical lithography of a conjugated polymer," *Applied physics letters*, vol. 82, no. 4, p. 526–528, 2003.

[40] A. C. Balazs, T. Emrick, and T. P. Russell, "Nanoparticle polymer composites: where two small worlds meet," *Science*, vol. 314, no. 5802, p. 1107–1110, 2006.

[41] S. A. Maier, *Plasmonics: fundamentals and applications*. Springer Science+ Business Media, 2007.

[42] U. Kreibig and M. Vollmer, *Optical properties of metal clusters*. Springer-Verlag, 1995.

[43] L. Novotny, *Principles of Nano-Optics*. Cambridge University Press, June 2006.

[44] J. D. Jackson, "Classical electrodynamics, 3rd ed.," *American Journal of Physics*, vol. 67, p. 841, Sept. 1999.

[45] P. B. Johnson and R. W. Christy, "Optical constants of the noble metals," *Physical Review B*, vol. 6, no. 12, p. 4370, 1972.

[46] S. Kühn, U. H\aakanson, L. Rogobete, and V. Sandoghdar, "Enhancement of single-molecule fluorescence using a gold nanoparticle as an optical nanoantenna," *Physical review letters*, vol. 97, no. 1, p. 017402, 2006.

[47] V. Myroshnychenko, J. Rodríguez-Fernández, I. Pastoriza-Santos, A. M. Funston, C. Novo, P. Mulvaney, L. M. Liz-Marzán, and F. J. G. de Abajo, "Modelling the optical response of gold nanoparticles," *Chemical Society Reviews*, vol. 37, no. 9, p. 1792–1805, 2008.

[48] H. Kuwata, H. Tamaru, K. Esumi, and K. Miyano, "Resonant light scattering from metal nanoparticles: Practical analysis beyond rayleigh approximation," *Applied physics letters*, vol. 83, no. 22, p. 4625–4627, 2003.

[49] J. P. Wilcoxon, J. E. Martin, F. Parsapour, B. Wiedenman, and D. F. Kelley, "Photoluminescence from nanosize gold clusters," *The Journal of chemical physics*, vol. 108, p. 9137, 1998.

[50] A. O. Govorov and H. H. Richardson, "Generating heat with metal nanoparticles," *Nano Today*, vol. 2, no. 1, p. 30–38, 2007.

[51] M. Quinten, "MQMIE version 3.2a," 2012.

[52] J. N. Reddy and D. K. Gartling, *The Finite Element Method in Heat Transfer and Fluid Dynamics*. CRC Press, 2010.

[53] A. Ashkin and J. M. Dziedzic, "Optical trapping and manipulation of viruses and bacteria," *Science*, vol. 235, pp. 1517–1520, Mar. 1987.

[54] J. E. Molloy and M. J. Padgett, "Lights, action: optical tweezers," *Contemporary Physics*, vol. 43, no. 4, p. 241–258, 2002.

[55] N. Malagnino, G. Pesce, A. Sasso, and E. Arimondo, "Measurements of trapping efficiency and stiffness in optical tweezers," *Optics Communications*, vol. 214, pp. 15–24, Dec. 2002.

[56] M. Dienerowitz, M. Mazilu, P. J. Reece, T. F. Krauss, and K. Dholakia, "Optical vortex trap for resonant confinement of metal nanoparticles," *Optics Express*, vol. 16, no. 7, p. 4991–4999, 2008.

[57] R. Loudon and S. M. Barnett, "Theory of the radiation pressure on dielectric slabs, prisms and single surfaces," *Optics Express*, vol. 14, no. 24, p. 11855, 2006.

[58] K. Svoboda and S. M. Block, "Optical trapping of metallic rayleigh particles," *Optics Letters*, vol. 19, no. 13, p. 930–932, 1994.

[59] N. R. Heckenberg, R. McDuff, C. P. Smith, H. Rubinsztein-Dunlop, and M. J. Wegener, "Laser beams with phase singularities," *Optical and quantum electronics*, vol. 24, no. 9, p. S951–S962, 1992.

[60] T. Kuga, Y. Torii, N. Shiokawa, T. Hirano, Y. Shimizu, and H. Sasada, "Novel optical trap of atoms with a doughnut beam," *Physical Review Letters*, vol. 78, pp. 4713–4716, June 1997.

[61] I. Manek, Y. B. Ovchinnikov, and R. Grimm, "Generation of a hollow laser beam for atom trapping using an axicon," *Optics communications*, vol. 147, no. 1-3, p. 67–70, 1998.

[62] R. R. Agayan, F. Gittes, R. Kopelman, and C. F. Schmidt, "Optical trapping near resonance absorption," *Applied Optics*, vol. 41, pp. 2318–2327, Apr. 2002.

[63] Z. L. Horváth and Z. Bor, "Focusing of truncated gaussian beams," *Optics communications*, vol. 222, no. 1, p. 51–68, 2003.

[64] M. Heckele and W. K. Schomburg, "Review on micro molding of thermoplastic polymers," *Journal of Micromechanics and Microengineering*, vol. 14, p. R1, Mar. 2004.

[65] C. G. Seefried, J. V. Koleske, and F. E. Critchfield, "Thermoplastic urethane elastomers. i. effects of soft-segment variations," *Journal of Applied Polymer Science*, vol. 19, no. 9, p. 2493–2502, 1975.

[66] A. Yousefi, P. G. Lafleur, and R. Gauvin, "Kinetic studies of thermoset cure reactions: A review," *Polymer Composites*, vol. 18, no. 2, p. 157–168, 1997.

[67] H. Senff and W. Richtering, "Temperature sensitive microgel suspensions: Colloidal phase behavior and rheology of soft spheres," *The Journal of chemical physics*, vol. 111, p. 1705, 1999.

[68] C.-S. Chen, D. N. Breslauer, J. I. Luna, A. Grimes, W.-c. Chin, L. P. Lee, and M. Khine, "Shrinky-dink microfluidics: 3D polystyrene chips," *Lab on a Chip*, vol. 8, no. 4, p. 622, 2008.

[69] C. L. Beyler and M. M. Hirschler, "Sfpe handbook of fire protection engineering," *National Fire Protection Association*, 1995.

[70] C. Buckley and D. Jones, "Glass-rubber constitutive model for amorphous polymers near the glass transition," *Polymer*, vol. 36, no. 17, pp. 3301–3312, 1995.

[71] K. Dalnoki-Veress, J. A. Forrest, C. Murray, C. Gigault, and J. R. Dutcher, "Molecular weight dependence of reductions in the glass transition temperature of thin, freely standing polymer films," *Physical Review E*, vol. 63, p. 031801, Feb. 2001.

[72] J. L. Keddie, R. a. L. Jones, and R. A. Cory, "Size-dependent depression of the glass transition temperature in polymer films," *EPL (Europhysics Letters)*, vol. 27, p. 59, July 1994.

[73] C. T. Moynihan, A. J. Easteal, J. Wilder, and J. Tucker, "Dependence of the glass transition temperature on heating and cooling rate," *The Journal of Physical Chemistry*, vol. 78, pp. 2673–2677, Dec. 1974.

[74] P. J. Lemstra, T. Kooistra, and G. Challa, "Melting behavior of isotactic polystyrene," *Journal of Polymer Science Part A-2: Polymer Physics*, vol. 10, no. 5, p. 823–833, 1972.

[75] K. Mezghani, "Crystallization polymer physical characteristics," 2005.

[76] T. Faravelli, M. Pinciroli, F. Pisano, G. Bozzano, M. Dente, and E. Ranzi, "Thermal degradation of polystyrene," *Journal of analytical and applied pyrolysis*, vol. 60, no. 1, p. 103–121, 2001.

[77] Y. Ono and T. Shikata, "Hydration and dynamic behavior of poly(n-isopropylacrylamide)s in aqueous solution: A sharp phase transition at the lower critical solution temperature," *Journal of the American Chemical Society*, vol. 128, pp. 10030–10031, Aug. 2006.

[78] S. Zhou and B. Chu, "Synthesis and volume phase transition of poly(methacrylic acid-co-n-isopropylacrylamide) microgel particles in water," *The Journal of Physical Chemistry B*, vol. 102, pp. 1364–1371, Feb. 1998.

[79] B. W. Garner, T. Cai, S. Ghosh, Z. Hu, and A. Neogi, "Refractive index change due to volume-phase transition in polyacrylamide gel nanospheres for optoelectronics and bio-photonics," *Applied Physics Express*, vol. 2, p. 057001, Apr. 2009.

[80] A. Grimes, D. N. Breslauer, M. Long, J. Pegan, L. P. Lee, and M. Khine, "Shrinky-dink microfluidics: rapid generation of deep and rounded patterns," *Lab on a Chip*, vol. 8, no. 1, p. 170, 2008.

[81] G. B. DeMaggio, W. E. Frieze, D. W. Gidley, M. Zhu, H. A. Hristov, and A. F. Yee, "Interface and surface effects on the glass transition in thin polystyrene films," *Physical Review Letters*, vol. 78, pp. 1524–1527, Feb. 1997.

[82] H.-L. Zhang, D. G. Bucknall, and A. Dupuis, "Uniform nanoscopic polystyrene patterns produced from a microscopic mold," *Nano Letters*, vol. 4, pp. 1513–1519, Aug. 2004.

[83] S. Fujishige, K. Kubota, and I. Ando, "Phase transition of aqueous solutions of poly (n-isopropylacrylamide) and poly (n-isopropylmethacrylamide)," *The Journal of Physical Chemistry*, vol. 93, no. 8, p. 3311–3313, 1989.

[84] R. Contreras-Cáceres, A. Sánchez-Iglesias, M. Karg, I. Pastoriza-Santos, J. Pérez-Juste, J. Pacifico, T. Hellweg, A. Fernández-Barbero, and L. M. Liz-Marzán, "Encapsulation and growth of gold nanoparticles in thermoresponsive microgels," *Advanced Materials*, vol. 20, no. 9, p. 1666–1670, 2008.

[85] M. Karg and T. Hellweg, "New "smart" poly(NIPAM) microgels and nanoparticle microgel hybrids: Properties and advances in characterisation," *Current Opinion in Colloid & Interface Science*, vol. 14, pp. 438–450, Dec. 2009.

[86] I. Varga, T. Gilányi, R. Mészáros, G. Filipcsei, and M. Zrínyi, "Effect of cross-link density on the internal structure of poly(n-isopropylacrylamide) microgels," *The Journal of Physical Chemistry B*, vol. 105, pp. 9071–9076, Sept. 2001.

[87] S. Höfl, L. Zitzler, T. Hellweg, S. Herminghaus, and F. Mugele, "Volume phase transition of "smart" microgels in bulk solution and adsorbed at an interface: A combined AFM, dynamic light, and small angle neutron scattering study," *Polymer*, vol. 48, pp. 245–254, Jan. 2007.

[88] T. Tanaka, "Kinetics of phase transition in polymer gels," *Physica A: Statistical Mechanics and its Applications*, vol. 140, pp. 261–268, Dec. 1986.

[89] C. E. Reese, A. V. Mikhonin, M. Kamenjicki, A. Tikhonov, and S. A. Asher, "Nanogel nanosecond photonic crystal optical switching," *Journal of the American Chemical Society*, vol. 126, pp. 1493–1496, Feb. 2004.

[90] P. Alexy, D. Bakoš, G. Crkoňová, Z. Kramárová, J. Hoffmann, M. Julinová, E. Chiellini, and P. Cinelli, "Poly(vinyl alcohol)–collagen hydrolysate thermoplastic blends: II. water penetration and biodegradability of melt extruded films," *Polymer Testing*, vol. 22, pp. 811–818, Oct. 2003.

[91] K. Ogura, T. Saino, M. Nakayama, and H. Shiigi, "The humidity dependence of the electrical conductivity of a solublepolyaniline–poly (vinyl alcohol) composite film," *J. Mater. Chem.*, vol. 7, no. 12, p. 2363–2366, 1997.

[92] M.-R. Yang and K.-S. Chen, "Humidity sensors using polyvinyl alcohol mixed with electrolytes," *Sensors and Actuators B: Chemical*, vol. 49, pp. 240–247, July 1998.

[93] Z. H. Mbhele, M. G. Salemane, C. Van Sittert, J. M. Nedeljkovic, V. Djokovic, and A. S. Luyt, "Fabrication and characterization of silver-polyvinyl alcohol nanocomposites," *Chemistry of Materials*, vol. 15, no. 26, p. 5019–5024, 2003.

[94] R. K. Tubbs, "Melting point and heat of fusion of poly (vinyl alcohol)," *Journal of Polymer Science Part A: General Papers*, vol. 3, no. 12, p. 4181–4189, 1965.

[95] Z. Peng and L. X. Kong, "A thermal degradation mechanism of polyvinyl alcohol/silica nanocomposites," *Polymer Degradation and Stability*, vol. 92, pp. 1061–1071, June 2007.

[96] P. S. Thomas, J.-P. Guerbois, G. F. Russell, and B. J. Briscoe, "FTIR study of the thermal degradation of poly (vinyl alcohol)," *Journal of thermal analysis and calorimetry*, vol. 64, no. 2, p. 501–508, 2001.

[97] J. D. Peterson, S. Vyazovkin, and C. A. Wight, "Kinetics of the thermal and thermo-oxidative degradation of polystyrene, polyethylene and poly (propylene)," *Macromolecular Chemistry And Physics*, vol. 202, no. 6, p. 775–784, 2001.

[98] G. M. Whitesides, E. Ostuni, S. Takayama, X. Jiang, and D. E. Ingber, "Soft lithography in biology and biochemistry," *Annual review of biomedical engineering*, vol. 3, no. 1, p. 335–373, 2001.

[99] J. R. Anderson, D. T. Chiu, R. J. Jackman, O. Cherniavskaya, J. C. McDonald, H. Wu, S. H. Whitesides, and G. M. Whitesides, "Fabrication of topologically complex three-dimensional microfluidic systems in PDMS by rapid prototyping," *Analytical Chemistry*, vol. 72, no. 14, p. 3158–3164, 2000.

[100] S. Bhattacharya, A. Datta, J. M. Berg, and S. Gangopadhyay, "Studies on surface wettability of poly (dimethyl) siloxane (PDMS) and glass under oxygen-plasma treatment and correlation with bond strength," *Microelectromechanical Systems, Journal of*, vol. 14, no. 3, p. 590–597, 2005.

[101] D. Corning®, "Product information sheet of sylgard 184," 2007.

[102] S.-H. Choi, J.-H. Kim, and S.-B. Lee, "Sorption and permeation behaviors of a series of olefins and nitrogen through PDMS membranes," *Journal of Membrane Science*, vol. 299, pp. 54–62, Aug. 2007.

[103] G. Camino, S. M. Lomakin, and M. Lazzari, "Polydimethylsiloxane thermal degradation part 1. kinetic aspects," *Polymer*, vol. 42, no. 6, p. 2395–2402, 2001.

[104] C. Sönnichsen, T. Franzl, T. Wilk, G. von Plessen, J. Feldmann, O. Wilson, and P. Mulvaney, "Drastic reduction of plasmon damping in gold nanorods," *Physical Review Letters*, vol. 88, no. 7, p. 077402, 2002.

[105] G. Binnig, C. F. Quate, and C. Gerber, "Atomic force microscope," *Physical Review Letters*, vol. 56, pp. 930–933, Mar. 1986.

[106] C. Odin, J. Aimé, Z. El Kaakour, and T. Bouhacina, "Tip's finite size effects on atomic force microscopy in the contact mode: simple geometrical considerations for rapid estimation of apex radius and tip angle based on the study of polystyrene latex balls," *Surface Science*, vol. 317, pp. 321–340, Oct. 1994.

[107] Y. Martin, C. C. Williams, and H. K. Wickramasinghe, "Atomic force microscope–force mapping and profiling on a sub 100-\AA scale," *Journal of Applied Physics*, vol. 61, no. 10, p. 4723–4729, 1987.

[108] Q. Zhong, D. Inniss, K. Kjoller, and V. Elings, "Fractured polymer/silica fiber surface studied by tapping mode atomic force microscopy," *Surface Science Letters*, vol. 290, pp. L688–L692, June 1993.

[109] R. Garcia and R. Pérez, "Dynamic atomic force microscopy methods," *Surface Science Reports*, vol. 47, pp. 197–301, Sept. 2002.

[110] M.-P. Mingeot-Leclercq, M. Deleu, R. Brasseur, and Y. F. Dufrêne, "Atomic force microscopy of supported lipid bilayers," *Nature protocols*, vol. 3, no. 10, p. 1654–1659, 2008.

[111] R. Pecora, *Dynamic Light Scattering: Applications of Photon Correlation Spectroscopy*. Springer, May 1985.

[112] K.-H. Su, Q.-H. Wei, X. Zhang, J. J. Mock, D. R. Smith, and S. Schultz, "Interparticle coupling effects on plasmon resonances of nanogold particles," *Nano Letters*, vol. 3, pp. 1087–1090, Aug. 2003.

[113] W. Rechberger, A. Hohenau, A. Leitner, J. Krenn, B. Lamprecht, and F. Aussenegg, "Optical properties of two interacting gold nanoparticles," *Optics Communications*, vol. 220, pp. 137–141, May 2003.

[114] J. I. L. Chen, Y. Chen, and D. S. Ginger, "Plasmonic nanoparticle dimers for optical sensing of DNA in complex media," *Journal of the American Chemical Society*, vol. 132, pp. 9600–9601, July 2010.

[115] A. Bek, R. Jansen, M. Ringler, S. Mayilo, T. A. Klar, and J. Feldmann, "Fluorescence enhancement in hot spots of AFM-Designed gold nanoparticle sandwiches," *Nano Letters*, vol. 8, pp. 485–490, Feb. 2008.

[116] S. K. Ghosh and T. Pal, "Interparticle coupling effect on the surface plasmon resonance of gold nanoparticles: from theory to applications," *Chemical Reviews-Columbus*, vol. 107, no. 11, p. 4797–4862, 2007.

[117] A. S. Urban, M. Fedoruk, S. Nedev, A. Lutich, T. Lohmueller, and J. Feldmann, "Shrink-to-fit plasmonic nanostructures," *Advanced Optical Materials*, vol. 1, no. 2, p. 123–127, 2013.

[118] A. Ohlinger, S. Nedev, A. A. Lutich, and J. Feldmann, "Optothermal escape of plasmonically coupled silver nanoparticles from a three-dimensional optical trap," *Nano letters*, vol. 11, no. 4, p. 1770–1774, 2011.

[119] D. Nguyen, D. Taylor, K. Qian, N. Norouzi, J. Rasmussen, S. Botzet, M. Lehmann, K. Halverson, and M. Khine, "Better shrinkage than shrinky-dinks," *Lab on a Chip*, vol. 10, no. 12, p. 1623, 2010.

[120] R. H. Pelton and P. Chibante, "Preparation of aqueous latices with< i> n</i>-isopropylacrylamide," *Colloids and Surfaces*, vol. 20, no. 3, p. 247–256, 1986.

[121] L. Dong, A. K. Agarwal, D. J. Beebe, and H. Jiang, "Adaptive liquid microlenses activated by stimuli-responsive hydrogels," *Nature*, vol. 442, pp. 551–554, Aug. 2006.

[122] J. Kim, M. J. Serpe, and L. A. Lyon, "Hydrogel microparticles as dynamically tunable microlenses," *Journal of the American Chemical Society*, vol. 126, no. 31, p. 9512–9513, 2004.

[123] D. Schmaljohann, "Thermo-and pH-responsive polymers in drug delivery," *Advanced drug delivery reviews*, vol. 58, no. 15, p. 1655–1670, 2006.

[124] T. R. Hoare and D. S. Kohane, "Hydrogels in drug delivery: Progress and challenges," *Polymer*, vol. 49, no. 8, p. 1993–2007, 2008.

[125] Y. V. Pan, R. A. Wesley, R. Luginbuhl, D. D. Denton, and B. D. Ratner, "Plasma polymerized n-isopropylacrylamide: synthesis and characterization of a smart thermally responsive coating," *Biomacromolecules*, vol. 2, no. 1, p. 32–36, 2001.

[126] J. Lahann and R. Langer, "Smart materials with dynamically controllable surfaces," *MRS Bull*, vol. 30, no. 3, p. 185–188, 2005.

[127] A. Pelah, R. Seemann, and T. M. Jovin, "Reversible cell deformation by a polymeric actuator," *Journal of the American Chemical Society*, vol. 129, pp. 468–469, Jan. 2007.

[128] C.-D. Chen, S.-F. Cheng, L.-K. Chau, and C. C. Wang, "Sensing capability of the localized surface plasmon resonance of gold nanorods," *Biosensors and Bioelectronics*, vol. 22, pp. 926–932, Jan. 2007.

[129] G. J. Nusz, S. M. Marinakos, A. C. Curry, A. Dahlin, F. Höök, A. Wax, and A. Chilkoti, "Label-free plasmonic detection of biomolecular binding by a single gold nanorod," *Analytical chemistry*, vol. 80, no. 4, p. 984–989, 2008.

[130] S. M. Marinakos, S. Chen, and A. Chilkoti, "Plasmonic detection of a model analyte in serum by a gold nanorod sensor," *Analytical chemistry*, vol. 79, no. 14, p. 5278–5283, 2007.

[131] J. Rodriguez-Fernandez, M. Fedoruk, C. Hrelescu, A. A. Lutich, and J. Feldmann, "Triggering the volume phase transition of core–shell au nanorod–microgel nanocomposites with light," *Nanotechnology*, vol. 22, p. 245708, June 2011.

[132] C. F. Bohren and D. R. Huffman, *Absorption and Scattering of Light by Small Particles*. WILEY-VCH Verlag GmbH & Co. KGaA, Dec. 2007.

[133] J. Pérez-Juste, B. Rodríguez-González, P. Mulvaney, and L. M. Liz-Marzán, "Optical control and patterning of gold-Nanorod–Poly(vinyl alcohol) nanocomposite films," *Advanced Functional Materials*, vol. 15, no. 7, p. 1065–1071, 2005.

[134] A. Sanchez-Iglesias, M. Grzelczak, B. Rodriguez-Gonzalez, P. Guardia-Giros, I. Pastoriza-Santos, J. Perez-Juste, M. Prato, and L. M. Liz-Marza?n, "Synthesis of multifunctional composite microgels via in situ ni growth on pNIPAM-coated au nanoparticles," *ACS nano*, vol. 3, no. 10, p. 3184–3190, 2009.

[135] J. Wang, D. Gan, L. A. Lyon, and M. A. El-Sayed, "Temperature-jump investigations of the kinetics of hydrogel nanoparticle volume phase transitions," *Journal of the American Chemical Society*, vol. 123, pp. 11284–11289, Nov. 2001.

[136] W. Ni, H. Ba, A. A. Lutich, F. Jaeckel, and J. Feldmann, "Enhancing single-nanoparticle surface-chemistry by plasmonic overheating in an optical trap," *Nano letters*, vol. 12, no. 9, p. 4647–4650, 2012.

[137] A. G. Skirtach, C. Dejugnat, D. Braun, A. S. Susha, A. L. Rogach, W. J. Parak, H. Möhwald, and G. B. Sukhorukov, "The role of metal nanoparticles in remote release of encapsulated materials," *Nano letters*, vol. 5, no. 7, p. 1371–1377, 2005.

[138] D. Pissuwan, S. M. Valenzuela, and M. B. Cortie, "Therapeutic possibilities of plasmonically heated gold nanoparticles," *TRENDS in Biotechnology*, vol. 24, no. 2, p. 62–67, 2006.

[139] C. M. Pitsillides, E. K. Joe, X. Wei, R. Anderson, and C. P. Lin, "Selective cell targeting with light-absorbing microparticles and nanoparticles," *Biophysical journal*, vol. 84, no. 6, p. 4023–4032, 2003.

[140] G. L. Liu, J. Kim, Y. Lu, and L. P. Lee, "Optofluidic control using photothermal nanoparticles," *Nature Materials*, vol. 5, pp. 27–32, Jan. 2006.

[141] J. S. Donner, G. Baffou, D. McCloskey, and R. Quidant, "Plasmon-assisted optofluidics," *ACS Nano*, vol. 5, pp. 5457–5462, July 2011.

[142] D. Boyer, P. Tamarat, A. Maali, B. Lounis, and M. Orrit, "Photothermal imaging of nanometer-sized metal particles among scatterers," *Science*, vol. 297, no. 5584, p. 1160–1163, 2002.

[143] E. W. Lemmon and R. T. Jacobsen, "Viscosity and thermal conductivity equations for nitrogen, oxygen, argon, and air," *International Journal of Thermophysics*, vol. 25, no. 1, p. 21–69, 2004.

[144] S. Marcus and R. Blaine, "Thermal conductivity of polymers, glasses and ceramics by modulated DSC," *Thermochimica Acta*, vol. 243, pp. 231–239, Sept. 1994.

[145] M. Fedoruk, A. A. Lutich, and J. Feldmann, "Subdiffraction-limited milling by an optically driven single gold nanoparticle," *ACS Nano*, vol. 5, no. 9, pp. 7377–7382, 2011.

[146] A. A. El-Kheshen, M. F. Zawrah, and M. Awaad, "Densification, phase composition, and properties of borosilicate glass composites containing nano-alumina and titania," *Journal of Materials Science: Materials in Electronics*, vol. 20, pp. 637–643, July 2009.

[147] M. T. J. Keene, R. D. M. Gougeon, R. Denoyel, R. K. Harris, J. Rouquerol, and P. L. Llewellyn, "Calcination of the MCM-41 mesophase: mechanism of surfactant thermal degradation and evolution of the porosity," *Journal of Materials Chemistry*, vol. 9, no. 11, pp. 2843–2849, 1999.

[148] S. N. Kasarova, N. G. Sultanova, C. D. Ivanov, and I. D. Nikolov, "Analysis of the dispersion of optical plastic materials," *Optical Materials*, vol. 29, pp. 1481–1490, July 2007.

[149] A. Curry, G. Nusz, A. Chilkoti, and A. Wax, "Substrate effect on refractive index dependence of plasmon resonance for individual silver nanoparticles observed using darkfield microspectroscopy," *Optics Express*, vol. 13, pp. 2668–2677, Apr. 2005.

[150] H. Wang, C. S. Levin, and N. J. Halas, "Nanosphere arrays with controlled sub-10-nm gaps as surface-enhanced raman spectroscopy substrates," *Journal of the American Chemical Society*, vol. 127, pp. 14992–14993, Nov. 2005.

[151] P. Kekicheff and O. Spalla, "Refractive index of thin aqueous films confined between two hydrophobic surfaces," *Langmuir*, vol. 10, pp. 1584–1591, May 1994.

[152] G. Ghosh, *Handbook of Optical Constants of Solids: Handbook of Thermo-Optic Coefficients of Optical Materials with Applications*. Academic Press, June 1998.

[153] A. Plech, V. Kotaidis, S. Grésillon, C. Dahmen, and G. von Plessen, "Laser-induced heating and melting of gold nanoparticles studied by time-resolved x-ray scattering," *Physical Review B*, vol. 70, p. 195423, Nov. 2004.

[154] D. Cristea, P. Obreja, M. Kusko, E. Manea, and R. Rebigan, "Polymer micromachining for micro- and nanophotonics," *Materials Science and Engineering: C*, vol. 26, pp. 1049–1055, July 2006.

[155] J. Behradek, "Temperature coefficients in biology," *Biological Reviews*, vol. 5, no. 1, p. 30–58, 1930.

[156] M. R. Kamal and S. Sourour, "Kinetics and thermal characterization of thermoset cure," *Polymer Engineering & Science*, vol. 13, no. 1, p. 59–64, 1973.

[157] N. Lue, G. Popescu, T. Ikeda, R. R. Dasari, K. Badizadegan, and M. S. Feld, "Live cell refractometry using microfluidic devices," *Optics letters*, vol. 31, no. 18, p. 2759–2761, 2006.

[158] Y.-J. Yang and H.-H. Liao, "Development and characterization of thermopneumatic peristaltic micropumps," *Journal of Micromechanics and Microengineering*, vol. 19, no. 2, p. 025003, 2009.

[159] Y. S. Shin, K. Cho, S. H. Lim, S. Chung, S.-J. Park, C. Chung, D.-C. Han, and J. K. Chang, "PDMS-based micro PCR chip with parylene coating," *Journal of Micromechanics and Microengineering*, vol. 13, no. 5, p. 768, 2003.

[160] R. A. Beth, "Mechanical detection and measurement of the angular momentum of light," *Physical Review*, vol. 50, no. 2, p. 115, 1936.

[161] M. E. J. Friese, J. Enger, H. Rubinsztein-Dunlop, and N. R. Heckenberg, "Optical angular-momentum transfer to trapped absorbing particles," *Physical Review A*, vol. 54, no. 2, p. 1593, 1996.

[162] N. B. Simpson, K. Dholakia, L. Allen, and M. J. Padgett, "Mechanical equivalence of spin and orbital angular momentum of light: an optical spanner," *Optics Letters*, vol. 22, no. 1, p. 52–54, 1997.

[163] T. A. Nieminen, A. B. Stilgoe, N. R. Heckenberg, and H. Rubinsztein-Dunlop, "Angular momentum of a strongly focused gaussian beam," *Journal of Optics A: Pure and Applied Optics*, vol. 10, no. 11, p. 115005, 2008.

[164] J. K. Oh, R. Drumright, D. J. Siegwart, and K. Matyjaszewski, "The development of microgels/nanogels for drug delivery applications," *Progress in Polymer Science*, vol. 33, no. 4, p. 448–477, 2008.

[165] N. Bassik, B. T. Abebe, K. E. Laflin, and D. H. Gracias, "Photolithographically patterned smart hydrogel based bilayer actuators," *Polymer*, vol. 51, no. 26, p. 6093–6098, 2010.

Acknowledgments

At this point I would like to thank those people, whose input made this thesis possible. In particular I want to thank:

Professor Dr. Jochen Feldmann, my supervisor and doctoral advisor, who gave me the opportunity to be part of his excellent group and helped me with important inputs during my time as a doctoral degree candidate. I am grateful for all the support, experience and knowledge which I could obtain during this great time.

Dr. Theobald Lohmüller, for his great contribution as a subgroup leader, for very helpful and long discussions about new ideas and current problems. I would like to thank him for his open minded way of scientific work and his support in all situations.

Dr. Andrey Lutich, who is a former subgroup leader and was always a helping hand in all scientific questions. With his great experience and keen perception he could find a solution to almost every problem.

Dr. Jessica Rodríguez-Fernández, for the successful cooperation in the area of thermoresponsive polymers and interesting discussions about many scientific questions.

Dr. Alexander Urban, for the productive cooperation on the filed of thermally induced shrinking of polymers during his last months in our group before he left to Houston.

I am grateful to the **Nanosystems Initiative Munich (NIM)** for providing the financial support during my doctoral candidate time.

My thanks also goes to the great technical, chemical and administrative support by **Stefan Niedermaier**, **Christian Holopirek**, **Anna Helfrich, Dr. Jessica Rodríguez-Fernández** and **Gerlinde Adam**. I would like to thank our current and former computer administrators **Dr. Alexander Ohlinger, Dr. Raphael**

Tautz, Paul Kühler and **Dr. Felix Deschler** for their great contribution to this difficult and important task.

Also, I thank my colleagues, who helped with proofreading of this thesis: **Anastasia Babynina, Dr. Nicolas Bouchonville, Dr. Michael Carlson, Dr. Sol Carretero Palacios, Dr. Felix Deschler, Silke Kirchner** (best lunchtime comrade), **Dr. Jessica Rodríguez-Fernández, Lidiya Osinkina** and, of course, **Dr. Theobald Lohmüller**.

Many thanks to my former and present room mates: **Dr. Haojin Ba, Dr. Wei Li, Dr. Heihai Ni, Miao Li** and all my dear colleagues: **Verena Baumann, Dr. Maximilian Berr, Jaekwon Do, Ilka Kriegel** (enjoy your time in Milano) and **Spas Nedev** for the great personal and scientific atmosphere.

In particular I would like to thank my family: my parents, **Halyna** and **Yuriy**, my brother, **Dima**, and my girlfriend, **Yevgeniya**, whose enormous contribution helped me through all the good and bad times.